UNIVERSITY OF CALIFORNIA,
IRVINE

Tomographic State Reconstruction and Time Resolved Surface Enhanced Coherent Anti-Stokes Raman Scattering in the Single Molecule Limit

DISSERTATION

submitted in partial satisfaction of the requirements
for the degree of

DOCTOR OF PHILOSOPHY

in Chemistry

by

Steven Yampolsky

Dissertation Committee:
Professor V. Ara Apkarian, Chair
Professor Eric O. Potma
Professor Craig Murray

2014

DEDICATION

To Paulina, for your constant support, unconditional love, and for walking with me into the great unknown...

TABLE OF CONTENTS

LIST OF FIGURES

ACKNOWLEDGMENTS

I would like to express my deepest gratitude and acknowledgment to my advisor, Professor V. Ara Apkarian, for believing in me, for letting me reconstruct experiments countless times over, and always helping guide me on my journey in striving to explain that which we do not yet understand.

I would also like to acknowledge and thank Professor Eric Potma for his enthusiasm, his encouragement, and for many insightful discussions and suggestions.

Thank you to Professor Craig Murray, for being the victim of a last minute committee swap, twice. I am grateful for your help.

Thank you to those of you who have helped shape my understanding and have contributed to this work with many shared discussions and laughs; Dr. Desire Whitmore, Dr. Patrick El-Khoury, Dr. Dmitry Fishman, Kevin Crampton, Dr. Eero Hulkko, Dr. Mayukh Banik, Dr. R. Zadoyan, Dr. Wytze van der Veer, Dr. Dinner, and Dr. Shirshendu Dey.

To all my friends and colleagues without whom the last six years would not have been nearly as survivable; Hayk Zadoyan, Jeremy Garrett, Amir Sadr, Alan Rogers-Kante, Peter Preston, Ash Shamsian, Dr. Alex Ushinsky, Jason Quinn, Dr. Jon Burdett Nicholas Sharac, Alexander Fast, Elizabeth Foreman, Ben Toulson, Ahmet Mentes, and Brian Albee.

Thank you to my "extended" family for offering unconditional support and love at every step of life that has led me to this juncture and beyond; Michael and Anna Moroz, Tanya, Greg and Nicole Zubatov, Michael and Ira Ushinsky.

Finally I would like to thank Mark, Natalie, Alex, David, and Alla Yampolsky, for standing by me no matter what, for your love, care, nurture, for letting me and encouraging me to pursue my dreams.

CURRICULUM VITAE

Steven Yampolsky

EDUCATION

Ph. D. in Chemical and Material Physics **2014**
University of California *Irvine, California*

M.S. in Chemical and Material Physics **2014**
University of California *Irvine, California*

B.S. in Chemistry **2009**
University of California *Irvine, California*

RESEARCH EXPERIENCE

Undergraduate Research Assistant **2007–2009**
University of California, Irvine *Irvine, California*

Graduate Research Assistant **2009–2014**
University of California, Irvine *Irvine, California*

TEACHING EXPERIENCE

Teaching Assistant **2009–2012**
University of California, Irvine *Irvine, California*

REFEREED JOURNAL PUBLICATIONS

Seeing a single molecule vibrate through time-resolved coherent anti-Stokes Raman scattering **2014**
Nature Photonics, vol 8 issue 8 pp. 650

Ultrafast pump-probe force microscopy with nanoscale resolution **2014**
Submitted

ABSTRACT OF THE DISSERTATION

Tomographic State Reconstruction and Time Resolved Surface Enhanced Coherent Anti-Stokes Raman Scattering in the Single Molecule Limit

By

Steven Yampolsky

Doctor of Philosophy in Chemistry

University of California, Irvine, 2014

Professor V. Ara Apkarian, Chair

Time-resolved, surface-enhanced, coherent anti-Stokes Raman spectroscopy (tr-SECARS) is ideally suited for preparing and probing vibrational coherences in molecules. By enhancing the local response of a single molecule with a dipolar nano-antenna, vibrational dynamics have been measured at the single molecule limit. In contrast with tr-CARS measurements in ensembles, the vibrational coherence of a single molecule is not subject to pure dephasing. It exhibits characteristic phase and amplitude noise, which allows the statistical distinction between single, few, and many molecule sources to be determined. To build on the current work, by using three unique pulses to spectrally filter the response of the molecule, the characteristic noise can be isolated and measured background-free. If the probing of a superposition state is carried out over a real resonance, then it is possible to tomographically reconstruct the complete description of quantum dynamics in phase space representation via the Wigner Distribution Function(WDF). The WDF can be reconstructed from either the wavepacket via Wigner Transform, or an experimentally measured density, via an Inverse Radon Transform. The calculations presented here highlight the necessary conditions in order to reconstruct the WDF with fidelity from a proposed experiment and compare the density derived WDF with that of the wavepacket. The principle is firstly demonstrated using a Kerr gated detection of emission from an evolving state on a bound harmonic potential

energy surface. The model is then explained in the case of a proposed spectrally resolved transient grating experiment (SRTG). The WDFs generated from the limiting conditions show that the reproduction fidelity of the experimentally derived WDF are dependent on the probe, utilized to measure the evolving superposition, and the curvature, or the vibrational frequency of the potential energy surfaces, and the dephasing time of the vibrational superposition states. Given two potentials, I show that it is possible to optimize probe pulse parameters to improve the fidelity of the state reconstruction. Due to the variational principle, the negative volume of the WDF, or the Wigner hole, can only be reduced via measurements - the pulse parameters can be optimized iteratively even when the molecular potentials are not known.

Chapter 1

Introduction

The last half century has seen the development of tools that allow for the study of single molecule dynamics[1]. Understanding the characteristic behavior of a single molecule will revolutionize applications, research and education[2, 3]. The Chemistry at the Space-Time Limit (CaSTL) center at the University of California in Irvine is funded by the National Science Foundation to conquer the challenges of understanding the physics that govern life at the space time limit. I have been fortunate enough to take part in this research effort alongside the brightest minds in this discipline. Together with their invaluable contributions and guidance we have helped advance a rudimentary understanding of life at the single molecule limit. I have attempted in this dissertation to put the ongoing efforts in a historical context, describe the necessary theory and experimental apparatuses required to chase these goals, and laid forth a theoretical model for a further grand experimental challenge.

Chapter 2 outlines a story about single molecule detection and spectroscopy as measurements that have evolved from linear spectroscopic techniques[4–8] to time resolved nonlinear methods[9–12] that can be used to not only detect, but also to control the quantum state of a single molecule and enhance its vibrational response. The single molecule signal is minis-

cule and requires surface enhancement to amplify its response[13, 14]. Along with a brief overview of surface enhancement[15], I have laid out the necessary computational steps to model molecular dynamics in the bulk by using time resolved coherent anti-Stokes Raman scattering[16, 17]. This method, along with surface enhancement, is implemented to measure vibrational superpositions in a single molecule and extends our current knowledge of nonlinear single molecule spectroscopy.

Chapter 3 provides a brief overview of the design and construction of a flexible experimental apparatus capable for interrogation of molecular systems using nonlinear spectroscopy. The design of a unique synchronously pumped three color system capable of executing virtually any four wave mixing measurement is described, with most of the necessary details required to construct and align such a system. The characterized tunability and temporal profiles of the system are enclosed. However, this system is ideal for measuring large quantities of molecules, and thus requires a lower peak power, higher repetition rate alternative to optimize measurements on single molecules.

Chapter 4 documents the first demonstration of time resolved surface enhanced coherent anti-Stokes Raman scattering (tr-SECARS) measurements executed on a single molecule[18]. This experiment elucidated the fate of a single molecule vibrational coherence on the ground electronic state, in the absence of pure dephasing. The details concerning the execution of such a measurement are presented with the analysis to extend the numerical model in Chapter 2 to include single and few molecule samples as well as the caveats encountered when measuring the nonlinear response of a single/few molecule system. An experimental system engineered to further investigate the single molecule behavior is described showing early results reproducing the previously published work.

Chapter 5 proposes the holy grail experiment on a single molecule. The developed numerical model describes the experiment conceived to measure the time dependent wavefunction of a single molecule. The generalized details required for the complete determination of the

Wigner distribution function[19] for a single molecule are then demonstrated, documenting the fidelity with which such a measurement can be made.

An included appendix contains the raw code for the numerical modeling of the figures and the experiment proposed in chapter 5, (relatively well)optimized for use in Mathematica.

Chapter 2

Single Molecule Spectroscopy

2.1 Linear Spectroscopy of a Single Molecule

The first observations of a single molecule were made by absorption of incident light conducted under cryogenic conditions. Single pentacene molecules in a p-terphenyl host crystal[20] were used to measure changes in incident light intensity[4]. By detuning the laser frequency to 6-8 standard deviations away from the center of the inhomogeneous absorption line[21], where the average number of absorbers is 10^8 in comparison to 10^{15} at the center of the absorption line, absorption of zero phonon lines, 0_1 (592.32 nm) and 0_2 (592.18 nm) of pentacene were measured at 1.6 K. Absorption studies of one molecule, as opposed to the ensemble, allowed for studies concerning local environments surrounding the molecule itself giving vast insight into chemistry at the microscopic limit.

Single molecule fluorescence[5], using the same molecule in the same host crystal, also under cryogenic conditions, was observed shortly following absorption. Orrit and Bernard monitored the emitted fluorescence intensity of the system as a function of laser excitation frequency and observed fluctuating fluorescence intensities. The observation of a fluorescence

peak disappearing and reappearing was determined to be a hallmark of single molecule hole burning. In order to efficiently study hole burning in single molecule samples[22], three conditions must be fulfilled; 1. The absorption cross section must be large and the homogeneous line width of the absorption must be small, 2. the molecule must emit a sufficient amount of photons before the resonance frequency is allowed to irreversibly shift, and 3. the rate at which photons are emitted must be higher than the dark counts of the detector. The 0_1 and 0_2 lines of the single pentacene molecules embedded in a p-terphenyl host crystal proved to be an ideal candidate that satisfied all three of these conditions allowing for the first signatures of fluorescence in SMS.

Detection of single molecules isolated in their local ambient environments allowed for the possibility of studying physical and biological processes in their natural surroundings. However, at room temperature, the single molecular cross section is reduced by five to six orders of magnitude[23] relative to when it is cryogenically cooled. This was overcome by increasing the single molecule's cross section via a subwavelength light aperture in a near-field optical microscope[6]. Plakhotnik et al. [24, 25] proposed another method to detect the absorption of single molecules by using far field microscopy. In this far field regime, the elastic scattering of the single molecule would coherently interfere with the incident laser field.

An indirect way of measuring the absorption of a single molecule in ambient conditions is via heat dissipation. A thermal lens effect was used to measure slight temperature increases around the absorbing object[26]. In this study, though an integration time of one second was much longer than the diffusion time of a single dye molecule traversing the focal region, it is speculated that thousands of individual molecules would be necessary to generate the signal. A simple calculation shows that a single molecule should be undetectable via absorption against the photon noise in a one second acquisition[23].

Fluorescence observation of single molecules in ambient conditions soon followed. Trautman and colleagues[27, 28] were able to correlate single molecule emission spectra with fluores-

cence lifetimes of dye molecules in PMMA. Xie et al. observed spontaneous and photoinduced spectral fluctuations of sulphorhodamine 101 in PMMA, elucidating information about the energy dissipation from the molecule to the polymer bath. These fluorescence measurements involved isolation of the molecule in a host matrix which restricted studies of single systems in their native surroundings. Although proving that fluorescence detection of single molecule is indeed possible, a more novel system was on the horizon.

Ambient fluorescence detection schemes of bulk Rhodamine in a hydrodynamic flow cell[29, 30] and in microdroplets[31] paved the way for the first demonstration of single molecule detection in an aqueous medium by Nie et al[7]. By using a diffraction limited spot size of $260\mu m$, the free diffusion of single Rhodamine 6G chromophores was observed. Moreover, the fluorescence fluctuations due to diffusion in single molecule detection allowed tracking the orientation and location of the single molecule reporter. This was first demonstrated with a two dimensional localization accuracy of 30 nm for single molecule dyes in phospholipid membranes[32] and green fluorescent protein[33]. The localization prospect of single molecules revolutionized measurements concerning biological processes by allowing real-time imaging of single viruses infecting living cells[34]. The above was made possible by fluorescence correlation spectroscopy, where diffusion analysis can be made by correlating the intensity of the fluorescence relative to the stationary excitation volume[35].

In addition to elucidating the location of single molecules, the transition dipoles for single molecules were experimentally determined by using polarization-modulated linear excitation. This was first demonstrated at low temperature[36] and in ambient conditions using near field optical microscopy[6, 37, 38].

Single Molecule detection was also demonstrated through resonant Raman[39] and nonlinear absorption[40]. In the latter case diphenyl -octatetraene molecules[41] were cooled in a cryostat to 1.6 K. At ambient temperatures, the one photon transition from the ground 1^1A_g to the excited 2^1A_g state is forbidden, but at low temperatures there exists a weak coupling

between the 2^1A_g state with another 1^1B_u state, to which a one photon transition is symmetry allowed[42]. By Pumping the 444 nm resonance with a continuous wave laser centered at 888 nm, two photon induced fluorescence was observed at 500 nm. When pumping at the peak of the resonance, the statistical fine structure of the molecule is reproduced[20]. When scanning the wing of the resonance, three spectrally separated fluorescence events were detected and identified as single molecule signatures by their characteristically sudden spectral jumps[43].

The advent of single molecule detection was marked by characteristic behavior in photon arrival times, spectral diffusion and inhomogeneous broadening. The following covers a small portion of feasible physical rationalizations for the emergence of these features in single molecule spectroscopy, which go undetected and are averaged over in ensemble measurements.

2.2 Characteristic Observables in Single Molecule Spectroscopy

In the realm of linear absorption we consider the behavior that is hallmark of single molecule is uniquely distinguishable from its ensemble counterparts. The differences manifest themselves in characteristic distributions of absorption lineshapes, photon counts, photon bunching and anti-bunching, and blinking or intensity fluctuations.

2.2.1 "Time Dependent" Single Molecule Spectroscopy

The arrival times of the fluorescence photons from a single molecule present invaluable information. In the case of the ensemble, synchronization of a short laser pulse is required to denote events regarding the arrival time of signal photons. But in the case of a single

molecule, the emission of a photon may signal the start of emission for a nearby neighbor. Therefore, time dependent emission of a single molecule remains informative even under continuous excitation. This principle was demonstrated by studying an inter-system crossing to a non-radiating triplet state[44]. The fluorescence of a single molecule was characterized by on and off times in the stream of measured photons leading the researchers to conclude that coupling non-radiating triplet state was responsible.

Studying the distributions between consecutive photons, on and off times, and distributions of signal intensities at discrete points in time can reveal various characteristics about the system. The distribution of consecutive photons can show anti-bunching; a single molecule cannot emit two photons simultaneously, giving instant verification of a single molecule in the interaction volume[45]. Spontaneous emission will exhibit an Poisson decay of photons with respect to arrival times[46, 47], whereas synchronized emission, by action of a short laser pulse will exhibit a Poisson distribution centered around the time between laser pulses[48]. Bath effects can also be extrapolated if a Poisson distribution arising from synchronized emission exhibits asymmetry.

2.2.2 Intensity Fluctuations

A Mechanism that can explain the intensity fluctuations and blinking observed in SMS measurements include triplet-state dynamics, where the fluorescence of a molecule is not observed because of coupling to a triplet state[49, 50]. In absence of a triplet state, the fluorescence blinking could be attributed to charging effects[51, 52].

2.2.3 Spectral Diffusion and Absorption Lineshapes

Spectral Diffusion was originally investigated in large ensembles by linear[53] and nonlinear[54, 55] spectroscopy, however the first realization of single molecule spectral diffusion was made by Moerner in measurements at 1.6K. Barkai et al.[1] goes on to methodically structure a greater understanding of these phenomena.

In an ensemble measurement, characteristic spectral fluctuations of single reporters, arising from host defects and spectral diffusion due to environmental changes, are averaged over[56, 57]. If it is assumed that these interactions are pair-wise additive and only depend on the distance between individual reporters, the excited state Hamiltonian for each individual reporter is randomized as the aforementioned distance evolves non-trivially in the excited state. The resulting absorption frequency of each reporter also evolves in time leading to spectral diffusion that can be observed when interrogating a single molecule. Rotational dynamics[58] and conformational changes in macromolecules[59, 60] also lead to spectral diffusion.

The Kubo-Anderson theory approximates spectral diffusion with a time-dependent[61, 62] stochastic process. Here, the absorption line and its width are given by the Fourier transform of the dipole correlation function, and include the average time dependent stochastic frequency fluctuations for the ensemble measurement. If the host is subject to defects unique to each reporter site, the information of the surrounding nanoenvironment is also averaged over, giving rise to inhomogeneous broadening[63]. Measurements on a single molecule allow for direct measurement of this time dependent spectral diffusion, and interrogation of the line shape distortions due to disordered host media.

2.2.4 Limitations to Incoherent Spectroscopy

Though insightful for interrogation of(but not limited to) behaviors as described here, incoherent spectroscopy can only address single molecule dynamics that occur on a time scale much longer than the measurement time. Such techniques are well suited to study enzymatic dynamics[64] and protein folding[65]. But to understand the nature of the molecular bond or the fate of a quantum coherence across multiple electronics surfaces, the tools required have to perturb on the timescale of such processes and require picosecond to femtosecond resolution in time.

2.3 Electronic Coherences in Single Molecule Spectroscopy

Quantum Coherences are hidden at the core of most important processes in nature amounting to a key cog in the wheel of the ecosystem that allows life to exist. The electronic coherence time of photosynthetic systems allows for naturally efficient conversion of sunlight into energy[66–68]. It is thought that interaction of a particular system with the bath introduces loss of coherent information, however some of the protein structure may be in fact preserving the coherence of photosynthetic processes[69, 70]. Understanding and controlling a coherent superposition will allow not only more efficient light-harvesting devices but also applications in the quantum processing realm, which would increase our computing speeds significantly in relation to the most powerful classical computers[2, 3]. Measurements of a molecular electronic coherence initially demonstrated with ultrafast pulses on an ensemble[71] have been extended to the single molecule limit[9]

Recently, van Hulst and coworkers published a series of experiments demonstrating coherent control of single molecule dyes. By using a pair of phase locked pulses and varying the time and phase delay between the pulse pairs, coherent control of bond dissociation and

rearrangement [72], laser induced fluorescence[73], coherent anti-Stokes Raman [74] and high harmonic generation[75] has been demonstrated. In these cases, the delay and phase between the pulse pairs is optimized to maximize the efficiency of the desired photo-effect. While photobleaching can quickly occur during the process of phase/delay optimization on a single molecule, faster, more intuitive approaches, with comparable efficiencies have been shown[76]. By monitoring the single molecule fluorescence intensity while the excitation intensity is kept constant, a direct measure of excitation probability can be observed as function of phase and time delay[11] between the pulse pairs.

In their first observation, van Hulst and coworkers, saw that for a pair of phase locked pulses where the phase between the two was zero, there was a modulation in fluorescence intensity as a function of time delay between the pulse pair. The attributed effect was explained by wavepacket inteferometry[77]. In this phenomenon, if the molecule is initially in the ground electronic state with the pulse pairs each being resonant with a singlet-singlet, ground to excited state transition, the first pulse will transfer probability amplitude to the excited state, exciting(if broad enough) several vibrational states that oscillate on the potential energy surface. The second pulse generates the same wavepacket but at a later point in time. If the quantum interference between the first and second wavepacket at some time delay is constructive, the excitation probability is enhanced and the fluorescence emission is greater. However if the quantum interference is destructive, then the excitation probability is suppressed, and the fluorescence intensity is lowered. In total the group measured 52 molecules, which exhibited a distribution in phase as a function of time delay, and the frequency of the oscillations, attributed to different local environments in the form of various dispersive interactions and structural hindrances embedded in the host matrix[78]. Further manipulation of the wavepacket interferometry was demonstrated by showing inversion of the time dependent molecular oscillations by manipulating the relative phase between the pulse pair from 0 to π [10]. While the coherent control of a single molecule at room temperature is demonstrated, the optimized phase and time delay for each system vary. This is exactly as

expected for an inhomogeneous distribution of single reporters in varying local environments. The solution to the inhomogeneity is found in the unique optimization of the phase and time delay between the pulse pairs to optimize coherent control of these single molecule systems.

The coherent superposition state created by the first pulse will often decay due to scattering of host vibrations, a process also known as pure electronic dephasing[79] which happens over the course of less than 100 fs. Phase locked pulse pairs, in sequence and at short time delays allow probing of such a short lived coherence. If the pulses are not phase locked, the electronic coherence cannot be probed due to the phase averaging. The constructive and destructive quantum interference as a function of time delay results from varying interaction strengths between the molecular transition dipole moments and the laser fields that differ from molecule to molecule, or Rabi frequencies[11] and is nascence of quantum manipulation[9]. If the Rabi frequency is small, only absorption to the excited state takes place, and the transfer of population to the excited state becomes less efficient as the time delay between the pulses is increased. If the frequency is large, population inversion and subsequent stimulated emission is also possible. At larger delay times, the pure dephasing is responsible for lower efficiency of the stimulated emission process by the second pulse. Using the optical Bloch equations[80], retrieval of the transition dipole moment is possible if the pertinent parameters of the electric field are known and is covered in greater detail elsewhere[12]. This was the first demonstration of Rabi oscillations on single systems which has thus far been observed only on organic dyes in a host matrix[81, 82] and quantum dots at low temperatures[83, 84].

A more detailed examination of the collected data and the technique which allows probing of the phase memory of the coherent superposition created by a pulse displays that photophysical parameters such as the transition dipole moments, pure electronic dephasing times, incoherent vibrational relaxation times, and vibrational energies can be extracted from phase lock pump probe measurements at room temperature[12]. van Hulst and coworkers measured

a distribution of Transition dipole moments, dephasing times, and Rabi frequencies across 52 molecules, with a forseen possibility of retrieving the full three dimensional orientation of the transition dipole moments[85].

These electronic coherence measurements were limited by the electronic dephasing time which occurs on a timescale much faster than the periods of vibrational motion, as predicted by the implicit broad and featureless absorption spectra, characteristic of chromophores. In this regard, Raman spectroscopy is better suited to study single molecule coherences because it does not require evolution on real electronic states. Moreover, time-resolved coherent anti-Stokes Raman scattering(tr-CARS) can be used to monitor the real-time evolution of a vibrational quantum superposition by measuring their relative phase as a function of time between the preparation of the superposition and subsequent probing.

2.4 Vibrational Spectroscopy of Single Molecules

While using phase-locked pulse pair excitation on an electronic surface allows the measurement of coherent evolution, Raman spectroscopy has the potential to measure similar characteristics of single molecules without the loss of coherence due to electronic dephasing. This is possible via time resolved coherent Stokes and anti-Stokes Raman Spectroscopy. While the electronic dephasing problem can be overcome using Raman scattering, the relatively feeble quantum yield of Raman photons (1 for every 10^7 incident photons) presents another problem, which makes single molecule sensitivity a greater challenge. Using plasmonic antennas[86] the Raman scattering can be greatly enhanced via the surface enhanced Raman scattering (SERS) effect[87, 88].

The SERS effect was first observed by Hendra and coworkers[89–91] using pyridine adsorbed on silver and copper electrodes. The group attributed the high intensity Raman peaks to a

purported large number of molecules at the electrode surface. Jeanmarie et al [87] extended the initial observations and observed that the collected vibrational spectra exhibited high resolution and high sensitivity to the local surface environment of the electrodes, as well as the orientation of the molecule with respect to the electrode surface. Jeanmarie et al further investigated the observations of this effect to other nitrogen heterocycles and amines for the purpose of studying kinetic processes that occurred at electrode surfaces. Creighton and Albrecht[92] along with van Duyne and coworkers concluded that there was a degree of surface enhancement in the measured range of 10^5-10^6[93] and initiated a series of experiments that aimed to explain the enhancement and its manifestation in other photophysical processes and environments such as thin films[94, 95], Colloidal nanoparticles[96, 97], and nanowires[98].

Plasmonic enhancement, the underlying cause of surface enhanced signals first observed by Fleischmann et al [89], allows coupling and manipulation of light radiation at subwavelength scales[99]. This mechanism enhances the efficiency of light emission[100, 101] of the molecule used for use in various applications, including spectroscopy[102]. Radio wave frequency and microwave technology has long ago matured to allow subwavelength scale manipulation of radiation, however this same technology has yet to be made more robust in the realm of optical frequencies. This is largely due to the size requirements for optical antennas, which allow control of structural features down to the nanometer scale. This realm of control is becoming more available with time with electron beam lithography[103], and ion-beam milling[104]. In time, optical antennas will add to the plethora of optical control devices including that of mirrors, lenses fibers and diffractive elements and further expand the capacity to which optical fields can be manipulated. The goal is to design structures to enhance the energy transfer of freely propagating optical radiation into localized energy and to generate the same effect in reverse[105]. The "optical transducer" would allow for coupling of optical fields to objects much smaller than the wavelength of the field efficiently.

The enhancement of the Raman photons from the single molecule is made possible by simultaneously excited surface plasmon modes of a nearby metal. van Duyne and coworkers found that this effect is most efficient if the metallic structure is Ag, Cu, or Au. In the presence of an electric field, a metal nanosphere's surface electron density will oscillate at the frequency of the incident electric field[106, 107]. When there are two spheres in close proximity, and the incident electric field has the optimized polarization, a dipole can be created at the nanometer size junction between the two metal spheres. This dipole is confined and effectively focuses the incident optical field similarly to the optical antenna scheme discussed previously. The electron density of the metals oscillates at the frequency of the incident optical field. This allows efficient coupling of incident fields to subwavelength scales. The junction between the spheres is roughly a few molecules in size, constituting the ideal environment, and the necessary enhancement to allow Raman Spectroscopy of a single molecule.

2.5 Single Molecule SERS

Following the initial demonstrations of plasmonic enhancement in the realm of single molecule detection via SERS[108, 109] at room temperatures, the field of Single Molecule SERS (SM-SERS) developed rapidly[110]. Kniepp et al and Nie et al, experimentally observed a Raman cross section at $10^{-}16\ cm^2$, a cross section magnitude comparable to that of a fluorescent dye. Hildebrandt and Stockburger[111] obtained similar results that indicated the enhanced Raman scattering efficiencies can approach those of the Rhodamine 6G fluorescence intensities used in the aforementioned experiments scaled from a non single molecule, though very dilute response. The development of SM-SERS detection allowed for imaging at sub-molecular resolution at the plasmonic junction of a scanning tunneling microscope tip[112]. However the optimum mechanism of enhancement remained a mystery.

Ensemble averaged SERS studies on lithographically prepared periodic substrates have been

conducted in an attempt to elucidate the optimum enhancement conditions. It was found that the SERS enhancement varied with the aspect ratio of the metal particles[113]. This aspect ratio determined the frequency of the localized surface plasmon resonances[114]. This relationship was experimentally confirmed and it was found that the peak SERS enhancement is obtained when the incident laser field is higher in energy than the plasmon resonance by a factor of 1/2 of the vibrational state that was to be enhanced[115]. Working in this regime purportedly enhances both the incoming field and the outgoing Raman photons in a method most optimized for the SERS signal. For SM-SERS the local surface plasmon resonance(LSPR) was found to have little effect on the overall SERS intensity[116]. Correlated AFM-LSPR-SMSERS studies later confirmed that the SERS signal originated from a junction that would form between at least two metal particles[117] referred to as the "hot-spot". Other studies that attempted to correlate the SERS enhancement factor with a LSPR in the presence of dipolar "hot-spots" showed that the relationship is "tenuous at best"[118], and showed something of a linear relationship[119] between the incident field strength and the measured signal. The systems with hot spots showed stronger SERS enhancement at incident field frequencies far from the LSPR. It was argued that the reduced far field scattering at frequencies near the LSPR was damped due to the interference of the resonant modes of individual metal nanoparticles[120, 121]. Van Duyne and coworkers[122] revealed experimentally that for a series of geometries ideal for SM-SERS, involving a dimer and trimer(two and three metal spheres in close proximity) geometries, and for variable excitation along the visible light spectrum, the relationship between LSPR and the SERS enhancement factor is not direct.

Theoretical calculations have shown that the "hot-spot" exhibits exceptionally high local fields in the interstitial region between two metallic nanospheres[123, 124] and also between a nanosphere and a substrate[125]. SERS Enhancement factors of 10^5 have been predicted[126], with surface enhanced resonant Raman scattering (SERRS) as high as 10^14 having been demonstrated[127]. Given that the hot-spots are ideal in size to capture one to few molecule

reporters, pursuit and understanding of these systems and their applications in SERS has led to synthesis of systems that are engineered to take advantage of these hot spots[106]. Moreover the reproducibility if the high field enhancement factors has made the engineered system a most attractive candidate for SM-SERS[128].

Correlated atomic force microscopy (AFM-SERS) measurements[14] on such an engineered system, revealed strong intensity and spectral fluctuations between adjacent peaks of di-benzene-dithiol located at the junction of two silver nanospheres where the enhanced local field is largest[129, 130]. Such behavior, considered to be the hallmark behavior of single to few molecules signals, can often lead to irreversible damage at high incident energies, and even fusion of the two nanospheres. At the threshold of 1 V/nm, charge tunneling may take place across the junction of the spheres [131]. While the push for true single molecule sensitivity shows promise, the stability of the system remains a question.

To further understand, and perhaps isolate the single molecule, the system must be made more structurally robust and able with withstand incident energy to generate a measure-able response. SM-SERS measurements have shown that it is indeed possible to measure a Raman spectrum from few reporter molecules as indicated by the spectral and intensity fluctuations as a function of observation time. Moreover, insight into the spectral and intensity fluctuations can reveal more information as to the activity of the nanogap and deeper insight into the SERS effect without the interference of ensemble averaging. The spectral and intensity fluctuations can be caught if the fluctuations are slower than the measurement time, however acquisition of a Raman spectrum often requires a frame period in the range of 100 milliseconds. If the integration time is too slow, the fluctuations are averaged over and the result is an inhomogeneous lineshape. The timescale of these fluctuations remains to be documented. Time-resolved coherent anti-Stokes Raman scattering(tr-CARS) allows capturing the vibrational motion of molecules on the timescale of femtoseconds[132, 133]. In using tr-CARS, it is possible to clock the spectral diffusion of the vibrational peaks in

real-time. However it is not clear if the principles of SERS can be directly transfered to the ultrafast time domain, where the high peak powers of ultrashort laser pulses have more drastic effects on plasmonically enhanced nanoparticle systems.

2.6 Surface Enhanced Coherent Anti Stokes Raman Scattering (SE-CARS)

Metallic nanoparticles, used in generating SERS active nanojunctions, may migrate due to the optical forces of ultrashort laser irradiation where the irradiance can reach upwards of 10^{10} $\frac{W}{cm^2}$. Experiments show that the structures can melt, change shape or even fragment[134]. Understanding the effects of ultrafast irradiation on these particles is vital in order to successfully carry out nonlinear spectroscopic measurements that can characterize surface enhancement effects on an ultrafast timescale.

The interaction of laser light with silver[135, 136] and gold[137, 138] nanoparticles has been studied extensively. Both have strong bands in the visible region due to the surface plasmon resonance[139]. The electron phonon relaxation time was measured to be a few picoseconds in length in the low excitation limit where the temperature of the nanoparticle is raised by only a few tenths of degrees. In the higher power excitation limit the metal nanoparticles lattice temperature goes to values well above the melting point within a few picoseconds, while the temperature of the surrounding environments remains essentially constant. In this regime, the particles can change size[140] and shape[141] before the energy is dissipated to the surrounding environment by phonon-phonon coupling, which occurs over the timescale of 100 ps[142]. In the case of sphere shaped particles, which are most ideal for creating SERS -active nanojunctions, the melting may remain unnoticed due to the thermodynamically favoured shape's lower surface energy. Under the influence of nanosecond pulse excitation

nanoparticles have been observed to fragment into smaller spherical particles[141]. These results were confirmed by monitoring the optical absorption spectra and post-mortem TEM analysis of the particles.

Though dynamic metamorphosis of the nanoparticles has been observed, surface enhanced coherent anti-Stokes Raman scattering (SE-CARS) measurements have been executed on SERS-active ensembles[143, 144].

Surface enhanced coherent anti-Stokes Raman scattering was first measured on a plane metal silver surface by Shen *et al* in 1984.[145] Upon examining a plane silver surface with the CARS method, a 992 cm^{-1} vibration was observed from a benzene molecule. Shortly thereafter Chew and coworkers [146] predicted an enhancement factor of SECARS of 10^{12} when the pump and stokes beams were both perpendicularly oriented to the metal plane, but a 10^{21} enhancement factor when the fields were cross polarized. This magnitude of enhancement factors have not yet been realized experimentally. Very recently, an experimental SECARS enhancement factor of $3.6x10^7$ has been observed from a self-assembled monolayer of benzenethiol on a silver coated substrate.[13]

Chew et al [147] theoretically predicted the presence of surface enhanced coherent anti-Stokes Raman scattering from molecules within the vicinity of colloidal spheres similar to the ones used for creating SERS active molecules described above. The prediction, based on electromagnetic enhancement gives a maximum enhancement factor of 10^{10}. The enhancement was predicted to be most dependent on the polarization of excitation and was found to fall off rapidly as the distance between the nanoparticles and the molecule is increased. Namboodiri and coworkers were able to show surface enhanced CARS however only saw an enhancement factor of 10. This lower than expected result was attributed to diffuse scattering of the laser and signal photons by the increasing silver colloid concentration, as well as only a few of the particles being in the optimum geometric arrangement to satisfy phase matching conditions for generation of the anti-Stokes photons.

Although one example of a time resolved surface enhanced Raman scattering measurement has been reported in a colloidal ensemble[148], only one instance of such a measurement has been achieved at the single molecule limit[18]. This fundamental breakthrough lays the groundwork for time domain spectroscopy at the single molecule limit and its potential to elucidate the nature of surface enhancement. The following covers the theory of tr-CARS and the challenges in performing such a measurement on a single molecule

2.7 Time-Resolved Coherent Anti-Stokes Raman Scattering (tr-CARS)

Time-resolved coherent anti-Stokes Raman scattering (tr-CARS) is a powerful tool in the arsenal of nonlinear optical spectroscopy techniques used for preparing and later interrogating vibrational dynamics on the ground electronic state of a molecule.[149, 150] tr-CARS a measurement as a function of time, is in many ways the Fourier analogue of the Raman Measurement. Raman Spectroscopy allows the measurement of vibrational frequencies in the frequency domain, while tr-CARS allows simultaeneous preparation of multiple vibrations and measures the relative phase evolution of the prepared vibrations in real time.

tr-CARS measurements are well documented for ensembles of molecules.[151–153] In the ensemble measurement, the observed signal strength is proportional to the square of irradiated molecules but is limited in information by the ensemble coherence time.[154] A measurement on a single molecule is not limited by this loss of coherent information, known as pure dephasing. This raises fundamental questions regarding the fate of the induced coherence and poses an interesting challenge. The coupling of the incident optical fields and resolution of the feeble single molecule response can be enhanced by the use of a plasmonic antennae. But first, the principles behind tr-CARS will be illustrated and the transformation of information

from a Raman Spectrum [15, 155]

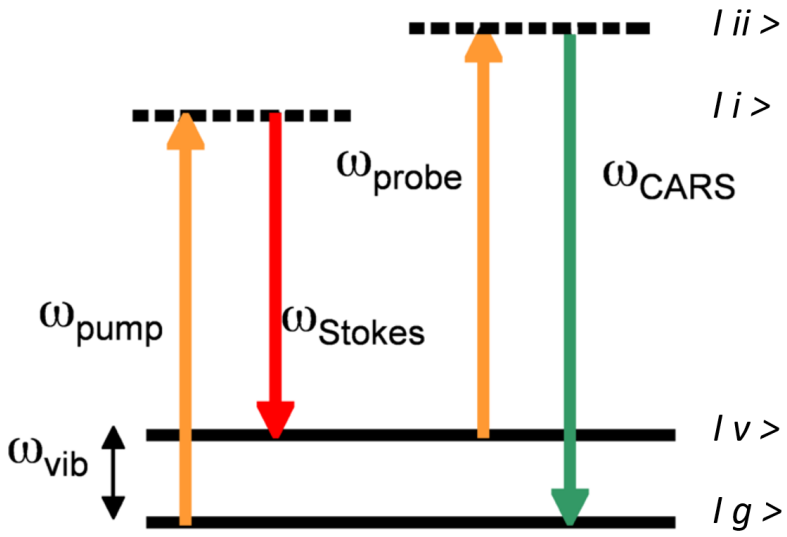

Figure 2.1: Jablonski representation of tr-CARS. The pump beam ω_p promotes electrons from the ground state $|g\rangle$ to an imaginary excited state $|i\rangle$, the Stokes beam ω_S then stimulates the electrons to vibrational eigenstates $|v\rangle = \omega_P - \omega_S$ where after Δt of evolution, the electrons are excited to another imaginary state $|ii\rangle$ (referred to in text by $|i'\rangle$) by the probe pulse ω_{pr}. From the final state $|ii\rangle$ the electrons spontaneously relax to $|g\rangle$ accompanied by the emission of an anti-Stokes photon $\omega_{AS} = \omega_p - \omega_S + \omega_{pr}$

Time-resolved coherent anti-Stokes Raman scattering(tr-CARS)[156] is illustrated in Jablonski representation in Figure 1.1. The preparation consists of action by a pump (ω_p) and a Stokes (ω_S) pulse, at time $t = \tau$ described classically;

$$E_p(t,\tau) = E_{0,p} e^{-(\frac{t-\tau}{\sqrt{2}\Delta t})^2} e^{-i\omega_p t} \tag{2.1}$$

with the Stokes pulse;

$$E_s^*(t,\tau) = E_{0,s} e^{-(\frac{t-\tau}{\sqrt{2}\Delta t})^2} e^{i\omega_s t} \tag{2.2}$$

where E_0 describes the amplitude of the field, ω, the carrier frequency (such that $\omega_p > \omega_s$),

τ, the time at which the pulse acts, and Δt the variance of the pulse envelope, where the FWHM of the pulse is $2\sqrt{2\ln 2}\Delta t$, assuming a Gaussian envelope. A graph of a pulse in time, including its real, imaginary and envelope components is shown in Figure 1.2. The

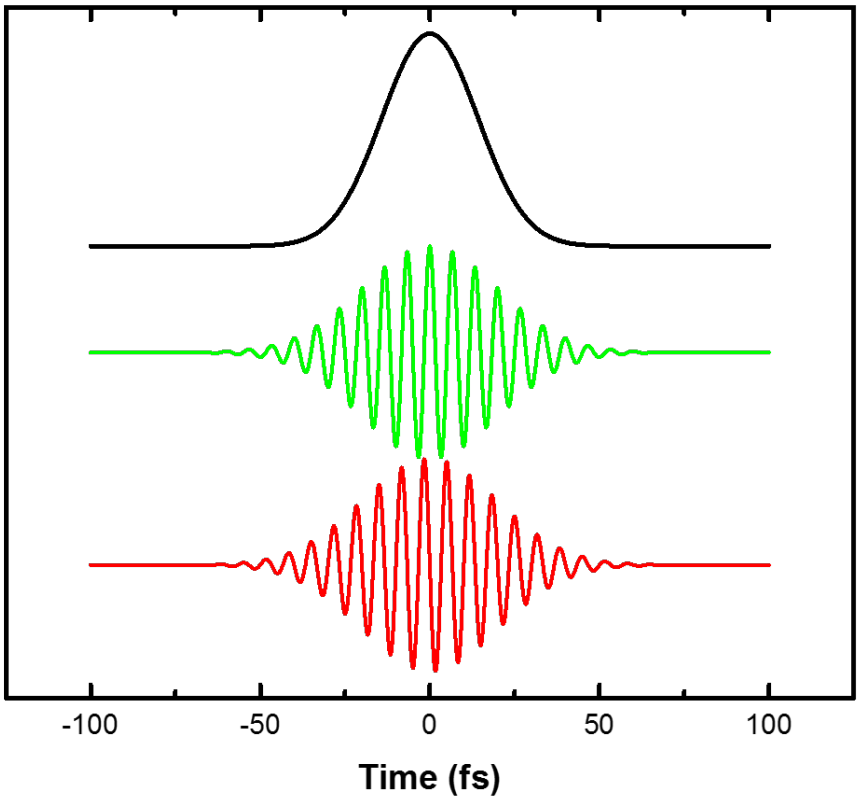

Figure 2.2: A Gaussian pulse with $\omega = 374$ THz (800 nm) and $\Delta t = 20$ fs with the imaginary (red), real (green), and intensity (black) components offset vertically

higher energy pump pulse promotes the ground state, $|\psi^{(0)}(x,0)\rangle$ of the system to an excited $|\psi^{(1)}(x,t')\rangle$ [16], where;

$$|\psi^{(1)}(x,t')\rangle = -i\int_{-\infty}^{\tau_1} e^{-iH_{mol}(t)}\mu_{gi}(x)E_p(t,\tau_1)|\psi^{(0)}(x,0)\rangle dt \tag{2.3}$$

where H_{mol} is the Hamiltonian of the system and μ_{jk} is the transition dipole moment between

j and k states. The longer wavelength Stokes pulse stimulates the amplitude down to create a vibrational superposition $|\psi^{(2)}(x,t)\rangle$ in the ground electronic state;

$$|\psi^{(2)}(x,t'')\rangle = -i\int_{-\infty}^{\tau_2} e^{-iH_{mol}(t')}\mu_{iv}(x)E_S^*(t',\tau_2)|\psi^{(1)}(x,t')\rangle dt' \tag{2.4}$$

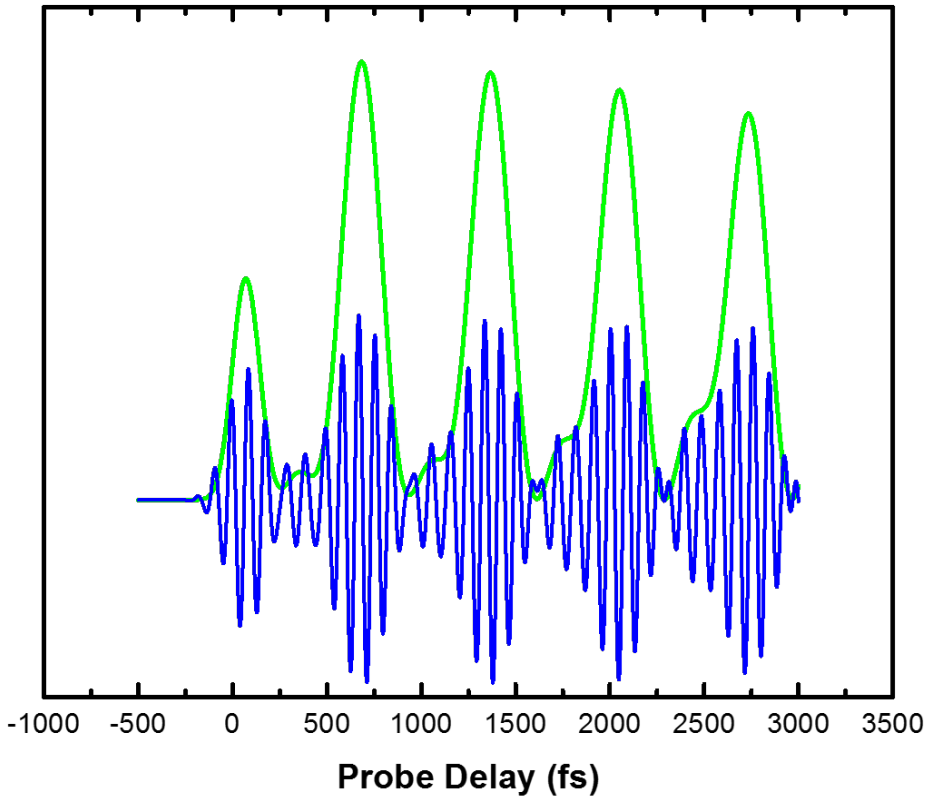

Figure 2.3: A vibrational wavepacket ψ consisting of four eigenstates prepared at $t = 0$ fs (blue) along with the density $|\psi^*\psi|$ of the wavepacket (green), where the oscillations, in green, are comprised of difference frequencies between the prepared vibrational eigenstates

A vibrational coherence $|\psi^2(x,t)\rangle\langle\psi^0(x,t)|$ is created. The evolution of $|\psi^{(2)}(x,t'')\rangle$ is depicted at early time in Figure 1.3. After some time-delay τ the vibrational coherence is

interrogated by the action of a third probe (pr) pulse;

$$E_{pr}(t,\tau) = E_{0,pr}e^{-(\frac{t-\tau}{\sqrt{2}\Delta t})^2}e^{-i\omega_{pr}t} \tag{2.5}$$

which excites the vibrational wavepacket to another non-resonant or resonant excited state $|\psi^{(3)}(x,t)\rangle$;

$$|\psi^{(3)}(x,t''')\rangle = -i\int_{-\infty}^{\tau_3} e^{-iH_{mol}(t'')}\mu_{vi'}(x)E_{pr}(t'',\tau_3)|\psi^{(2)}(t'')\rangle dt'' \tag{2.6}$$

creating the tr-CARS polarization.[17] Integrating over the square of the polarization results in the measured signal;

$$S_{CARS}(t) = \int_{-\infty}^{\infty} dt|P^{(3)}(\tau)|^2 = \int_{-\infty}^{\infty} dt|\left\langle \psi^{(0)}(t)\,|\mu|\,\psi^{(3)}_{\mathbf{E}_p-\mathbf{E}_s+\mathbf{E}_{pr}}(t)\right\rangle + C.C.|^2 \tag{2.7}$$

from which the wavepacket can spontaneously relax to the ground state accompanied by the emission of an anti-Stokes(AS) photon. If the spontaneous emission is from a real state, a subsequent re-emission can occur shortly thereafter. The anti-Stokes photon contains information about the relative phase of the vibrational coherence for each time delay τ_3. The AS photon satisfies the energy conservation condition;

$$\omega_{anti-Stokes} = \omega_{pump} - \omega_{Stokes} + \omega_{probe} \tag{2.8}$$

In an ensemble, or a bulk medium, which contains a thick sample of polarize-able material, the third order polarization will also have an associated momentum vector, which is also conserved;

$$k_{anti-Stokes} = k_{pump} - k_{Stokes} + k_{probe} \tag{2.9}$$

In a collinear mixing case, collection of the AS photon is background free when using three

different color pulses or when the three pulses do not overlap in time. Spatial filtering is also possible when the wave vector momentum conservation is revisited in the BOXCAR geometry, where the three pulses are mixed non-collinearly.[151] To derive the time dependent signal the third order polarization for the CARS pathway is considered. [157] Note, this approach neglects certain contributions that may arise from pre-populated vibrational states, i.e. $\hbar\omega_p - \hbar\omega_S >> kT$. The measured third order polarization arises from the time ordered interaction of the three pulses;

$$\begin{aligned} P^{(3)}(x,t) &= \frac{-i}{\hbar^3}\sum_{givi'} p_g \mu_{i'g}(x) \int_{-\infty}^{t}\int_{-\infty}^{\tau_3}\int_{-\infty}^{\tau_2} (e^{-iE_{i'g}(t-\tau_3)}\mu_{i'v}(x)E_{pr}(\tau_3)e^{-iE_{vg}(\tau_3-\tau_2)} \\ &\qquad \mu_{vi}(x)E_s^*(\tau_2)e^{-iE_{ig}(\tau_2-\tau_1)}\mu_{ig}(x)E_p(\tau_1) + c.c.)d\tau_3 d\tau_2 d\tau_1 \end{aligned} \tag{2.10}$$

This expression integrates over the action of each time-ordered pulse and the subsequent evolution on the respective excited state. In the case of resonant CARS, the states denoted by i and i' (or ii) are real electronic eigenstates of the system where wavepacket evolution may occur and spontaneously emit in absence of a stimulating electric field.

The above description takes into account the possibility of evolving on all states. In non-resonant tr-CARS where states i and i' are imaginary states, no evolution can occur, hence further simplifications can be made. The action of the pump pulse at τ_1 occurs at $t = 0$, Due to the fact that state i is a virtual state, τ_2 must also be set to $t = 0$. The lack of resonance dictates that the optimum transition conditions are achieved when the pump and Stokes pulse overlap in time. The action of the probe pulse, in the non-resonant case, will only spectrally shift the relative phase of the evolving vibrations and give rise to the AS photon. By energy conservation the spectral distribution of $|\psi^{(2)}(x,t)\rangle$ is described by the

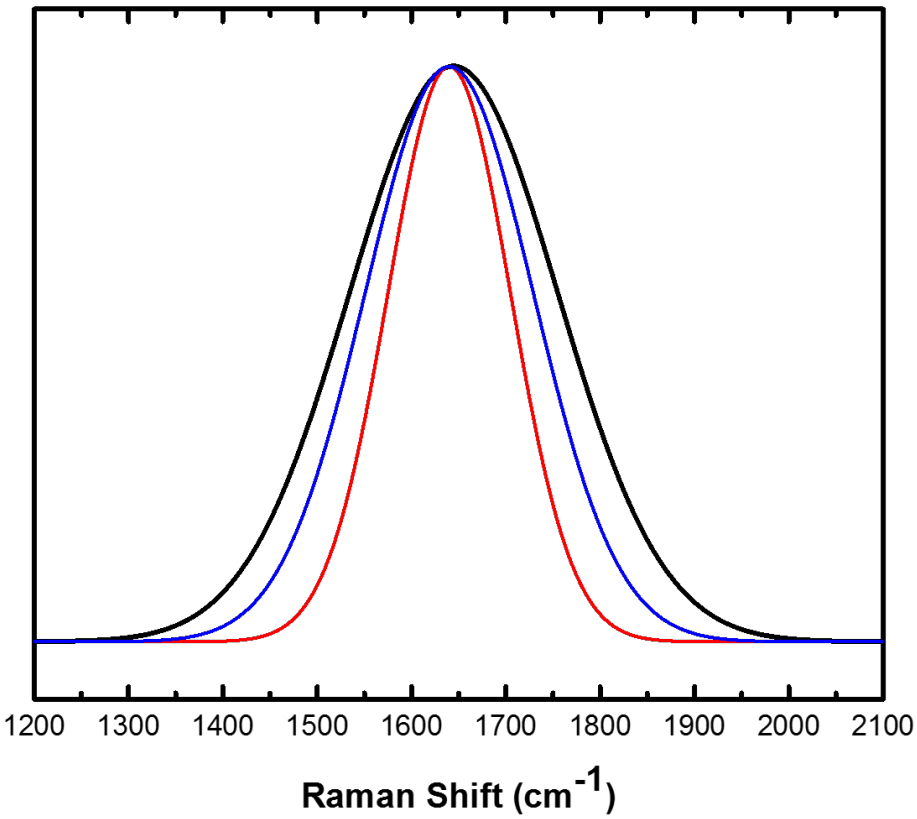

Figure 2.4: The pulses(pump in red and Stokes in blue), convolved in the spectral domain. Tuned by the difference between the pump and Stokes pulses, the convolution selectively excites vibrational eigenstates $E_v = \omega_p - \omega_S$ that fall within its spectral domain

spectral convolution of the E_{pu} and E_{Stokes} pulses depicted in Figure 1.4;

$$E(\omega) = \int_{-\infty}^{\infty} E_p(\omega') E_s^*(\omega - \omega') d\omega' \tag{2.11}$$

The vibrational wavepacket, prepared at $t = 0$ is the superposition;

$$\psi^{(2)}(x,t) = \sum_{i=1} \psi_v(x) a_i e^{-\imath E_i t} \tag{2.12}$$

where $\psi(x)$ is the spatial wavefunction with amplitude $a_i = E(\omega)\delta[\omega - E_i/\hbar]$ dictated by the two pulse convolution described in Eq. (2.11), E_i is the energy of the vibrational eigenstate i. The evolving vibrational coherence $|\psi^{(2)}\rangle\langle\psi^{(0)}|$ is then interrogated by the time-delayed probe pulse. The time integration, Eq. (2.9), by a photodetector washes out the carrier frequency, and the signal is reduced to the sum of relative phases between the prepared vibrational eigenstates. For a two eigenstate superposition;

$$|\psi^{(2)}(t)|^2 = |\sum_{i=1}^{2} a_i e^{-i\frac{E_i}{\hbar}t}|^2 = (a_1 e^{i\frac{E_1}{\hbar}t} + a_2 e^{i\frac{E_2}{\hbar}t})(a_1 e^{-i\frac{E_1}{\hbar}t} + a_2 e^{-i\frac{E_2}{\hbar}t}) \tag{2.13}$$

Using $E = \hbar\omega$, the measured signal is reduced to;

$$\begin{aligned}
&a_1^2 e^{-i(\omega_1-\omega_1)t} + a_1 a_2 e^{-i(\omega_1-\omega_2)t} + a_2 a_1 e^{-i(\omega_2-\omega_1)t} + a_2^2 e^{-i(\omega_2-\omega_2)t} = \\
&= a_1^2 + a_2^2 + a_1 a_2 e^{-i(\omega_1-\omega_2)t} + a_2 a_1 e^{i(\omega_1-\omega_2)t} = \\
&= a_1^2 + a_2^2 + a_1 a_2 (cos[(\omega_1 - \omega_2)t] - isin[(\omega_1 - \omega_2)t]) \\
&+ a_2 a_1 (cos[(\omega_2 - \omega_1)t] + isin[(\omega_2 - \omega_1)t]) = \\
&= a_1^2 + a_2^2 + 2(a_1 a_2) cos[(\omega_1 - \omega_2)t]
\end{aligned}$$

The signal is the beat frequency between the two vibrational bands above a constant background. In general, the coherence measurement, which probes the off-diagonal density matrix elements, describes the difference frequency between all excited vibrational bands. The measured quantity at any time delay is the sum over all transition frequencies squared. The finite linewidth of transitions implies a phase distribution in the evolving coherence. At early delay times, the phases can be described by a normal distribution function with a variance that is proportional to the delay time of the probe. At sufficiently large delay times the phase distribution becomes uniform and the expectation value of the phases goes to zero.

This behavior is an inherent property of the ensemble known as pure dephasing, denoted by T_2^* [157]. The ensemble eigenstate bands are described by a homogeneous distribution, the inverse width of which is the lifetime of the eigenstate T_1. In the above example, the eigenstates are spectral delta-functions, subject to no decay $T_1 \to \infty$. Typically, in a tr-CARS measurement on an ensemble, pure dephasing will scramble the measured phase long before the vibrational vibrational eigenstates decay. The overall decoherence time of the signal, T_2, is a combination of these two factors;

$$\frac{1}{T_2} = \frac{1}{2T_1} + \frac{1}{T_2^*} \tag{2.14}$$

2.8 tr-CARS on a Single Molecule

The tr-CARS signal is proportional to n^2, where n is the number of molecules in the excitation volume. [158] To execute a tr-CARS measurement on a single molecule, the one photon response must be enhanced. Surface enhanced Raman scattering (SERS) has enabled detection of trace quantities of molecules that are highly diluted in their local environments. [159–162] SERS has been extended and studied in various configurations: thin films [163, 164], colloidal particles [165, 166], and nanowires [167]. The enhancement of the detected vibrational fingerprint is made possible by simultaneously excited plasmon modes of a nearby metallic structure. In the presence of an electric field, a metal nanosphere's surface electron density will oscillate at the frequency of the incident electric field [168, 169]. However, when there are two spheres in very close proximity, given the optimum incident field polarization, a dipole is created at the nanometer junction of the two spheres that is much greater in amplitude and oscillates with the incident electric field. The focused excitation junction is roughly a few molecules in size, allowing for a greater probability of catching a single molecule in action. [170, 171] In addition to the concentrated excitation, the emitted anti-Stokes photon

from the molecule located in the junction, drives the collective electrons of the spheres. The anti-Stokes radiation is thus amplified proportional to the oscillator strength of the plasmon. If the incident electric field satisfies the surface plasmon resonance condition of a particular material and structure(in this case, a pair of spheres), then the amplitude of the field is also significantly increased at the junction(between the spheres).[172, 173] Raman intensity scales as $|E_0|^2$, in SERS, this relationship is $|E_0|^4$ as both the driving field, and the molecular response is enhanced. Following the enhancement of two fields in SERS, we expect the CARS photon, a phenomenon involving four fields, to have $|E_0|^8$ enhancement[174]. In Chapter 4, the results of the first instance time resolved surface enhanced coherent anti-Stokes Raman scattering measurements are reported, and the characteristics explained.

Chapter 3

Design and Construction of Experimental Apparatuses

The millenial advent of low noise solid state laser systems provides robust femtosecond pulses[175], which allow for clocking molecular coherence dynamics on their natural timescale. Commercially available fiber and free space laser systems, including but not limited to titanium sapphire[176] and erbium fiber[177] oscillators are but a few sources that are capable of covering different regions in the near-infrared spectral regions with broadband femtosecond pulses at repetition rates in the MHz region. However, in order to design a system that is universally capable of initiating and probing a photophysical change across a library of molecular systems, each with their unique absorption and emission fingerprints, the range provided by the above NIR systems fails to meet the requirements alone.

Spontaneous Parametric Down Conversion(SPDC)[178], a nonlinear process in which a photon can be split into two lower energy photons, allows for the tunable extension to the incident source light. Coupling this phenomenon with commercially available femtosecond oscillators allows for robust tunability by using an Optical Parametric Oscillator(OPO)[179].

Alternatively, if the initial 800nm output of the titanium sapphire, or the 1064nm output of the Erbium fiber oscillators can be amplified via Chirped Pulse Amplification[180], thus providing a peak pulse power 10^9 times higher than the initial input, Optical Parametric Amplification(OPA)[181] can be used.

While the peak power provided by the OPO is lower, its repetition rate is on the order of MHz, more suitable for microscopy applications where the number of reporters in the focal volume is limited. Higher repetition rates in this case allow for more signal photons per second for the detection to collect. OPAs allows for higher peak power but at a significantly lower repetition rate of kHz. OPA is more suited for experiments concerning ensemble measurements where the focal region is generally much larger, thus encompassing a larger concentration of reporters for easier collection. The higher peak power allows the output of an OPA to be frequency doubled to extend the accessible tunability into shorter or longer wavelengths.

The following covers the fundamental principles behind non-collinear optical parametric amplification and the design of three individually tunable, synchronously pumped, optical parametric amplifiers, which allow for background free Four Wave Mixing (FWM) measurements on virtually any molecular system. It is apparent that to reach the single molecule limit in nonlinear spectroscopy, the higher repetition rate OPO is much more adept due to the flux of signal photons generated. Though the system was not used in any single molecule measurements, the concepts and designs governing wavelength conversion and pulse characterization techniques discussed here are applied in later experiments involving single molecules measured with 80 MHz and 250 kHz laser systems, also employing optical parametric generation.

3.1 Noncolinear Optical Parametric Amplifiers (NOPA)

An optical parametric amplifier consists of two parts; a weak broadband spectrum used as the seed, which provides the source bandwidth of the optical parametric amplifier, and a high power pump, usually, the second harmonic (SHG) of the commercial chirped pulse amplifier driving the OPA.

3.1.1 White Light Generation

At the expense of a small portion of the available laser power, white light continuum[182], the seed for the OPA, can be generated by focusing the output of a chirped pulse amplifier into virtually any medium but typically chosen from either sapphire, calcium fluoride, yttrium aluminum garnet(YAG) or water. The advantages of each are well documented and beyond the scope of this thesis. At an irradiance threshold unique but relatively similar for each of these media, the pump light undergoes Kerr lensing[183] and self focuses via the nonlinear refractive index change

$$n = n_0 + n_2 I \tag{3.1}$$

that is known as the optical Kerr effect, where n is the refractive index of the medium and I is the intensity of the pump beam. For a Gaussian beam in space, this effectively means that the refractive index will be higher in the center of the beam causing the light to travel slower, than the outside, while also generating self focusing. The result to an observer, as opposed to an otherwise normal beam waist, the region of the waist appears to be a single filament, or an elongated beam waist. The generation of new frequencies is the result of the

changing phase due to the nonlinear index of refraction via the Kerr effect;

$$\omega_{WLC} = \frac{\partial\phi(t)}{\partial t} = \omega_{pump} - n_2 \frac{\omega_{pump}}{c} z \frac{\partial I(t)}{\partial t} \tag{3.2}$$

An increased intensity(in the center of the beam) leads to a red shift in the frequency while a lower intensity(in the wings) leads to a blue shift[184]. The newly generated frequencies interfere with those already present in the incident pulse. Constructive interference leads to generation of a broad continuum[185] up to an octave on the blue and red wings of the incident laser pulse that serves as the seed for the Optical Parametric Amplifier.

3.1.2 Second Harmonic Generation

The pump for the OPA in our case is the frequency doubled output of the 775nm chirped pulse amplifier. To double the frequency of the laser light, two 775nm photons are combined in a nonlinear BBO crystal to create one 387nm photon that propagates collinearly with the undoubled portion of the incident light source. The conversion efficiency cannot be greater than 50 % and is typically on the order of 30 % for broadband pulses. Adjustments can be made to spectrally disperse the incident pump light before focusing into the nonlinear medium so as to better phase match the incident pump photons with the newly generated SHG photons for a higher conversion efficiency.

3.1.3 NOPA

The pump and seed arms have been described, and the optical parametric amplification can occur in another nonlinear medium when the two are combined in space and time. A simplified NOPA schematic is depicted in Figure 3.1. The SHG pulse is focused into a nonlinear medium to generate spontaneous parametric down conversion(SPDC). The down

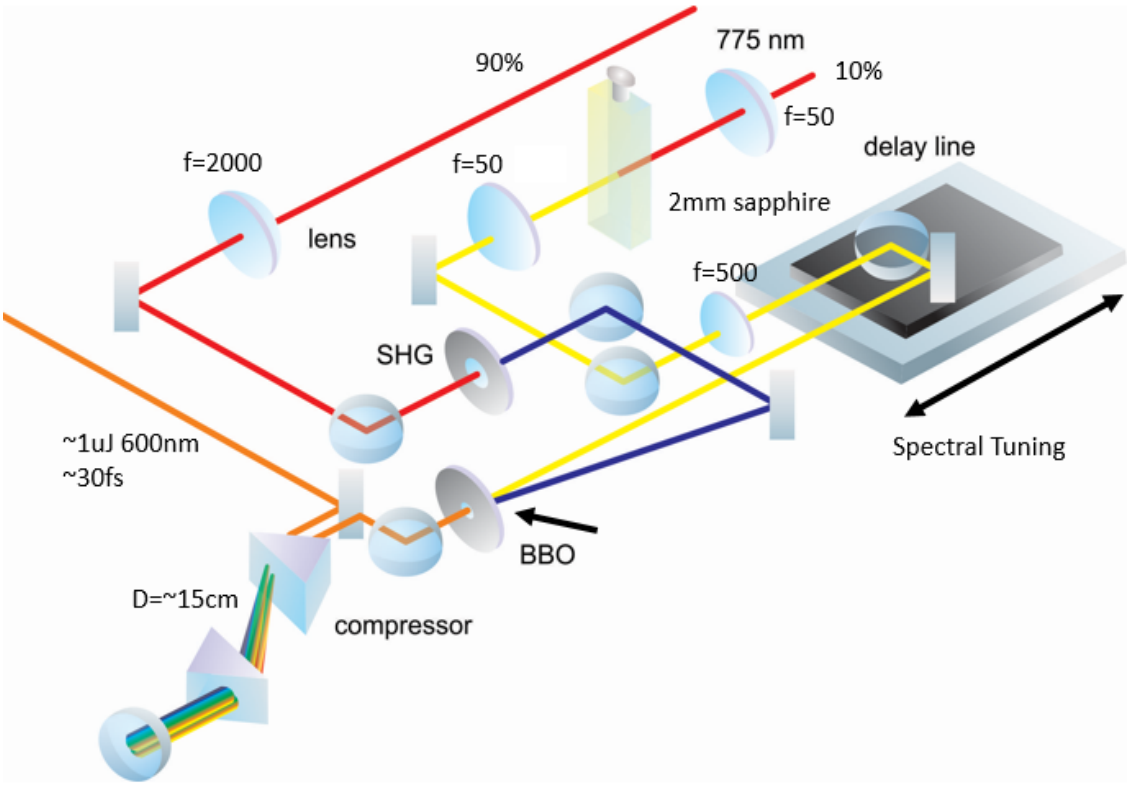

Figure 3.1: A general schematic for a Non-collinear Optical Parametric Amplifier. Light is split 90/10 (not shown), with 10 % used for generation of WLC. The 90% is used to for generation of SHG which drives the SPDC in a nonlinear BBO crystal. Spectral tuning of the OPA is accomplished via spatiotemporal overlap between the WLC and the signal photons that arise from parametric down conversion. The output is passed through a folded prism compressor to manipulate the chirp profile of the pulse.

conversion splits the SHG light into two photons whose combined energies reconstruct the energy of the original SHG photon;

$$\omega_{pump} = \omega_{signal} + \omega_{idler} \tag{3.3}$$

The two new photons, dubbed the signal (for the higher energy photon) and idler(for the lower energy photon) are generated in the process. The mechanics for such a process are highlighted in Figure 3.3 In a collinear regime, the idler photons travel through the medium faster than the signal photons as the lower frequencies see a lower index of refraction and are diffracted less than the higher frequency signal photons (as per Snell's law, depicted in

bottom left of figure)[186]. Each pair of photons generated are entangled, and there cannot be more idler than signal photons and visa versa. In this regime, group velocity mismatch conditions dictate that the newly generated signal photons add to the leading edge of the signal pulse and and the new idler photons add to the trailing edge of the idler pulse (in time). The consequence is that the newly generated tunable bandwidth cannot support a pulsewidth shorter than the one used to generate it. In addition, the amplification is hampered by the group velocity mismatch between the pump and the signal and idler photons due to the minimal interaction length in the nonlinear crystal. The mismatch between the signal and idler photons serves to limit the bandwidth that can be amplified.

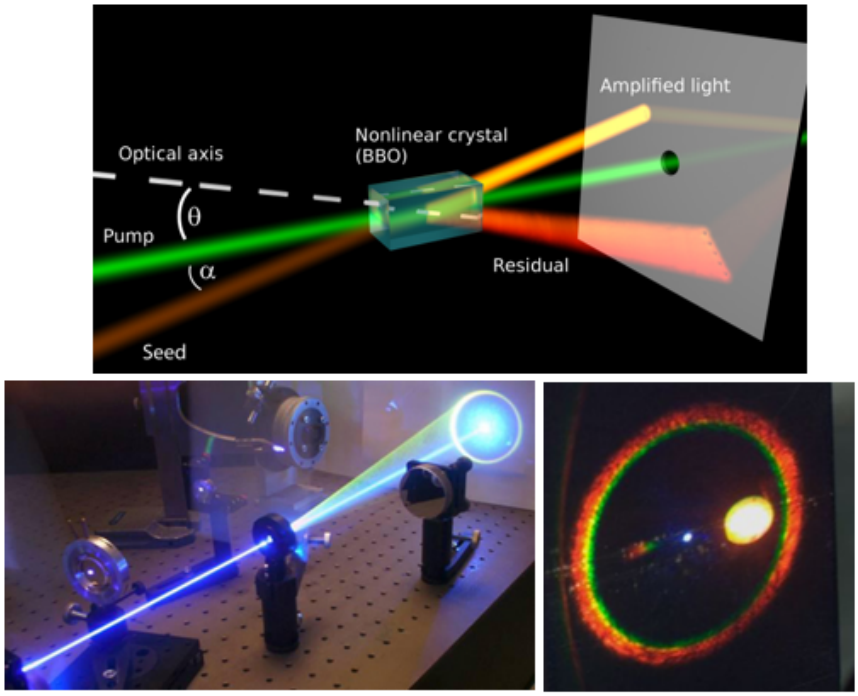

Figure 3.2: Spontaneous Parametric Down Conversion (SPDC) is the essence behind optical parametric amplification. An incident photon is split into two photons conserving momentum and energy. Pictured here, a 400 nm beam is split into the signal, and idler photons. The solution to the momentum conservation is a cone about the propagation direction of the incident light source. The result is a plethora of all possible two photon combinations that make up the incident source light emerging in in a bright superfluorescent ring

Non-collinear generation[187] of the signal and idler pulses allows to maximize the group

velocity mismatch between the pump and generated photons as well as the mismatch between the generate photons themselves while still obeying the momentum conservation principle;

$$k_{pump} = k_{signal} + k_{idler} \tag{3.4}$$

Assuming the WLC and the pump beam are overlapped in space and time in a nonlinear crystal with the WLC being collinear to the signal photons, a comparison between the collinear and non-collinear idler and signal regimes, is shown in Figure 3.3.

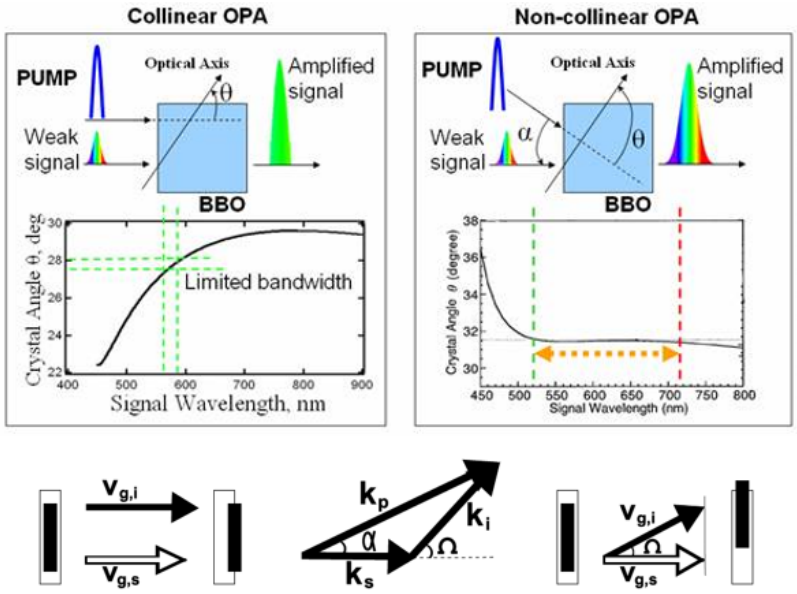

Figure 3.3: A comparison of collinear and non collinear optical parametric amplification. In the case where the seed and pump are mixed collinearly, the amplified bandwidth depends greatly on the crystal angle. The idler and the signal photons propagate collinearly, the the bluer signal trailing the idler pulse, resulting in less temporal overlap of the entangle photon pair. In the non-collinear case, there exists an ideal angle between the pump and the seed light where the signal and idler remain optimally overlapped in time allowing amplification of a significantly broader bandwidth for a given crystal angle.

On the bottom left, the collinear regime depicts the scenario described earlier, where the

signal photons are added on the leading edge of the signal pulse and visa versa due to group velocity mismatch. This leads to a narrow bandwidth for amplification at any given crystal angle relative to the incident pump light(top left). If the signal(WLC) and the idler are mixed noncollinearly (bottom, middle), the group velocity mismatch is maximized[188, 189] (bottom right) and virtually the entirety of the visible light spectrum can be amplified for the given crystal angle Ω (top right). The generated signal and idler beams emerge in a cone from the nonlinear medium used to generate SPDC and is depicted in Figure 3.2 The conditions for optimum phase matching is derived starting from the phase matching condition projected parallel;

$$\Delta k_{\parallel} = k_{pump} Cos[\alpha - k_{signal} - k_{idler}] Cos[\Omega] \tag{3.5}$$

and perpendicular;

$$\Delta k_{\perp} = k_{pump} Sin[\alpha - k_{idler}] Sin[\Omega] \tag{3.6}$$

to the signal wavevector. To maximize the phase matching, both the parallel and the perpendicular terms must equal 0, so that;

$$v_{g,s} = v_{g,i} Cos[\Omega] \tag{3.7}$$

To derive the angle α, the angle between the pump and the signal photons, or rather the pump and the WLC which is collinear with the signal photons for optical parametric amplification to occur;

$$\alpha = ArcSin[\frac{1 - \frac{v_{g,s}^2}{v_{g,i}^2}}{1 + 2\frac{v_{g,s} n_s \lambda_i}{v_{g,i} n_i \lambda_s} + \frac{n_s^2 \lambda_i^2}{n_i^2 \lambda_s^2}}] \tag{3.8}$$

Optimization[190] of α allows for easy generation of bandwidths that support sub 20 fs pulse

lengths[188, 191]. Although the bandwidth is sufficient to support a short pulse upon exiting the mixing stage, the pulse is chirped due to all the optics that add positive group velocity dispersion to the pulse and can be compensated by implementing pulse compression.

3.1.4 Pulse Compression

There are various ways to compress a pulse that has/will accrued/accrue positive GVD in the path of propagation[192]. The simplest of these options is a folded prism compressor as depicted in Figure 3.4

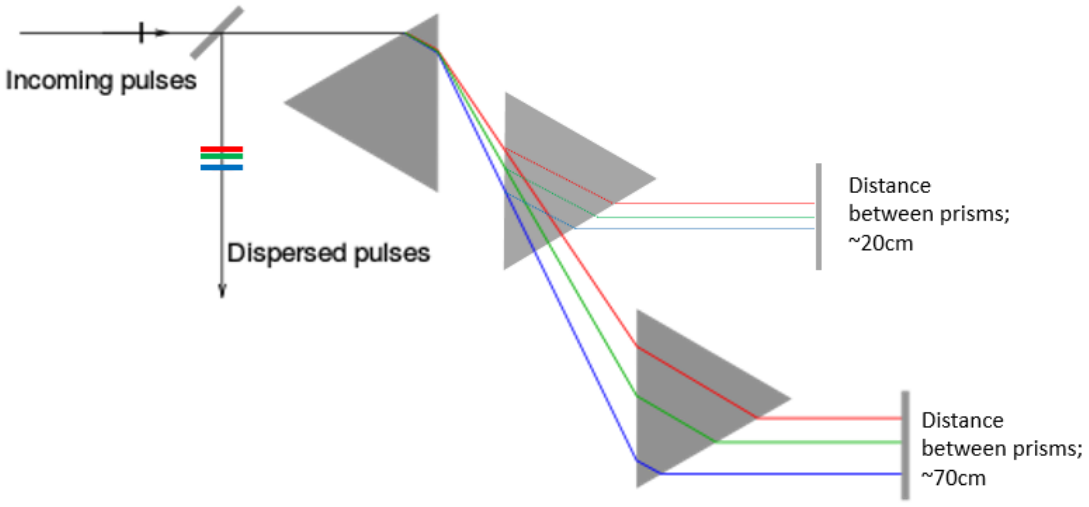

Figure 3.4: A discrete way to manipulate the linear chirp profile of an ultrafast laser pulse. By sending light through a prism, the beam is separated by color, with the bluer tail bending the most. A second prism is placed in the path and "collimates" the angular dispersion initiated by the first prism. For a pulse with positive linear chirp, the redder colors traverse more distance in the prism and travel slower than they would otherwise in air, allowing the bluer colors a chance to catch up in time. The beams are retroreflected back through both prisms and exit the compressor free of angular dispersion, with a modified chirp profile if both prisms are at the minimum deviation angle w.r.t. th incoming beam.

The beam enters the first prism, cut at Brewster's angle, at the angle of minimum deviation,

and the beam begins to spectrally disperse. Another prism is placed at a specified point in the path of the dispersed light, perpendicular to its trajectory, also at the angle of minimum deviation. The farther the distance between the prisms, the more time the redder wing of the pulse spends traveling through the second prism relative to the blue wing of the pulse, giving the blue wing of the pulse time to catch up to the red wing of the pulse in time. The beam is then retroreflected back to the 2nd prism, and angled slightly downward to be picked off below the beam incoming to the first prism. If both prisms are aligned at the angle of minimum deviation and are level with respect to the beam, the output has no angular dispersion. The net effect of such an apparatus is an overall negative GVD on the pulse. Appropriate choice of distance between the prisms can compensate for any amount of positive GVD accrued before/after the pulse compressor. The second prism can sit on a linear delay stage to fine tune the negative GVD added to the pulse.

3.1.5 Pulse Characterization

To ensure that the pulse is at its transform limit, characterization of the pulse in time will take place to verify that there exists no chirp on the pulse before any experiment is performed. If there exists positive or negative chirp in the pulse it will manifest as the red or blue end on the leading edge of the time correlation. Second Harmonic Generation Frequency Resolved Optical Gating (SHG-FROG)[193] allows for a trivial way to intensity autocorrelate any ultrafast pulse. However SHG is a $\chi^{(2)}$ effect, as it takes two photons and gives the Sum Frequency photon intensity as a function of delay of one pulse relative to another (or the Second harmonic if the two photons are degenerate). Figure 3.5 depicts a general schematic for measuring the intensity autocorrelation using Second Harmonic Generation.

The pulse is split via a beamsplitter, with one arm passing through a variable delay stage controlled by a computer. The beams are made parallel and focused into a thin nonlinear

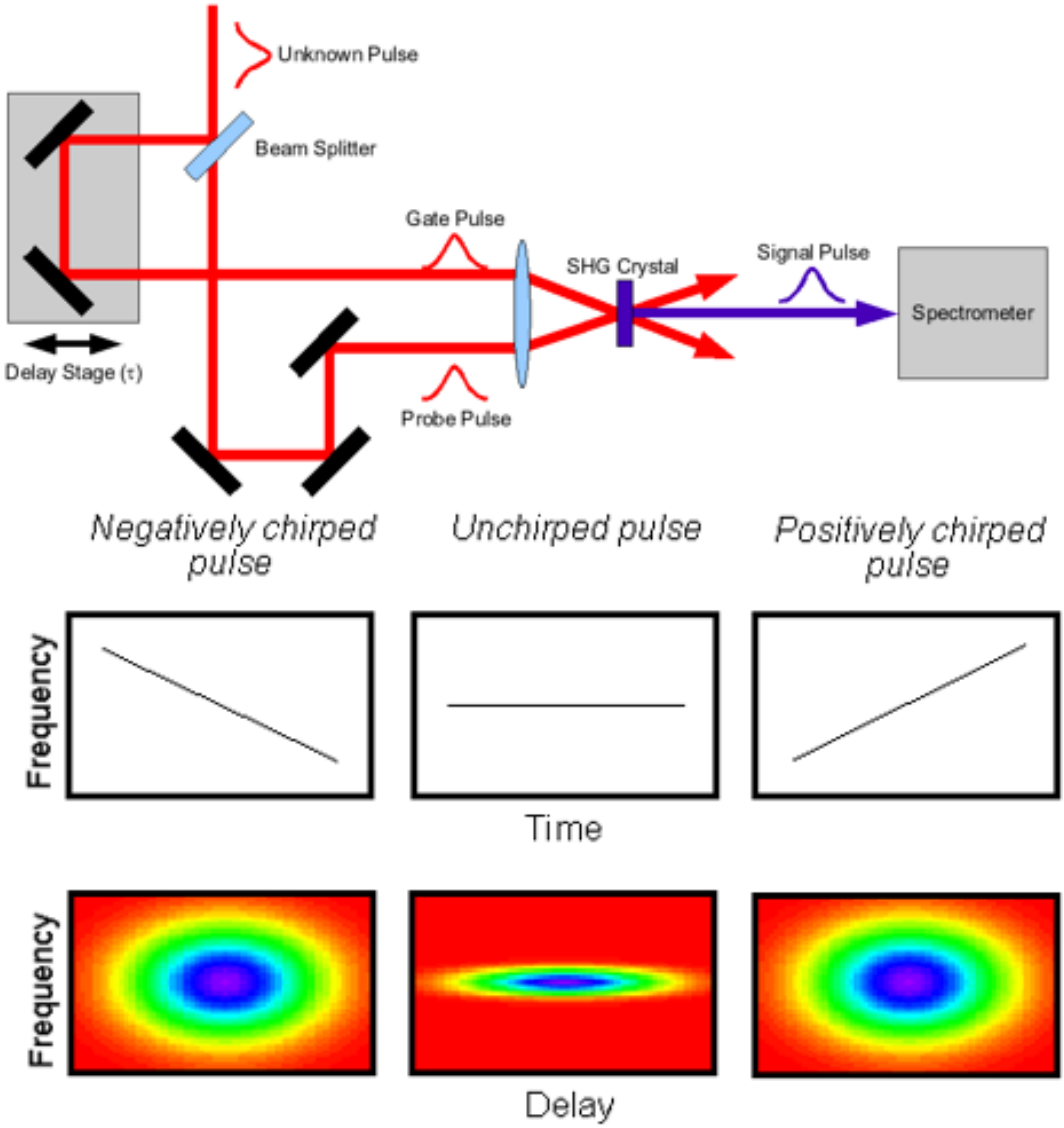

Figure 3.5: Typical schematic for Second Harmonic Generation Frequency Resolved Optical Gating. This technique allows measuring the spectral distribution of a pulse in time. However the technique cannot distinguish between negative and positive chirp of the incoming pulse.

crystal (the thinner the better, for less GVD). The crystal is tuned such that the second harmonic of both arms can be generated. If the pulses are overlapped in the crystal in space and in time, a "sum-frequency" signal will emerge in between the two beams after passing through the crystal. The intensity of the newly generated beam depends on the delay of one arm relative to the other. The delay can be scanned and correlated with a spectral

intensity, collected by a spectrometer to extract the pulsewidth of the beam. For a beam to be considered transform limited, or as compressed as it can be via the undertainty principle, the condition of the time bandwidth product

$$\Delta\omega\Delta t \geq 0.441 \tag{3.9}$$

must be met[194]. Here the $\Delta\omega$ is in Hz and Δt is in seconds. However one of the caveats with using such a simple autocorrelation method is that it cannot differentiate between positive or negative chirp. If the incident pulse is positively chirped, but the user does not know this and runs an SHG-FROG trace, the user will not know whether to put more of the second prism into the beam or to take it out. The trivial approach would be to try to put in more prism (for instance) and see if the pulse width decreases. If that is true, then the user can continue to put more prism into the beam until the pulse begins elongating again after reaching a minimum. Though there is some guesswork involved, the method will serve to characterize and correct for negative/positive chirp. Among the many other available methods of pulse characterization (MIIPS[195], SPIDER[196], etc...) there exists another simple solution which also does not require a nonlinear crystal (though it does help). This method, dubbed time-resolved Self-Diffraction(tr-SD), allows for full chirp characterization of the pulse and can be executed in any mixing medium (other than air). While the majority of the setup remains the same as the above mentioned SHG-FROG, the collection point, as well as the mixing medium are different. The main difference is highlighted in Figure 3.6.

As opposed to using a nonlinear crystal to mix the beams, allowing for a SHG signal to emerge between the mixing beams, this method relies on using a photon from both arms to generate a transient grating in a mixing material[197]. This grating only exists for the duration of the pulse overlap of the two photons. This transient grating has ruling Λ which is defined as grooves/mm, for two beams incident onto the glass at a half angle α. A third photon, from either of the beams k_1 or k_2, will scatter off this transient grating at angle β

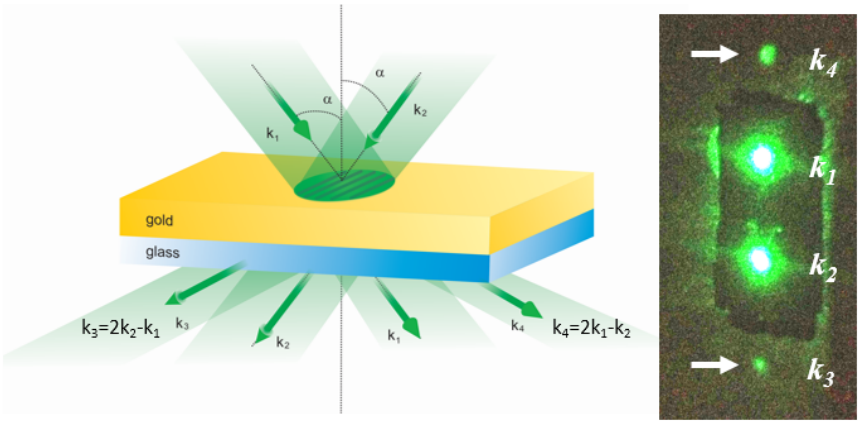

Figure 3.6: Self Diffraction pulse characterization. By overlapping two beams on any optically transparent material in time and space, a population grating is created. This holographic grating scatters a third photon from either of the two incident pulses producing a diffracted beam that can be used to characterize the pulse and chirp temporal and spectral profiles.

on the other side of the glass. This relationship is dictated by;

$$\Lambda(Sin[\alpha] - Sin[\beta]) = m\lambda \tag{3.10}$$

where m is the diffraction order, and lambda is the wavelength of the incident light (assuming the two beams are degenerate in color). For a diffraction order of m = 1, the diffracted beam k_3 and k_4 obey momentum conservation and result from the third photon coming from k_2 and k_1 respectively. Higher order diffraction can occur in which case there is a (m+2)th photon coming from the respective incident field. Generally this can occur if the interaction medium is long enough or if there is excess peak power in the pulse. Note that this effect is more pronounced and the generated diffraction is more intense as the pulse gets closer to its transform limit. So in effect, one way of judging the pulsewidth is to scan the second prism of the beam being characterized and monitor for a peak in the brightness of the diffracted beams (inset in Figure 3.6). Note that this is a four wave mixing measurement, but unlike a FWM measurement on a molecule, glass does not have any real resonances in the visible light region and so the diffraction will only occur if the incident pulses k_1 and k_2 overlap in time (and

space). Another note is that the mixing medium can be anything without any real resonances or photon echoes to add features to the characterization. This is because unlike SHG-FROG which is measures $\chi^{(2)}$ effect and requires anisotropy of the mixing medium, Self Diffraction is a $\chi^{(3)}$ measurement which can be performed on any isotropic medium. The other key difference is that when characterizing with SHG-FROG, characterization takes place in one medium while the measurement takes place in another (usually a cuvette if the system being measured is liquid). Characterizing in one substance to measure in another is not advised when using short (sub 50 fs) pulses as the two add different GVD to the pulses; while the pulses appear transform limited in SHG-FROG, they can develop strange temporal profiles in the sample. tr-SD allows to characterize the pulses being used in the same sampleholder as the system of interest will be in. One can even obtain an instrument response function by measuring tr-SD in a cuvette filled with solvent, in absence of the system of interest. This guarantees truly background free pulse characterization. One major downside of tr-SD over SHG-FROG is that it requires significantly more intensity as the process is a higher degree of nonlinearity than its counterparts, and it may be difficult to find the diffracting orders upon overlap in time and space if the compression of the beams is very far from optimum. To this deficit, we propose that a rough compression be performed by firstly putting the beam through a nonlinear crystal to generate its second harmonic frequency, and the 2nd prism be optimized on the intensity of the generated second harmonic light before executing tr-SD. This will put the compression close to transform limit and ensure that the diffracted orders can be observed in tr-SD. To methodically ensure a transform limited pulse, if one of the diffracted order is examined with a spectrometer as a function of delay, time, if the delay is in the negative time regime (where the pulse from the variable delay pulse is incident on the mixing medium before the fixed delay pulse) and the diffracted order scans from blue wing to the red wing of the spectrum as a function of delay into positive time, then the pulse has excess negative GVD. The second prism should be placed further into the beam path. If the opposite is true, and the red wing emerges first at negative time, then less prism

is prescribed. If the edge of the prism is reached in either direction without finding the shortest pulse, or the point where the red and blue wings come coincidently when scanned from negative to positive time, then the distance between the prisms must be adjusted. See the Appendix for the calculation that determines the correct distance between the prisms for a given input pulsewidth and wavelength.

3.2 Three Individually Tunable Synchronously Pumped Optical Parametric Amplifiers at 1 kHz

In order to be universally equipped to perform four wave mixing measurements on on any molecular system, three of such NOPAs described previously are required. Two can be tuned degeneratively to to create a population grating on a resonant state while a third can be time delayed relative to the first two to monitor the evolution of the population. Likewise, the two preparatory pulses can be nondegenerate to prepare a coherence on an electronic state, while a third one scans this coherence. Two nondegenerate pulses can be used to prepare a coherent superposition on the ground electronic state of a system, far below an electronic resonance and the evolution be monitored with a third unique color. Below follows a rough description of the design of three individually tunable synchronously pumped NOPAs for use in any Four Wave Mixing measurements as depicted in Figure 3.7.

The above design is unique from all commercially available wavelength conversion options in a few features that will be outlined. The system is pumped by a commercially available chirped pulse amplifier (Clark MXR CPA-2001) that provides the system with 850 μJ pulses centered at $\lambda = 775$nm with a pulse width of 150 fs and a repetition rate of 1 kHz. The amplifier is seeded by a 30MHz erbium doped fiber oscillator that outputs 30mW of 1550 nm light, frequency doubled to 3 mW of 775nm via a temperature tuned periodically poled

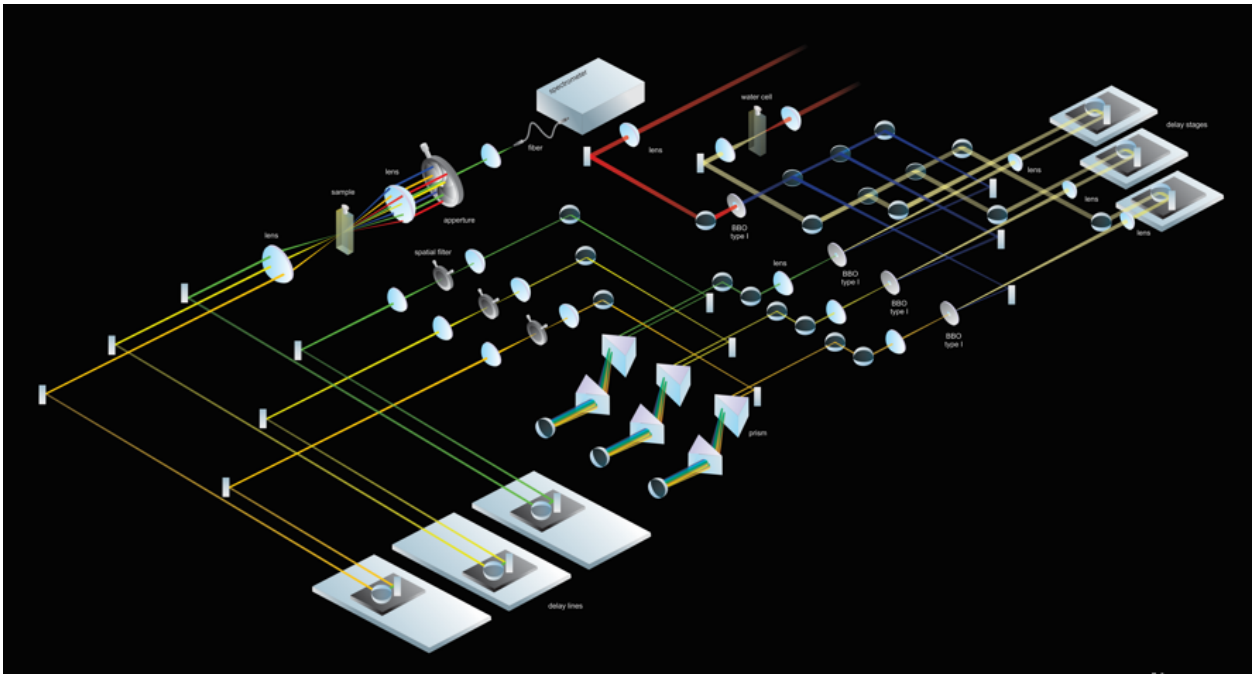

Figure 3.7: A schematic for three synchronously pumped independently tunable optical parametric amplifiers. All three amplifiers are seeded and pumped by a common WLC and SHG source. Each OPA has its own prism compressor, telescope with a spatial filter, and an electronically controlled time delay stage. The three OPAs are overlapped in time and space in a sample and generate a fourth spectrally unique color which contains the sample response. The generated beam is sent to be spectrally filtered and collected in a monochromator/CCD combination.

lithium niobate(PPLN) crystal. The femtosecond seed is then stretched to picoseconds via a grating stretcher, and sent to the chirped pulse amplifier that is pumped by a 1 kHz nanosecond intracavity frequency doubled Nd:YAG at 532nm. The seed is passed through a faraday rotator on its way into the amplifier cavity to ensure no back reflections are sent into the oscillator that may destabilize the modelock, and enters the cavity via a polarizing beamsplitter cube(PBSC). The seed then passes through a Pockels Cell which rotates the polarization to keep the seed in the amplifier cavity so that it passes through the PBSC that reflected it into the cavity and onto the population inverted Ti:Sapphire crystal where it is amplified. The 532nm pump beam has a duration of nanoseconds, which allows replenishment of the population inversion in the Ti:Sapphire gain medium while the seed pulse propagates through one round trip in the cavity. The seed pulse is amplified via 3-4 round

trips through the cavity, at which point the Pockels cell again switches the polarization of the amplified seed so that it may exit the cavity through the PBSC that reflected it into the cavity. The amplified beam once again passes through the Faraday rotator in the opposite direction from whence it came to pass through a PBSC that otherwise reflects the incoming unamplified seed. The amplified pulse travels through a telescope to enlarge the beam size so that it may not burn the grating as it becomes compressed. The large amplified pulse is compressed to 150 fs via a prism compressor and sent out of the amplifier to pump the optical parametric amplifiers for wavelength conversion. The fundamental output of the Clark is then split 90/10 with 10 % heading towards the WLC generation stage (included in the Figure). The 10 % light is passed through a half wave plate (HWP) and further cleaned by a PBSC for intensity attenuation, irised to control the beam diameter, and focused with a plano convex (PCX) lens over 150 mm into a 1 cm long cuvette filled with deionized water at room temperature. Optimization of the WLC is done by firstly positioning the lens such that the focus is after the water cuvette. The lens is slowly moved away from the cuvette until continuum is generated with a faint blue circle surrounding the continuum. If a red circle appears surrounding the blue, then the focus is in too deep and the lens should be moved forward towards the cuvette until only a blue circle is present. If the liquid appears to be bubbling, the intensity is too strong and must be attenuated via the HWP. If continuum cannot be generated then adjust the iris to allow a larger diameter beam through to the cuvette. After optimizing the WLC, the output is collimated with a PCX lens with a focal length of 100 mm. This WLC is the seed continuum for all three OPAs. Note that when the same continuum is used to generate all three OPAs, the quality of the spatiotemporal overlap when later used in FWM measurements is optimized. The WLC is split into 3 equal intensity arms via 2 broadband dichroic beamsplitters (for best results, use partially coated silver optical flats with a density of silver that reflects 70/30 and then 50/50, though note that if not coated with a protective layer, it will tarnish quickly and need to be replaced often). The three WLC arms are sent through three variable delay stages for optimizing

the temporal overlap with the pump beam in the nonlinear mixing crystal. After the delay stage, the beams are focused with a 500 mm lens into a 5x5x2 mm BBO Type II cut at θ = 32 degrees, ϕ = 0 degrees. BBO crystals are hygroscopic and will absorb the moisture out of the air. To prevent this, they come with two options; either a protective coating or with a heated mount. Protective coatings have a lower damage threshold than the bare BBO and so are subject to damage when irradiated with excess pump intensity. Heated crystals are sometimes bulky but are well worth it considering the effectively higher damage threshold. The WLC is ready for mixing. The 90 % is passed through a PCX lens with a focal length of 2 m. Approximately 1 m away from this lens is positioned a 10x10x0.5 mm BBO type I crystal cut at θ = 29.2 degrees and ϕ = 0 degrees. Heated BBO crystals can arguably produce a better rate of conversion however the irradiance of the fundamental 775nm is not sufficient to induce damage at this juncture so a protective coating may be used. The full output of the SHG light at 387nm is 240 μJ per pulse giving an effective conversion efficiency of 31.3 %. The SHG light is then split three ways via 2x beamsplitters and sent to join the WLC in the previously mentioned mixing BBO crystals, mixing just before the SHG light reaches the its beam waist (50 mm to waist after mixing crystal). The optimum mixing angle depends on the desired OPA color but is generally fixed at α = 3.7 degrees. Because the output of the Clark is P polarized, the mixing between the WLC and SHG has to happen vertically. Ideally, the WLC is propagating level to the table, and the SHG comes is reflected from beneath the WLC propagation plane. After spatial overlap between the WLC and SHG has been established while keeping the WLC propagating level with the table, the superfluorescence cone, generated by SPDC is adjusted by changing the angle of the BBO crystal such that the ring overlaps with the propagating WLC. If no rings are present, attempt to rotate the BBO while it is perpendicular to the SHG light until the rings appear. At 50 μJ of SHG power per NOPA, the rings should be clearly visible when the BBO crystal rotation has been optimized. When the spatiotemporal overlap of the WLC and SHG is established in the BBO, and the superfluorescence rings are overlapped with the

WLC, attempt to scan the WLC delay to find the temporal overlap. When the two arms are spatiotemporally overlapped the bright rings should collapse (not fully but by a significant amount) as the SPDC normally responsible for lighting up the rings is diverted to amplify the WLC. If no such phenomenon occurs, check the pathlengths of the SHG and WLC arms to ensure that they are within the travel distance of the WLC stage (starting from the 90/10 BS). Once the initial overlap is found, tunability can be adjusted via changing the delay of the WLC and the BBO crystal angle. The WLC has a pulse duration of 1ps and is heavily positively chirped. In the noncollinear mixing regime, the bandwidth of the generated OPA is strictly dictated by the spatiotemporal overlap of the WLC and SHG. The WLC can be precompressed to amplify a larger portion of the WLC, but only as long as spatial overlap is maintained and the superfluorescent rings are superimposed for all colors (α = 3.7 degrees). If alpha is varied, the rings split by color, and only the color that propagates with the WLC can be amplified. The tunability of the pulses used in experiments with this design is illustrated in Figure 3.8, spanning the majority of the visible light spectrum.

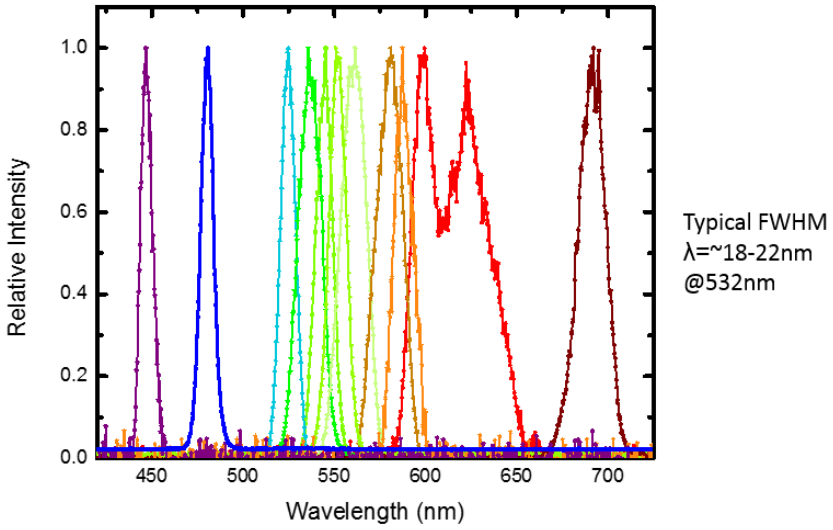

Figure 3.8: The spectral profiles of amplified pulses used in experiments. Typical bandwidth is 18-22 nm centered around 532 nm. The majority of the visible light region is easily reachable by all three NOPAs.

The typical output of each of the three OPAs is 1 μJ with a bandwidth capable of supporting 30 fs pulses. Assuming the input pulse of the SHG was stretched to 200 fs and the OPA

was pumped with 50 μJ, the Conversion efficiency calculated from the peak power ratios, compensated for the difference in energy is 10.2 %. The peak power was calculated by taking the ratio of pulse power (1 μJ) and dividing it by the duty cycle of the pulse at the transform limit (30 fs) and dividing that result by the peak power to duty cycle ratio of the SHG Pump (50 μJ for 200 fs). Frequency compensation was added by taking the ratio of frequencies of the OPA light (20000 cm^{-1}) and the SHG light (25839 cm^{-1}). The highest reported conversion efficiency is 13%. The output from the mixing crystal is lightly collimated with a 50 mm FL PCX lens. Following the pulse compression with the appropriate distance separation between the prisms as described by the previous subsection under Pulse Compression, the OPAs emerge with a power of 500 nJ. At this point the beam, depending on the bandwidth, may have a very non symmetric mode with a large divergence. A fundamental tradeoff in optical parametric amplification is the spatial mode to bandwidth quality. If the bandwidth is significantly large, the spatial mode will suffer in quality, and visa versa. To correct the spatial profile and the divergence, the beams are passed through a telescope with a spatial filter. A lens focuses the beam with an f=100 mm PCX lens into a 50 μm spatial filter. The beam waist for a 2 mm beam focused over 100 mm is approximately 30 μ. The spatial filter is moved away from the beam waist towards the focusing lens until the filter begins to cut the spatial profile of the beam. When the incident power is cut to 50 % (250 nJ) of the input power, an Airy diagram emerges around the beam, complete with Fresnel rings. At the center lies a perfect TEM00 Gaussian beam, ideal for Four Wave mixing measurements.

The beams are passed through another set of delay stages and forwarded to collinearly to a 150 mm Lens that focuses the beams for overlap in a piece of glass in a BOXCAR geometry. Each arm has a beam splitter by the delay stage to split the beam to be sent to an adjacent delay stage for tr-SD characterization for each independent beam. The beams not being characterized are blocked and tr-SD can be measured, as described in the previous section. The spectrally resolved self diffractions measurements for each of the three OPAs are depicted in Figure 3.9

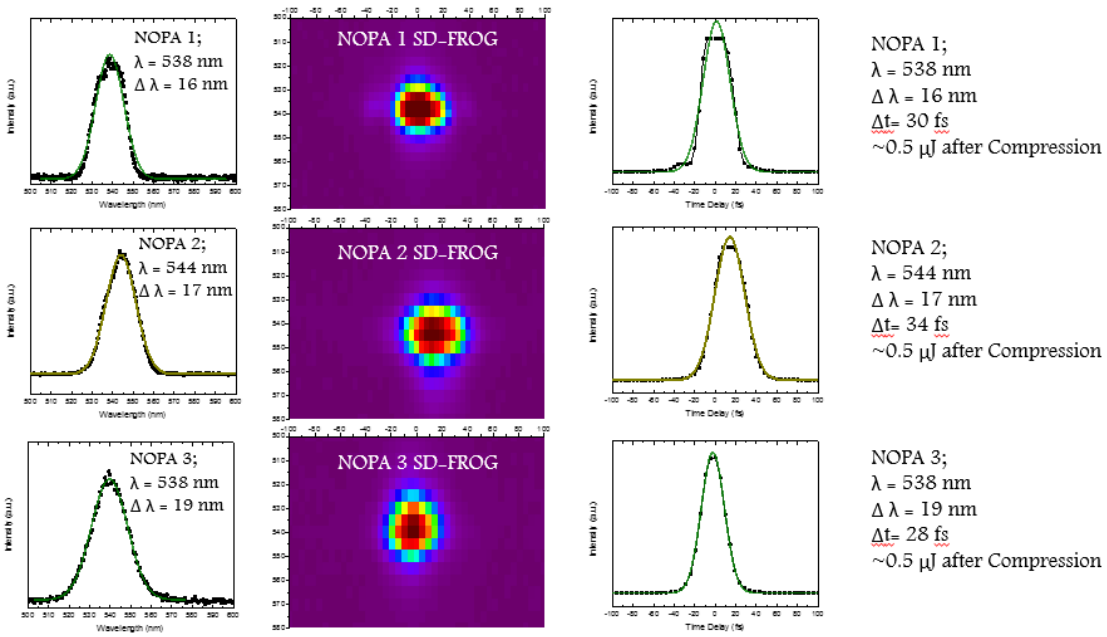

Figure 3.9: Time Resolved Spectral profiles of the three optical parametric amplifiers as characterized by tr-SD. Each NOPA has a clean Gaussian temporal and spectral profile with a transform limited pulsewidth.

All three pulses are 30 fs and transform limited. After each pulse is characterized, the three are mixed in glass and the delays and spatial overlap of all three OPAs is optimized to create the maximum degree over nonlinear mixing as depicted in Figures 3.10 and 3.11

In the case where the OPAs are nearly degenerate (Figure 3.10) the higher degree of nonlinear signals generated is due to the wavevector matching of the degenerate colors being significantly better than in the non-degenerate case (Figure 3.11). One of the signals corresponding to Four Wave Mixing where all of the beams act only once in the generation of a signal was measured in time with the time dependent spectrum appearing in Figure 3.12.

The instrument response function, or the three beam correlation function, as measured by scanning one of the OPAs in time, reveals a transform limited Gaussian shape in time and spectrum with a pulse width of 35 fs. Effectively, this means that this system is capable of initiating and clocking molecular processes with a resolution of 35 fs.

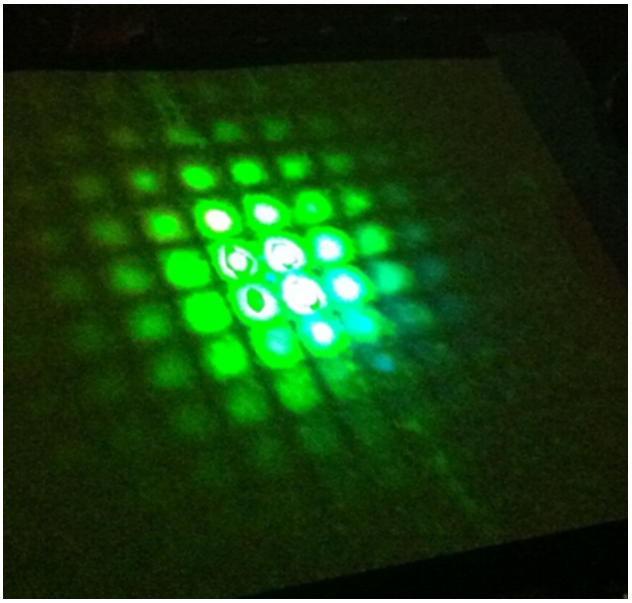

Figure 3.10: The diffraction pattern generated when all three NOPAs are mixed via BOXCAR geometry in space and time on a thin piece of glass. Presence of higher order diffractions depict the relative healthiness of the temporal and spatial profiles of each pulse. The more observed orders the better the spatial and temporal profiles of pulses.

Figure 3.11: The diffraction pattern generated when all three NOPAs are mixed via BOXCAR geometry in space and time on a thin piece of glass. Presence of higher order diffractions depict the relative healthiness of the temporal and spatial profiles of each pulse. The more observed orders the better the spatial and temporal profiles of pulses. There are less diffractive orders than in the previous Figure because of the lower degree of overlap between the pulses due to different colors having a smaller coherence time as opposed to two degenerate colors.

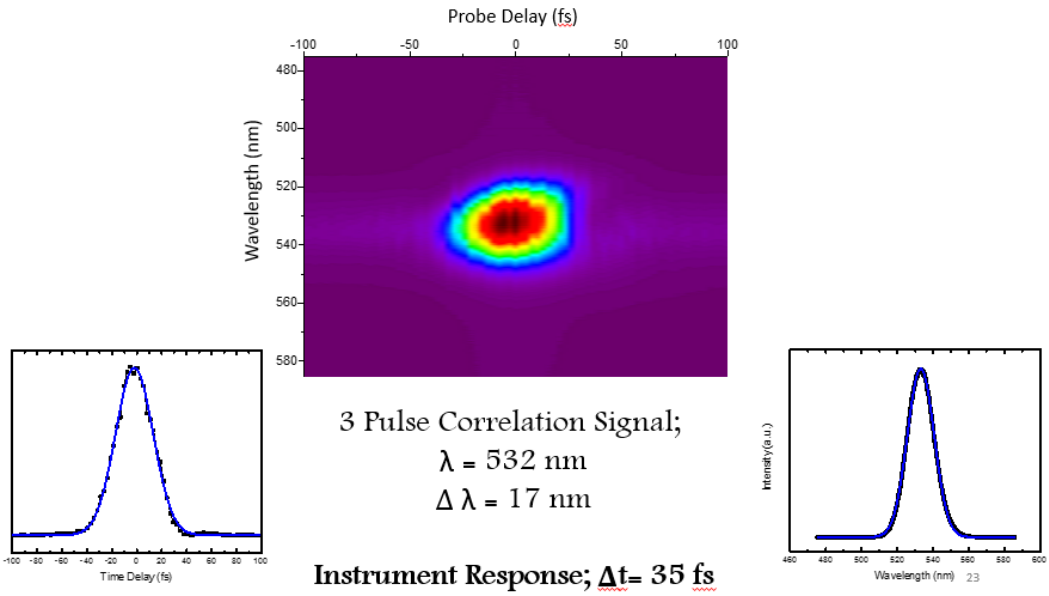

Figure 3.12: A three pulse correlation function used to characterize the temporal resolution of a four color four wave mixing experiment. The signal has a near transform limited Gaussian temporal profile, with a 35 fs temporal resolution to clock molecular dynamics.

3.3 Conclusion

The system was built to target any feasible four wave mixing measurement in the visible light spectrum, with the adaptation to make lower or higher energy pulses than readily accessible by a cacophony of Sum Frequency or Difference frequency generation to reach the desired pump or probe wavelength. However when in pursuit of the single molecule signal, a 1 kHz repetition rate can only yield a maximum of 1000 signal photons as one molecule can only emit one signal photon per pulse. Thus a higher repetition rate system is prescribed to study the fate of a coherence at the single molecule limit.

Chapter 4

The Single Molecule Coherence

We have succeeded in the first demonstration of time resolved coherent anti-Stokes Raman Scattering on single molecules through measurements carried out on molecules attached to gold nanosphere pairs which act as plasmonic nano-dumbell antennae. The tr-SECARS traces provide unique signatures of coherent evolution in discrete ensembles. The signals are characterized by phase and amplitude noise, which can be cast in terms of amplitude probability distribution functions (PDF), which allow rigorous distinction between single, few, and many molecule coherences. The experimental system for carrying out tr-SECARS and the analysis of the results in terms of PDFs are presented in this chapter. The analysis makes it clear that we have, for the first time, observed the coherent vibrational motion of a single molecule. Though the 80 MHz measurements were conducted with two colors, an extension of the experimental system at 250 kHz is explained, where three colors are used to assure the background free nature of the experiment.

4.1 Experimental Setup

Though the 1 kHz system previously described is optimum in every way for execution of Four Wave Mixing measurements, its repetition rate limits its application in the realm of time resolved single molecule spectroscopy. The following describes an idealized molecular system for measuring the single molecule vibrational coherence, measured by an 80 MHz Optical Parametric Oscillator.

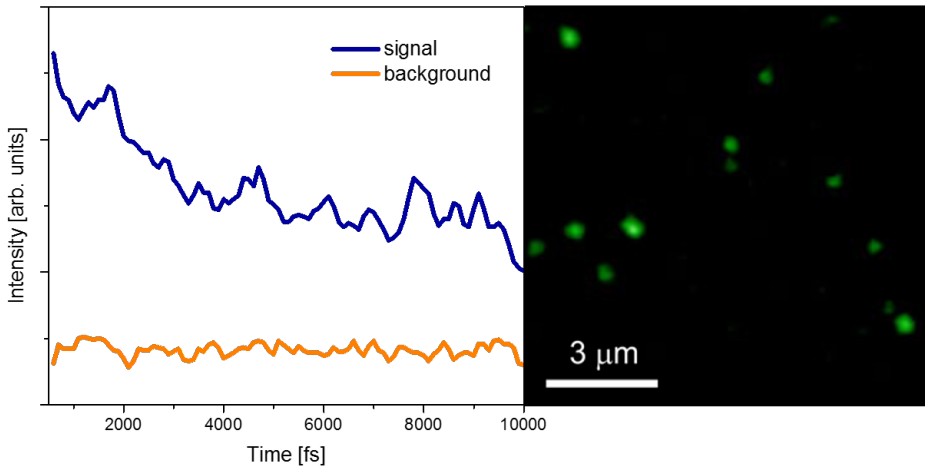

Figure 4.1: Time trajectories are taken from structures confirmed by SEM and Raman to be SERS-active dumbbell structures (green dots in CARS imaging data on the right) show time dependent oscillations, whereas the dark region (silicon nitride membrane), shows no modulation as a function of time.

4.1.1 80MHz tr-CARS Microscope

The time resolved system is pumped by a commercial femtosecond titanium sapphire laser (Spectra Physics Mai Tai). The output is frequency doubled to pump a tunable optical parametric oscillator (Radiantis Inspire OPO) tuned to be offset from the fundamental frequency by $1627 cm^{-1}$. The OPO output (714 nm) along with the residual fundamental are

compressed in time with a double pass prism compressor to achieve transform limited pulses. The OPO output split into two arms, one to be incident in time with the residual 809 nm and create the vibrational superposition, and another on a digitally controlled delay to probe the vibrational coherence created by earlier pulses. The three arms are overlapped collinearly and directed to a commercial microscope (Olympus IX-73) equipped with a Fluoview (FV1000) imaging system. The beams are focused into the sample by a 60x oil immersion objective with a numerical aperture of 1.42. The spot size of the beam is diffraction limited to 400 nm at the focus. The back scattered anti-Stokes photons are filtered out of the path by a dichroic mirror and collected with a monochromator CCD or photomultiplier tube (PMT). The forward scattered signal is also filtered and collected by a PMT. The Fluoview system can raster the beam to create an image of the sample in typically a 125 μm by 125 μm image with variable resolution and integration time per pixel. The luxury of having mirrors capable of rastering in the X and Y plane of the sample allow us to image an entire 100 μm x 100 μm grid, while the photomultiplier tubes record an intensity to each corresponding X and Y value. The gold nanoparticles are imaged using electronic CARS response of the surface plasmon modes[198, 199] shown in Figure 4.1 on the right. The time trace corresponding a gold nanosphere (dimer) structure show oscillations, while the dark regions of the image, consisting of the 20 nm silicon nitride membrane, shows a constant level throughout all the time traces, with a small amplitude noise arising from the PMT pulse height distribution. Samples are either zoomed into and collected rastered over quickly with the signal detected by monochromator/CCD, or alternatively, the whole 100x100 micron grid can be imaged using the PMTs. Measurements are made at iterated time delays of the probe pulse and displayed in the following section.

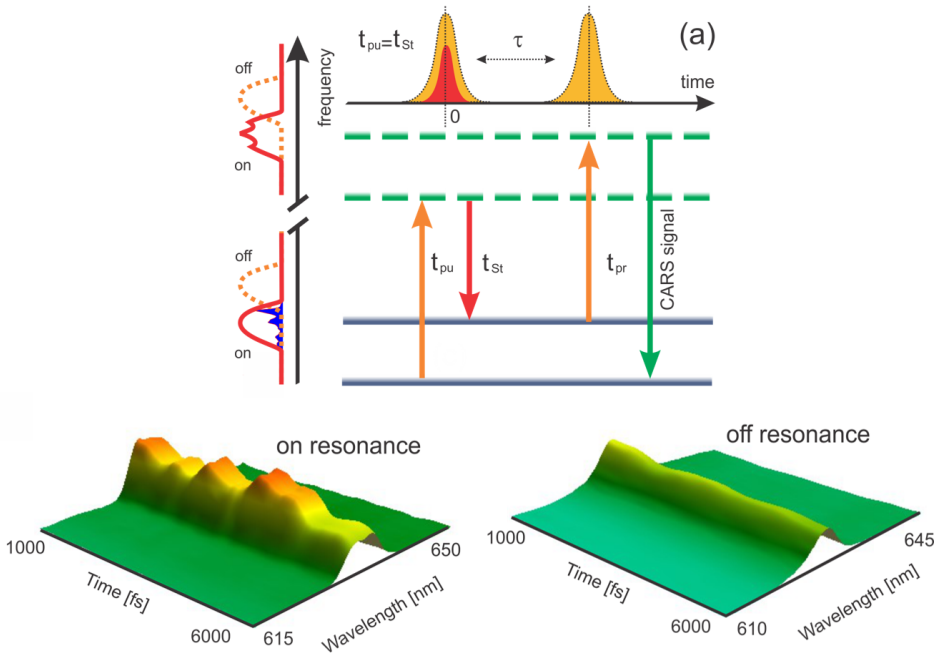

Figure 4.2: When the pump and Stokes pulse spectral convolution is tuned to overlap with the vibrational eigenstates (on resonance) modulations proportional to the difference frequencies of vibrational eigenstates are observed, whereas if the convolution does not overlap with the eigenstates (off resonance) no modulation activity is observed

4.1.2 Sample Characterization

The single molecule samples are purchased from Cabot Security Materials. The structure consists of two gold spheres, roughly 90-100 nm in diameter, immersed in trans-bipyridyl ethylene. The entire system is enclosed in a 70-80 nm thick Silicon oxide shell. The shell is used to better ensure structural integrity of the system, and as a heatsink into which peak power excitation can dissipate. The sample is diluted to the desired concentration, and then spin coated or drop cast onto a silicon nitride TEM grid (Ted Pella). The silicon nitride is roughly 20 nm thick to ensure minimum scattering background. The spin coated sample is then taken to the SEM for coarse characterization of the available candidate structures for the experiment. Though SEM only offers a rough picture, ideal dumbbell structures can be identified and later probed. The selected candidates are then taken to a high numerical

aperture Raman microscope to be characterized for Raman activity of the trans-bipyridyl ethylene. A few molecules with significantly apparent Raman spectra per grid are then tagged and taken to the time resolved system.

4.1.3 Testing the Validity of the Data

Three measures were taken to ensure that the signal we collect is in fact tr-CARS. Firstly, the preparatory bandwidth was tuned to a region with no peaks in the Raman spectrum. Assuming the signal is CARS, if the bandwidth overlaps with vibrational bands, the time resolved measurement yields the difference frequency of all prepared bands oscillating in time. So if no bands are prepared within the convolution, no oscillations should be seen in the time delay. Such is the case in Figure 4.2. Here we see oscillations resembling 1 ps periods, analogous to the separation between the mean vibrational frequency in the Raman spectrum of the dimer. In the non-resonant case, a flat background is seen at all delays. The constant background arises from the time zero response of the gold nanoparticles. The level is constant across all delays because while the response of the gold is not long lived, due to the degenerate spectrum of the pump and probe beams, the pump beam may act twice at time zero and generate an anti-Stokes photon before the system even evolves. Future experiments will include three independent colors so as to avoid the problem of signal contamination making the measurement truly background free.

Another test used to determine the validity of the CARS experiment is comparison of the negative versus positive time traces. Measurements at negative time probe the coherence before the coherence is prepared.[200] Given that there is no coherence to interrogate, there should be no oscillations or amplitude related to the vibrations evolving in time. In Figure 4.3 low noise modulations are shown before time zero, with high amplitude oscillations resembling a 1 ps period, establishing that the prepared vibrational coherence is indeed

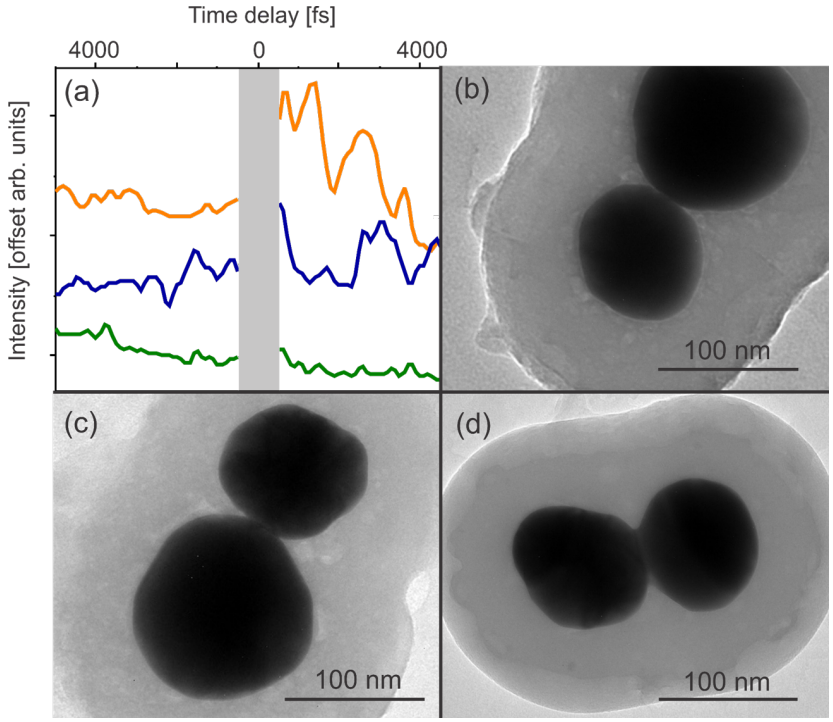

Figure 4.3: Time traces of individual dumbbell structures that are SERS active (TEM images and after irradiation in (b),(c),(d)) show little to no modulation at negative time (before superposition is prepared), and exhibit modulation activity with a period of 1 ps after the superposition is prepared (orange and blue trace). SERS inactive structures show no modulation activity at negative and positive time (green trace)

being probed, atop a constant gold time zero response.

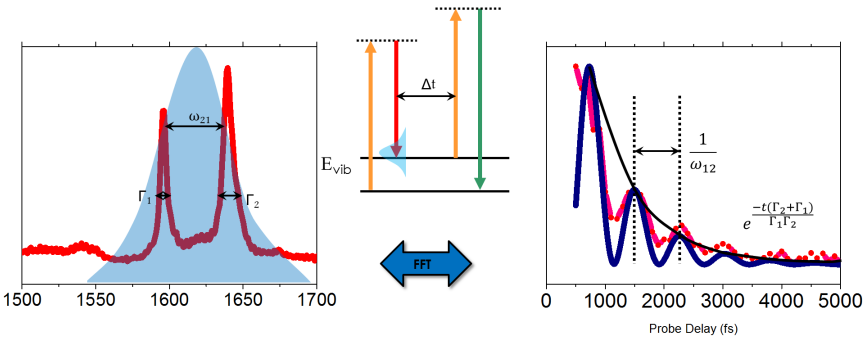

Figure 4.4: (Left) an ensemble Raman spectrum (red) of trans-bipyridyl ethylene with a two pulse(Pump+Stokes beams) spectral convolution (blue). (middle) Jablonski representation of tr-CARS, (right) a tr-CARS trajectory of bulk trans-bipyridyl ethylene (red) with an FFT of the bulk Raman spectrum (blue) shown on the left.

4.2 Calculated Signal Fluence

For the time traces shown in the analysis, the modulation depth of the fluctuating time traces is 10 counts. These counts from the Fluoview instrument are converted back into the incident current on the PMT which can be trivially converted into the photon flux per second and give a reasonable estimation of how many photons of signal are incident on the detector per pulse.

The Analog to Digital converter for the data visualization is 12 bit, giving a dynamic range of 4096 counts. 3.3 V of signal onto the ADC corresponds to 4096 counts meaning that 10 counts would come from 8mV of signal. These 8mV are converted from current by a 75 Ohm resistor. Following V=IR, 8mV corresponds to 107 μA of current. This current arrives at the resistor from a transimpedence amplifier that amplifies the current from a PMT by a factor of 100, meaning that the current at the anode of the PMT is 1.07μA. The gain of the PMT at the used 1200V of High Voltage is $1.5 * 10^7$ A/W of photons incident onto the dynodes of the PMT. Taking into account that the Quantum Efficiency of the PMT is 11%, The photon flux on the PMT is 0.65 fW. The energy of the anti-Stokes photon collected at 640 nm is $3.1 * 10^{-19}$J, giving a photon flux of $2.09 * 10^6$ photons per second, This quantity, divided by the repetition rate of the laser means that for the experiment energy of 100μW per pulse, the flux of signal photons is 1 for every 38 incident pulses.

4.3 tr-CARS in the Single Molecule Limit

For the case of an ensemble, by extracting a vibration's central frequency and homogeneous linewidth, as well as the difference in vibrational frequencies prepared under a two-pulse convolution, the tr-CARS trace can be reconstructed via a Fourier transform. The time trace consists of oscillations, with frequencies equal to the difference frequencies of the states

prepared. The signal will contain beats with a modulation depth determined by the amplitudes a_i (see Eq. (2.12)). of the vibrations from the Raman spectrum. The oscillations will decay as a function of the inverse linewidth of the vibrational bands. In addition to the dissipation of the hot vibrational state, the decay of the oscillation depth will be accelerated by pure dephasing, or the impact of collective oscillations of many molecules simultaneously, each with its own relative phase. Two C=C stretching modes belonging to the pyridine ring breathing mode and the ethylinic stretch of BPE [201] centered at 1600 cm^{-1} are the focus of the tr-SECARS measurement. The ensemble trans-bipyridyl ethylene Raman spectrum shows 2 homogeneous vibrations within the two pulse convolution window with a separation of 33 cm^{-1} and a width of 5 cm^{-1}. A Fourier transform of the ensemble Raman spectrum agrees perfectly with the experimental trace, which decays over the course of a few ps (Figure 4.4). Thus all the information contained in the tr-CARS measurement of an ensemble can be obtained by performing a more trivial Raman measurement.[202] However, the reasoning above cannot explain the tr-CARS trace in the case of a single molecule.

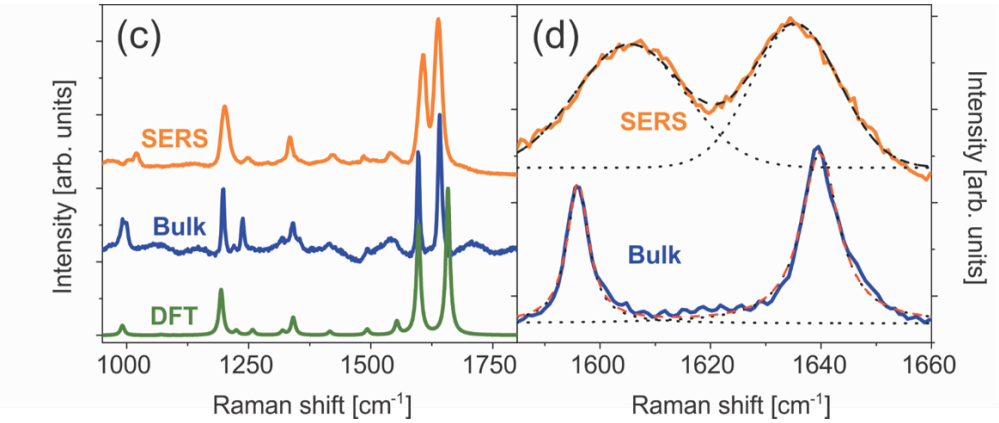

Figure 4.5: BPE in a SERS active dumbbell(orange), in bulk (blue) and calculated (green). (right) Close up of the vibrations(orange from SERS active structure, blue from Bulk BPE) that were subsequently probed with tr-CARS

The SERS spectrum in Figure 4.5 of the single nanoparticle shows vibrational bands approximately at the same frequencies as the ensemble trans-bipyridyl ethylene spectrum. The gold

nanoballs that encase a molecule (or a few) in their junction contain peaks with a Gaussian lineshape three times larger in width than the ensemble Raman peaks.[203] The inhomogeneous lineshape is indicative of spectral diffusion that is too fast to be observed in the time frame necessary to obtain significant signal to noise in the spectrum. When the spectra are collected sequentially with a lower integration time, benign traces of the spectral diffusion and amplitude modulation can be observed in Figure 2.6.

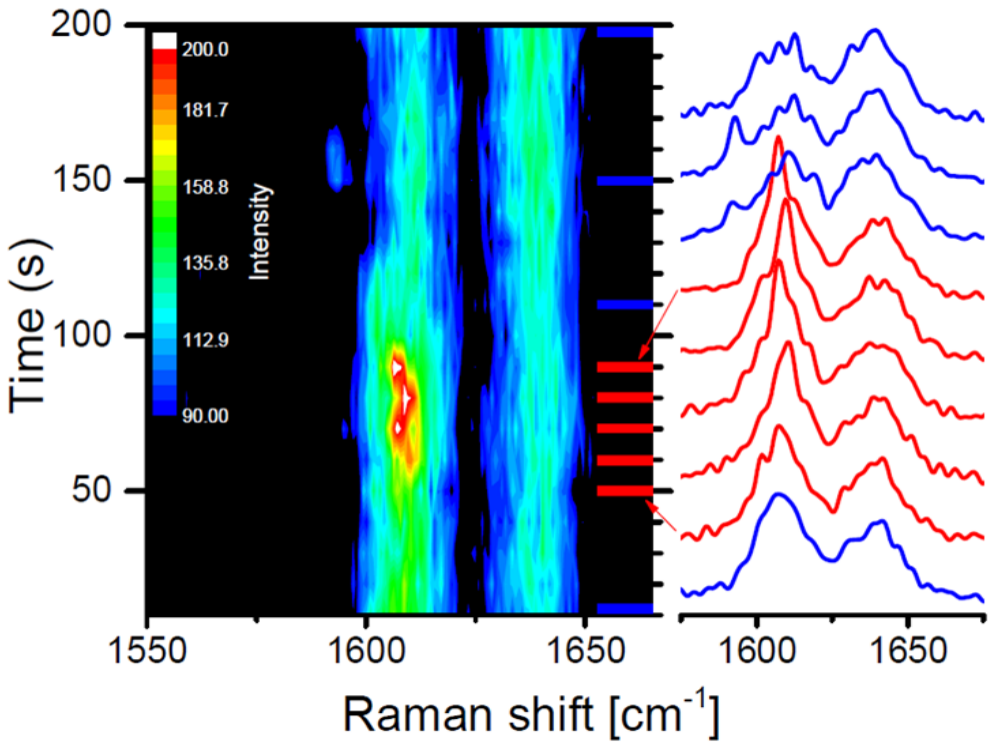

Figure 4.6: Raman spectra of a SERS-active dumbbell structure acquired sequentially in 10 s periods for 200s, with select spectra at various points in time (right). Modulations in peak width and intensity and mean frequency can be observed occurring on the acquisition time scale.

This behavior is the hallmark of a few, or possibly a single molecule. As a consequence, when performing a tr-CARS measurement, the vibrations prepared and subsequently probed during one pulse, may diffuse slightly in the preparation and probing of the next pulse. If the single molecule time trajectory could be extracted from the Raman spectrum, it would dictate that the single molecule time trace would decay much faster than the ensemble

due to the 15 cm^{-1} linewidth of the vibrations, making the tr-CARS method redundant. Furthermore, distinguishing a single molecule from a few molecules in the frequency domain (Raman) is not trivial as both exhibit inhomogeneous vibrational bands with indiscernible characteristics. Only gold nanoballs that showed a Raman spectrum with features that resembled single or few molecule behavior were used in the tr-CARS measurements.

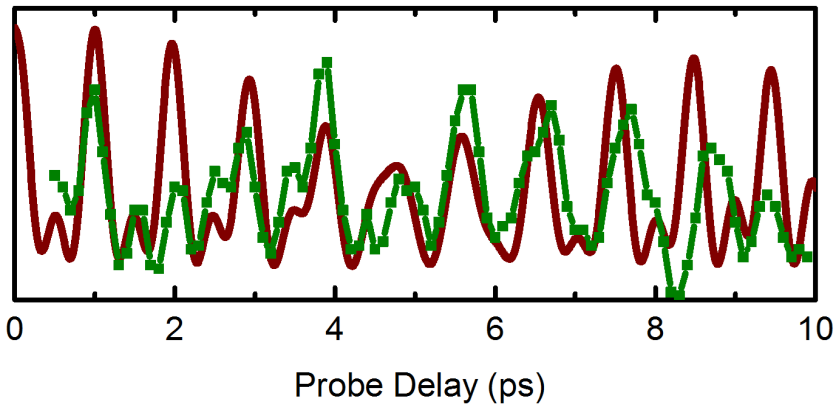

Figure 4.7: tr-CARS measurement on a SERS active dumbbell (green) shows distinct quantum beats, and can be simulated with good fidelity via FFT of four discretely defined vibrational eigenstates (red).

All tr-CARS measurements showed a signal that does not decay within the time prescribed by the width of the SERS-active gold nanoball structures. One particular trace is depicted in Figure 4.7 in green. The signal was fit (red trace) with four vibrational lines having a width of 0.1 cm^{-1}. The slow beat was reproduced by having two vibrations, which appear briefly in the 1580 cm^{-1} region in the meandering Raman trajectory in Figure 4.6. The faster feature was produced by having one of these transient lines (from the meandering slide) beating against one of the main bands present in the ensemble and the dimer spectrum 1647 cm^{-1}. The 1 ps beat feature was reproduced by the two main vibrations 33 cm^{-1} apart. While the main features of the trace were reproduced, the SERS spectra show that in reality, the vibrations are much wider than the simulation prescribes.

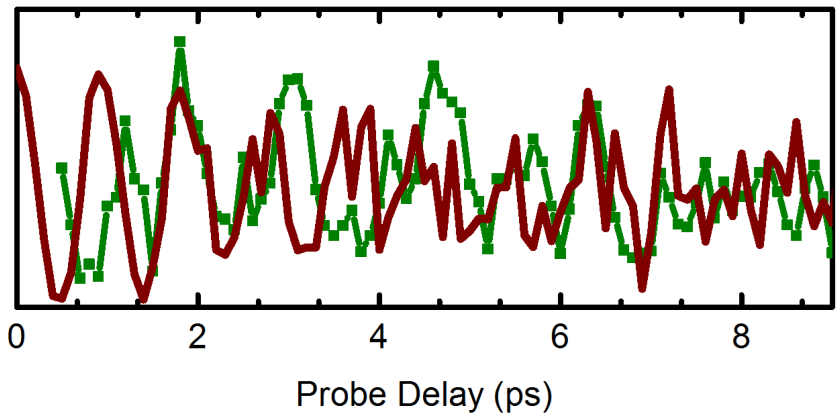

Figure 4.8: tr-CARS measurement on a SERS active structure (green) shows distinct quantum beats at early times, which recede into phase noise at later delay times. The fit (red), is one stochastic manifestation of phase noise that arises from a randomized shift δ from Eq. (4.2)

A more typical time trace is depicted in Figure 4.8 (green trace), where the 1 ps oscillation emerges at early delay times, with some noise, and eventually recedes to a smaller amplitude modulation around approximately $\frac{1}{2}$ the maximum amplitude at the time of preparation. This signal cannot be fit with the previous static narrow vibrational width model. However, if a small shift is added to the mean vibrational frequency to account for the spectral diffusion observed in the SERS Spectra, the noisy features, and the decay of the oscillation to noise can be reproduced. This shift from the mean vibrational frequency, is selected randomly upon preparation, from within a normal distribution that matches the shape of the Gaussian lineshapes observed in the SERS spectra of gold nanoballs.

Here we depict the general model for the simulation used to replicate the experimental time traces;

$$S(t) \propto \frac{1}{M}\sum_{m=1}^{M}|\frac{1}{NV}\sum_{n=1}^{N}\sum_{v=1}^{V}a_{n,v}e^{-\imath\omega_{n,v}t}|^2 \tag{4.1}$$

where S is the signal over time which results from summing over N, the number of photons collected, M, the number of molecules, and V the vibrational eigenstates. For the time being, the number of photons collected is set to 1 for simplicity. In the case of one molecule and two vibrations, the above equation yields the trivial example depicted in the CARS theory section; a summation of a constant with a difference frequency oscillation. In order to simulate a time trajectory similar to the experimental traces, the spectral diffusion from the mean vibrational frequencies must be accounted for. A shift, $\delta_{n,v,m}$, of the bands is included, and can be random within a predefined normal distribution described earlier;

$$S(t) \propto \frac{1}{M}\sum_{m=1}^{M}|\frac{1}{NV}\sum_{n=1}^{N}\sum_{v=1}^{V}a_v e^{-\imath(\overline{\omega}_{v,n}+\delta_{m,v,n})t}|^2 \tag{4.2}$$

Upon further simplification;

$$\begin{aligned} S(t) \propto \quad & \frac{1}{N}\sum_{n=1}^{N}|\frac{1}{V}\sum_{v}^{V}a_i e^{-\imath(\omega_v+\delta_{v,n})t}|^2 \\ & = \frac{1}{4N}\sum_{n=1}^{N}|a_1|^2+|a_2|^2+2a_1a_2cos[(\omega_{21}+\delta_2-\delta_1)t] \\ & = \frac{1}{4N}\sum_{n=1}^{N}|a_1|^2+|a_2|^2+2a_1a_2cos[(\omega_{21}+\Delta)t] \end{aligned}$$

Δ is introduced to highlight the covariance of the frequencies of the two states that are being measured.

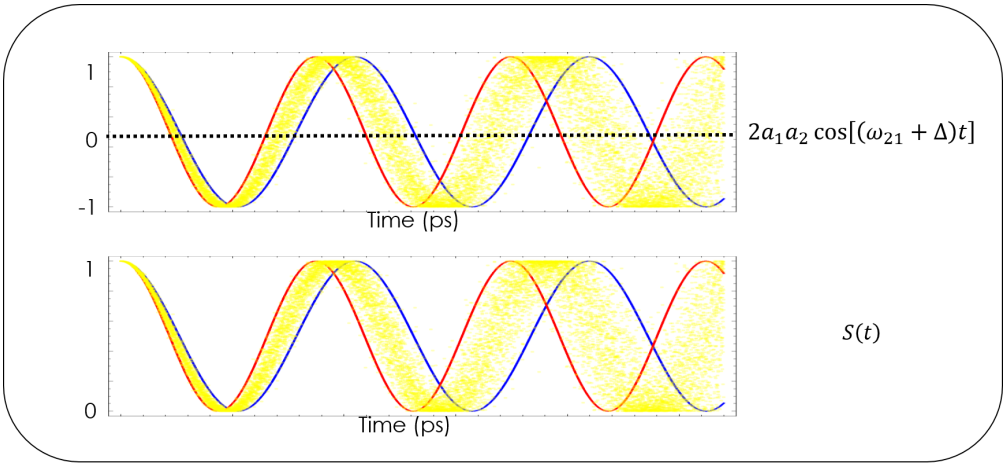

Figure 4.9: Simulation of the $2a_1a_2cos[(\omega_{21} + \Delta)t]$ (top) and the $S(t)$ (bottom) from Eq. (4.2) evolving in time. The red line represents the fastest beat frequency while the blue line represents the slowest. The yellow region in between indicates all possible values that can be measured in one stochastic trajectory.

To better illustrate the behavior of the covariance, an example with two excited vibrations is considered; a case with the smallest difference frequency and a case with the largest difference frequency within the normal distributions of the vibrational bands is illustrated in Figure 4.9. The two cases provide an outline for all possible time traces that can be obtained when performing a tr-CARS measurement on this specific molecule. It is apparent that as the time between the preparation and probing increases, the possible intensities that can be obtained as a function of the "random" shifts of the vibrational frequencies increases. As the phase angle between the faster and slower oscillations reaches π all intensities in the oscillation depth are possible but occur within a normal distribution. Moreover, as the time is increased further, the phase angle will wrap 2π and the distribution, or the likeliness of measuring any phase becomes equal.

If a one molecule, two vibration system subject to phase shifts is prepared, and measured once only per delay (one photon gathered), the cosine term will yield the full range of -1 to 1 when $\tau >> 0$ and when incident on a photodetector (squared) will yield one value in the range of 0 to 1. The average of many measurements at later times where each measurement

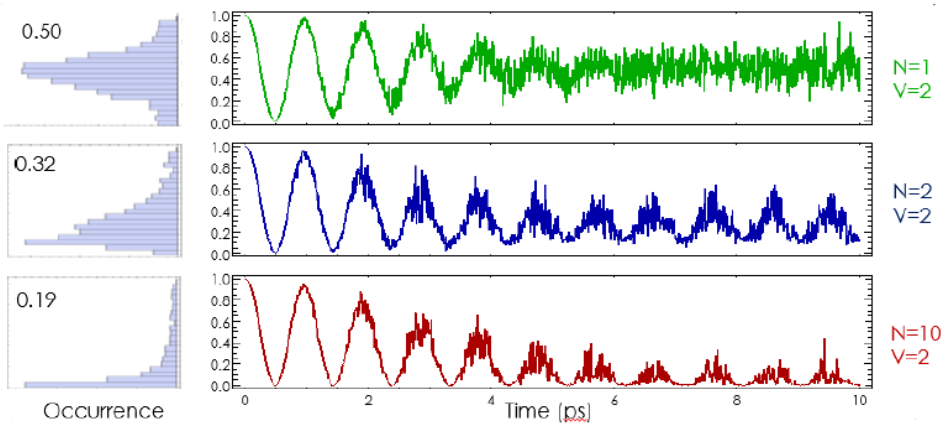

Figure 4.10: tr-CARS trajectories simulated for one (green), two (blue), and ten (red), molecule system(Eq. (4.2)), each prepared with one difference frequency and measured with 10 photons per delay. As the number of molecules prepared is increased, the onset of pure dephasing becomes more evident. On the left are probability distribution functions (PDF) for each time trace. The shape and the first two moments of these distributions is characteristic of the number of molecules prepared.

could be any random value from 0 to 1 will be 1/2. If two molecules with two vibrations are prepared, having the sum of two cosine terms squared will yield a value of 1/4 when averaged over many measurements at large delay times. The one, two, and 10 molecule superposition is depicted in Figure 4.10. As the number of molecules prepared increases, so does the number of cosine terms in the molecular response function. The expectation value of many cosine terms with random phases is 0. Upon squaring the sum of many cosines the measured phase at later times is also expected to be 0. Thus, if many measurements are averaged, a mean value characteristic of the number of molecules and vibrations prepared can be obtained. The value is proportional to $\frac{1}{NV}$. For example, a single molecule, prepared with 2 vibrations, averaged over many measurements will converge to $\frac{1}{2}$ at a delay when the phase angle spans a uniform distribution. Note that the opposite case, where 1 vibration is prepared on two molecules is not possible, as the coherence of one vibration will not yield a time dependent oscillation. A single molecule tr-CARS trajectory does not decay by pure dephasing, but instead recedes into phase noise, which carries a characteristic mean.

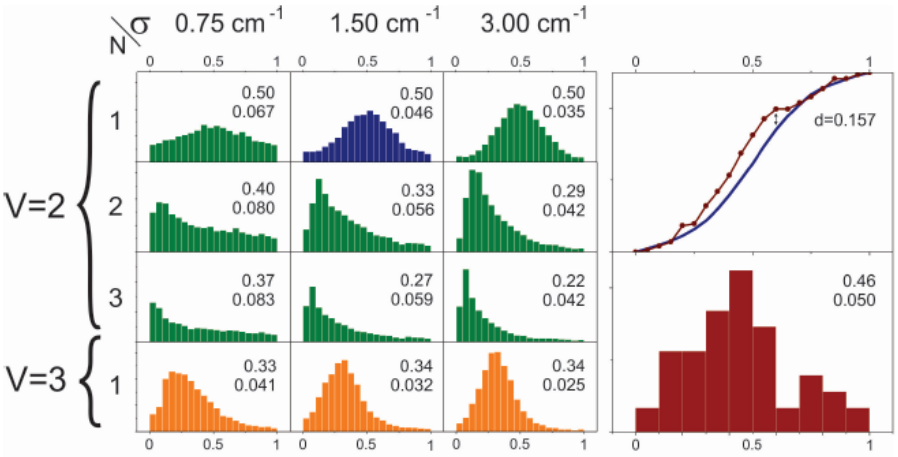

Figure 4.11: Probability distribution functions (PDF) generated using Eq. (4.2) for different numbers of molecules (N), vibrational eigenstates (V) and variance of spectral fluctuations (δ) On the right (red) is the PDF for the tr-CARS trace shown in Figure 4.8. The experimental PDF, along with mean and variance, uniquely match their simulated counterparts containing the parameters N=1, V=2, and $\delta = 1.50\ cm^{-1}$. The experimental cumulative distribution function (CDF; red dots in the top right) and the theoretical CDF made from the PDF with blue bars are also indicated. The Kolmogorov-Smirnov(KS) test indicates a maximum distance of $d = 1.57$ between the theoretical and experimental CDFs. This d value translates into a 99% likelihood that the experimental data represents the evolution of a statistical two-state superposition on a single molecule.

The phase noise will manifest itself differently each time the simulation is computed or an experiment is performed. Therefore the fitting of the simulated phase noise to an experimental single molecule signal results in purely qualitative information. Amplitude histograms of the time traces can be made; and quantitative correlations extracted from the mean and variance of the histogram. These moments are characteristic to the number of photons collected, as well as the number of vibrational bands and the number of molecules prepared. If the number of photons collected from the system is large, then the variance of the histograms will be small. The mean can discern, most accurately between the single and many molecule case. The mean will approach 0 for the many molecule case, and converge to $\frac{1}{2}$ for the single molecule case(on a normalized scale of 0 to1). In general, for any number of N and V,

the signal will converge to $\propto \frac{1}{NV}$. Coupled with a high number of collected photons, this relationship will be more precise. As V is increased, it becomes hard to discern the "many" molecule case from the "many" vibrational eigenstate case. As a result, the histogram analysis can accurately discern a single molecule signal for an ideal two vibrational eigenstates contributing to the coherent phase correlation.

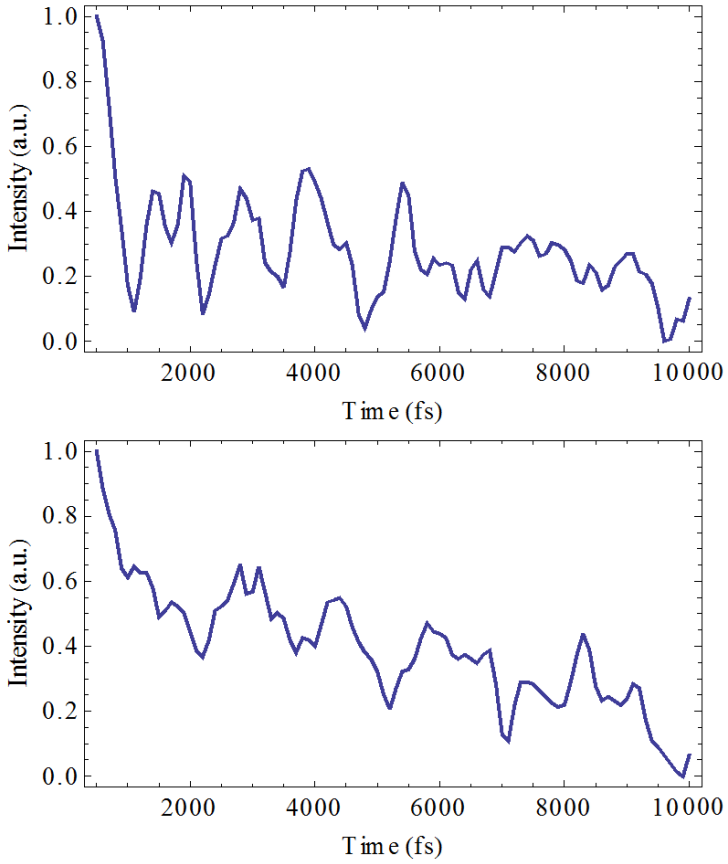

Figure 4.12: Two tr-CARS traces from other SERS active nanostructures. The top trace depicts distinct quantum beats at early times and recedes into phase noise albeit a small artifact at early time believed to be part of the three pulse correlation centered around $t = 0$ fs. The bottom trace shows signs of convergence to 0 as the probe delay is increased, indicating the preparation of more than one molecule.

Simulation histograms for $V = 2, 3$ and $N = 1, 2, 3$ have been made in Figure 4.11, having covariance values of .75 cm^{-1}, 1.5 cm^{-1}, and 3 cm^{-1}, alongside histograms of experimental

traces. The simulations from which the histograms have been generated, have been oversampled for a step size of 1 fs whereas the experimental traces were collected with 100 fs time steps. It is apparent that the experimental distribution matches closely to the histogram that was generated from one molecule with two vibrations and covariance of 1.50 cm^{-1}. Depicted in Figure 4.12 are two more time traces of the many that were collected. The first depicts a similar situation to the earlier experimental trace (Figure 4.8), albeit a small amplitude drop at early time. This feature could be an artifact of the interference between the pump and probe pulses around time zero. If those data points are omitted, the histogram also matches that of one molecule, two vibration model, with 1.5 cm^{-1} covariance. In the second case, there is an exponential decay and then the signal stays relatively flat, with ps features that appear to be the indication of two prepared vibrations 33 cm^{-1} apart. While the exponential decay is indicative of a large number of molecules within the interaction volume, the ensemble, as shown earlier, does not survive beyond a few picoseconds. Upon the loss of the ensemble coherence, the single molecule coherence persists.

The amplitude histograms can be made more accurate by averaging over a set of measurements on different dumbbells. We cannot add together the stochastic time trajectories, however, we can combine their histograms to improve statistical significance of the measurement set. Three trajectories were picked for each case of a single, few, and many (green, blue, and red PDFs in Figure 4.13). The sorting was done by the mean values of their respective PDFs. The PDFs corresponding to the green blue and red traces were combined to broaden the number of samples composing each respective summed PDF. The generated histograms can be transformed into cumulative distribution functions (CDF) for a more rigorous non-parametric analysis using the Kolmogorov-Smirnov(KS) test. This is done in order to compare the CDF of the simulation histograms to those that appear to be from single, few, and many molecules. The KS test uses a two sample comparison to provide correlation between two CDFs with the same number of elements using the distance between the two

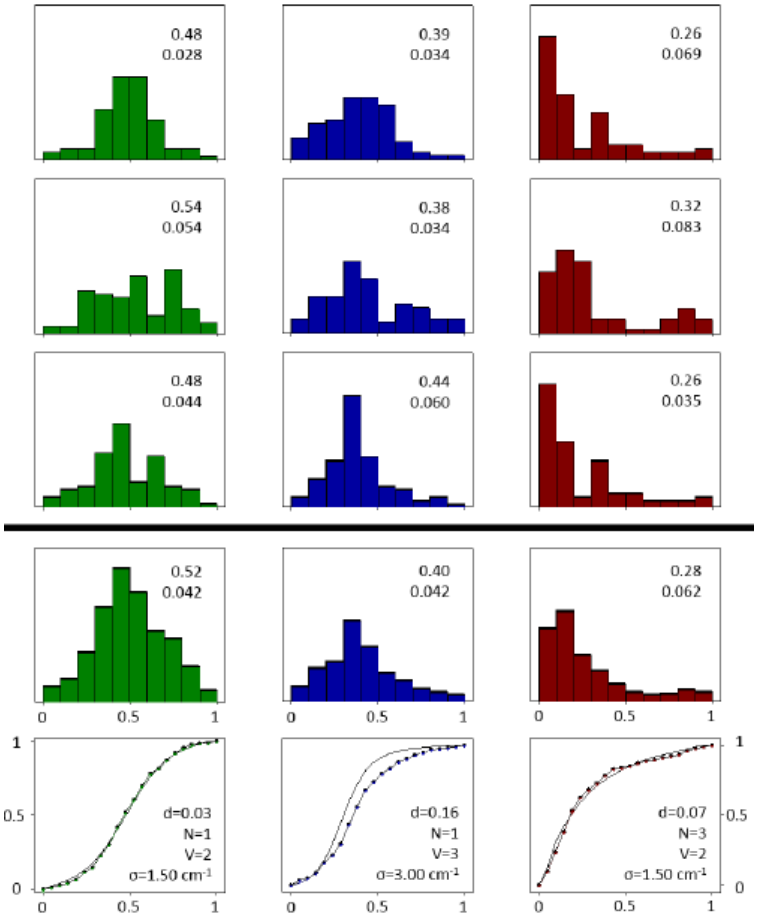

Figure 4.13: Probability distribution functions for tr-CARS traces obtained from nine different nanosphere structures. The mean and the variance of each distribution is also indicated. The PDFs are sorted by color based on their moments. The averaged PDFs appear in the fourth row, along with their CDFs in the fifth row. The CDFs are compared distribution functions generated from stochastic trajectories for the indicated number of molecules, vibrational eigenstates and their spectral covariance (N,V, and σ respectively). In all three cases, the measured distance d (Eq. (4.3)), is less than 0.162, indicating a 99% certainty of the assignments.

functions at any given element;

$$d = Max|F_i(x) - F_i'(x)| \tag{4.3}$$

where F_i and F_i' represent the experimental and simulated CDFs and i signifies the specific

element in the CDFs. The KS test gives 99 % confidence probability if d does not exceed a critical value of 0.162 for a sample consisting of 100 elements. From a comparison of simulated vs experimental CDFs with their largest d shown in the respective comparison in the Figure 4.13. It can be seen that for the single, few, and many molecule case, the simulation and the experimental data exhibit statistical certainty with respect to their assignment.

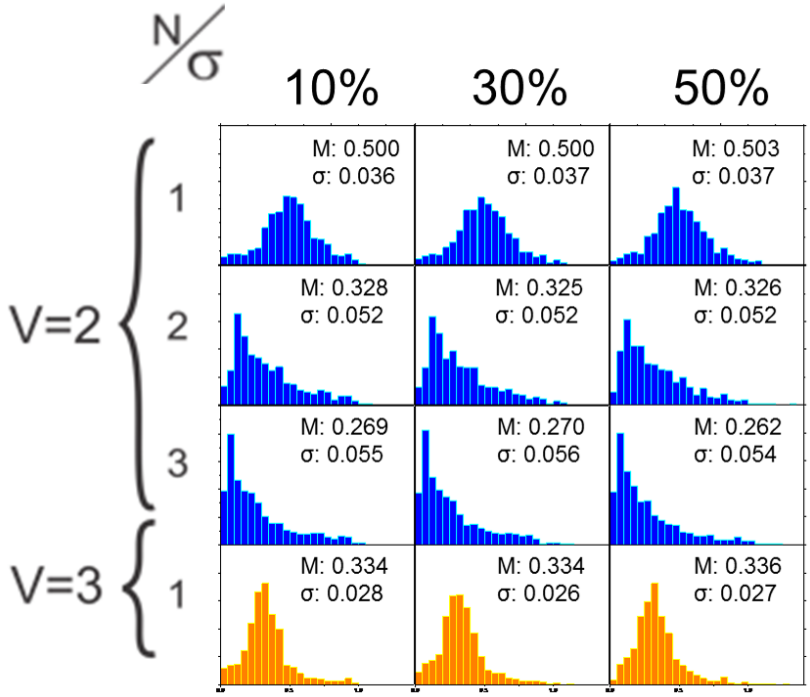

Figure 4.14: Amplitude noise (10, 30, and 50 % respectively) distributions generated for a various cases of molecules (N) and vibrations (V). With increasing amplitude noise, little to no change can be observed to the shape of the distribution, nor its first two moments as indicated in each row in the top right corner.

The histograms prove as an adequate characterization method for the phase noise on the vibrations prepared on a few molecules. Another source of noise that was not considered in the above analysis is amplitude noise. However, with the inclusion of amplitude noise from 10 % to the 50 % range. the shape of the distributions remains largely unchanged

(see Figure 4.14). In the time trace picture, when measuring the difference frequency, the amplitude noise manifests itself at the peaks of the oscillations, thereby spreading the high intensity counts of the histograms to values above the normalized range. But the counts on the lower intensity remain unchanged.

When the tr-SECARS is combined with the histogram analysis, the difference between a single molecule and the many molecule case becomes trivial to discern quantitatively using the KS test, and traces of single molecule dynamics can be singled out and identified with statistical certainty.

4.4 Extension of measurements to three colors via a 250kHz Microscope

The next step involves repeating these experiments in absence of the background noise generated by impulsive CARS at time zero by measuring the same system with an uniquely tunable probe pulse. For this undertaking, a 250kHz amplified laser system with two NOPA's already built will be remodified and used to further push the boundaries of Single Molecule Spectroscopy. (250kHz system)

4.4.1 250Khz Sequentially Pumped Optical Parametric Amplifiers

A previously built sequentially pumped two NOPA system was constructed, driven by a 250kHz Coherent RegA Chirped Pulse Amplifier. The amplifier emits 7 μJ pulses of 800nm light with a bandwidth capable of supporting 50fs pulses. This light was used to pump two individual WLC stages and a common SHG stage where the SHG light was used to pump one OPA and the leftover energy recycled to pump a second OPA. Including the fundamental output of the amplifier, this gives three colors for use in our experiments; one color locked

at 800nm with two tunable colors throughout the visible region. The schematic for such a system appears in Figure 4.15.

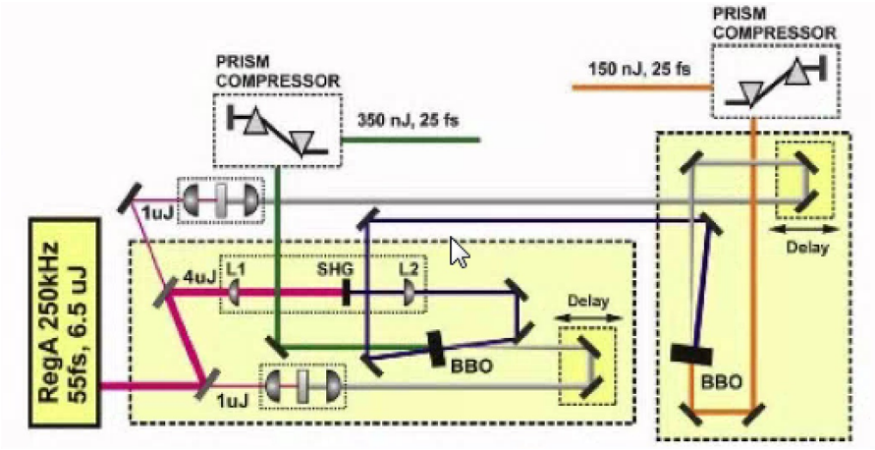

Figure 4.15: A schematic for two sequentially pumped NOPAs that utilize the pump amplifier output as a third color for Four Wave Mixing Spectroscopy.

The incoming P polarized light is sent through a periscope(not shown) to change the height of the beams and also to rotate the propagation direction by 90 degrees. In such a geometry the polarization of the beam is flipped and it becomes S polarized. The operating principles of the NOPAs are the same as covered in Chapter 3 except one key difference is that the pulse power of the amplifier is much lower on the 250kHz system than it is on the 1kHz system. However, NOPA operation is still very much possible in this regime, while the repetition rate allows an experimental capability that will give rise to 250x more signal photons than the previously described 1kHz system. The output form the periscope is split 90/10, with 10% used to pump a WLC from sapphire. See the instructions from Chapter 3 for a more rigorous procedure as to how this can be done efficiently. the 90% arm is split once again by a 90/10 beamsplitter with 10% going to drive another WLC stage for the second NOPA. The remaining 81% is sent focused over 400mm by a PCX lens through a 5x5x0.3 mm type I BBO crystal cut at 29.2 degrees θ and 0 degrees ϕ. The SHG and remaining fundamental is collimated by a f=200 mm PCX lens and the SHG is separated from the fundamental via a dichroic mirror selected to reflect the SHG at 400 nm and pass the fundamental 800 nm light

for use in experiments (not pictured). The SHG is then focused (by adjusting the earlier mentioned f=200 mm PCX lens away from the BBO crystal) into the first type II 5x5x2 mm BBO crystal cut at $\theta = 32$ degrees, ϕ=0 degrees. Following the instructions outlined for NOPA generation in Chapter 2, the WLC generated with the first 10% arm and passed through a delay stage, is amplified to give 708 nm light. 708 nm is chosen in conjunction with the 800 nm output of the amplifier, to create the necessary 1600 $cm^{-}1$ vibrational superposition on the sample. The leftover SHG light is recycled and used to pump the second OPA at another identical BBO crystal using the second WLC stage as the seed. The color here was chosen to be 615 nm. When the second NOPA is used as the probe, the measured anti-Stokes color comes out at 565 nm, whereas the previously used degenerate experiment would generate an impulsive CARS signal with the same frequency as the time delayed trace of interest, the impulsive CARS here is generated at 640 nm (2x 708nm - 800nm) far away from the time delayed signal that is sought for measurement. Both OPAs were sent to prism compressors with a distance between the prisms chosen for experiments in the bulk, i.e. the GVD compensation was for 2-3 PCX lenses maximum to achieve transform limited pulses at the sample position (not shown). In an effort to get experiments underway, the microscope from the previous experiments, including the FLUOVIEW system was attached to the output of these 3 colors, and experiments ensued. The bandwidths of the generated NOPAs and the fundamental is depicted in Figure 4.16

The bandwidths of the NOPAs and fundamental show a capability to be $\Delta t < 50$ fs at the transform limit when properly compressed. The choice of colors would give rise to an anti-Stokes signal at 565 nm. The spectral structure on the 800 nm pulse is due to the pulse originally being used to generate SHG to pump the OPAs and will perhaps yield some features in the time resolved experiments.

The first experimental traces using this system are depicted in Figure 4.17. Because all three beams are collinear in space, any of the three beams can serve as the Pump and Probe

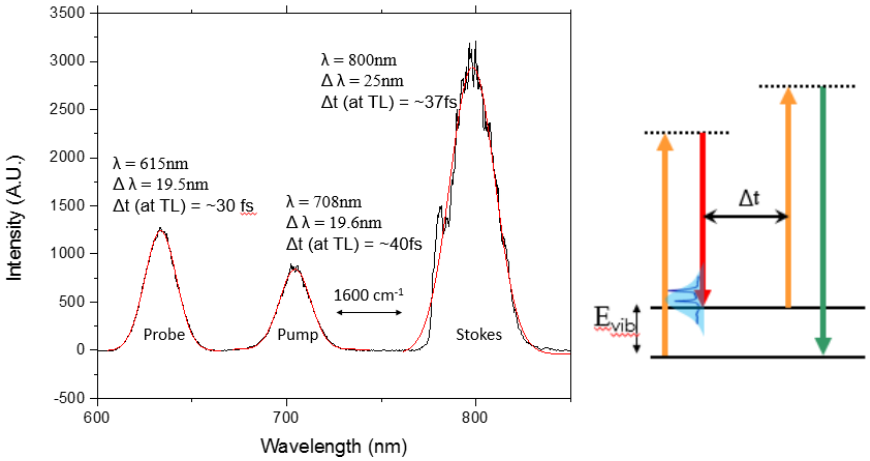

Figure 4.16: The two NOPAs were tuned to 708nm and 615nm with the amplifier output at 800 nm. When 708 nm and 800 nm are used to prepare a vibrational superposition at 1600 cm^{-1}, and a time delayed probe pulse at 615 nm produces a molecular response at the anti-Stokes wavelength; 565 nm.

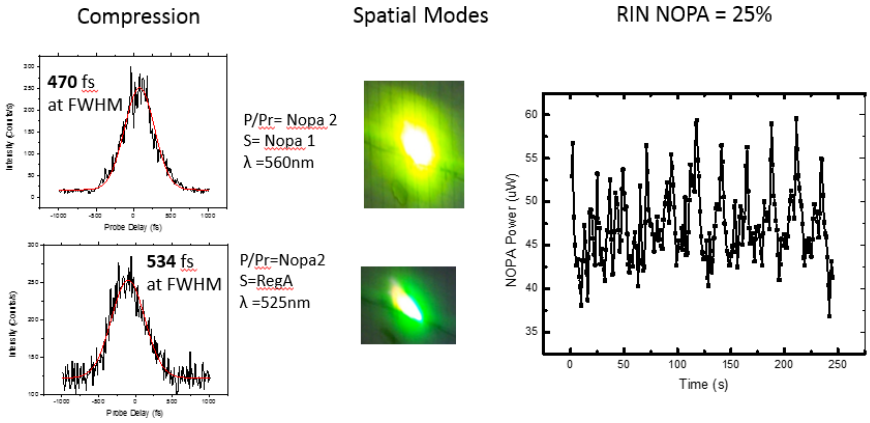

Figure 4.17: Initial time correlation measurements(left) yielded response function 10x larger expected at transform limit. The spatial profiles of both NOPAs were also not ideal for microscopy measurements. The stability of the system was rather poor as well with relative intensity noise at 25 %.

with any of the remaining two being used as the Stokes pulse (assuming the Stokes is redder in frequency than the Pump and Probe). Using the degenerate CARS signals obtained by having NOPA 2 at 615 nm serve as the pump and probe, and having NOPA 1 at 708 nm serve as the Stokes, an anti-Stokes signal can be observed at 560 nm (top left). If either of the NOPAs are scanned realtive to each other in time, a pulse correlation function can be

extracted. Such a measurement between these two pulses yields a pulse correlation time of 470 fs, a factor of 10 larger than should be at transform limit. Similar measurements using NOPA 2 as the pump and probe and the amplifier output at 800 nm as the Stokes, which yield a signal at 525nm show a correlation time of 534 fs, also about 10x larger than expected. As the compressors used for the NOPAs were set up to provide minimal negative GVD, the positive GVD that is generated in the pulse by the FLUOVIEW system by having the beams traverse beam resizing telescopes and microscope objective require a lot more negative GVD to compensate for. Thus the pulses accrued positive GVD from the FLUOVIEW and were stretched significantly at the sample position. In addition to the temporal stretching, the spatial modes of the NOPAs (shown in Figure 4.17) were not ideal for focusing with a high NA microscope objective. For microscopy purposes, an ideal Gaussian spatial profile in both horizontal and vertical directions is preferred. If the beam is elliptical, the shorter diameter will focus later than the wider diameter in propagation direction after passing through a focusing optic. Such a small aberration can distort the spot size of the beam at the sample position also serving to distort the wavefront of the pulse. In addition to the spatial and temporal distortion, the relative intensity noise of the NOPAs where the modulation of the noise is divided by the average total power in the sample series, was 25%. For a measurement that seeks to study the single molecule, which contains a very limited photon flux of signal, such a high noise level, amplified by the nonlinearity of the measurement is detrimental to the study.

As such, a few changes were put in place to compensate for the spatial, temporal and noise aberrations in the system. Firstly, because the compression of the amplifier is optimized via the grating compressor for the generation of NOPAs, the grating compressor cannot be adjusted to compensate for the positive GVD picked up by the amplifier output in the FLUOVIEW. Thus a prism compressor was added for the amplifier output, which was picked off, by a beam sampler before proceeding into NOPA pumping by a beam sampler. This early pickoff also allows use of an amplifier output unperturbed by the SHG process. The

compressors for the NOPAs had the distance between the prisms elongated accordingly to add the necessary negative GVD to compensate for the FLUOVIEW optics. Secondly, all the beams; the amplifier output, and the 2 NOPAs passed through a spatial filter similar to the ones implemented on the 1kHz NOPAs in Chapter 3, to ensure a Gaussian spatial mode for use in the microscope. To deal with the high relative intensity noise, an enclosure was placed around the NOPA generation stages thereby lowering the noise to a manageable 4.8%. The three beam time correlation function, generating a signal at 565 nm, with the new compression in place generated an instrument response function of 56 fs. The time correlation function, relative intensity noise, and the spatial profile of the NOPAs is depicted in Figure 4.18.

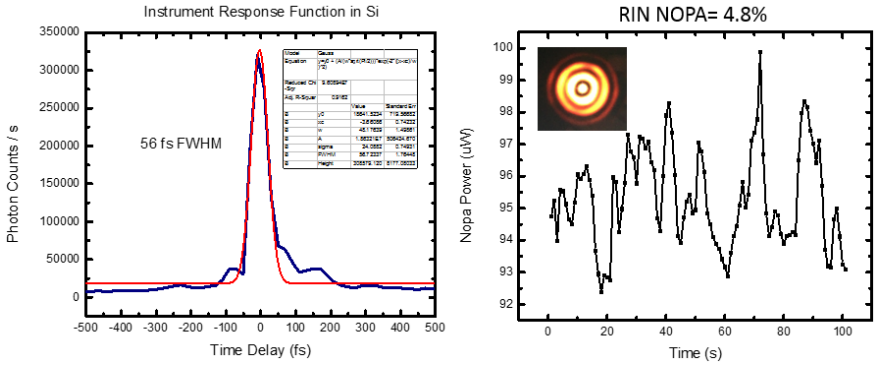

Figure 4.18: After expanding the compressors to compensate for the chirped pulses, The time correlation function of all three beams was measured to be 56 fs. The spatial modes were cleaned up by use of a telescope and spatial filter. A box was assembled to shield the NOPAs from air currents, reducing the relative intensity noise to less than 5%.

A schematic depicting the 250 kHz Microscopy setup with three colors, giving a unique frequency for the time delayed anti-Stokes signal is depicted in Figure **??**.

The implemented changes are shown in the Figure, with the absence of the spatial filters. In the current regime, the system is capable of imaging in the forward and back scattered geometries (Figure 4.20) allowing for correlated measurements. This flexibility greatly simplified correlation between the nonlinear microscopy images and the SEM from which the samples are characterized (inset of Figure 4.20).

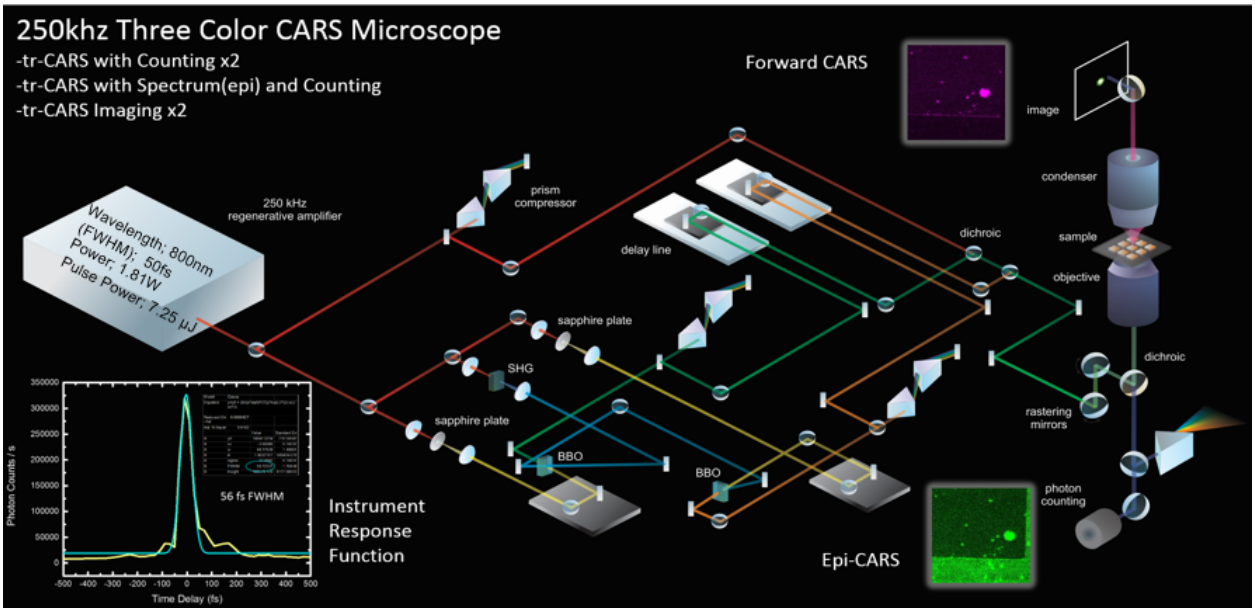

Figure 4.19: The Schematic for the modified Three Color Four Wave Mixing Microscope. The Chirped Pulse amplifier proved 7.25 μJ per pulse used to drive two sequentially pumped NOPAs after having a small amount picked off to be used in conjunction with the two tunable colors for single molecule microscopy. The system allows for time resolved imaging and photon counting in the forward and backscattered geometries as well as the option to collect time resolved spectra in the backscattered geometry.

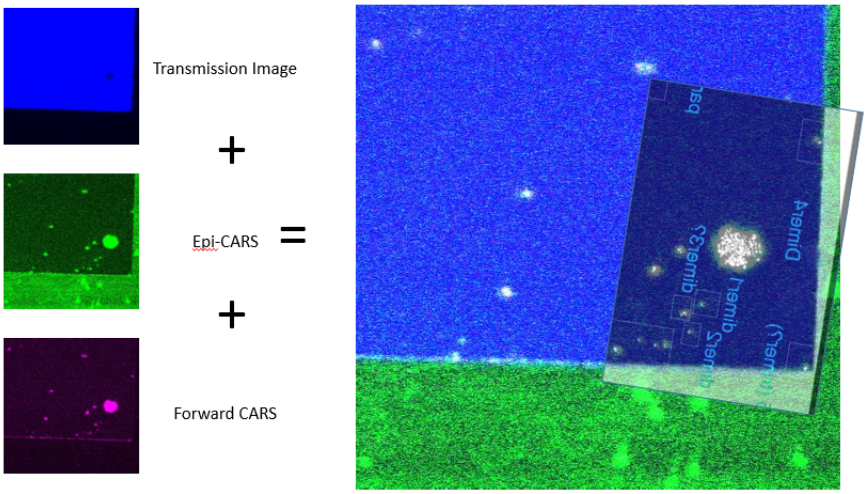

Figure 4.20: The system is designed to detect the anti-Stokes photons and generate an image in the back and forward scattered geometries. When correlated with the known SEM of the sample, locating and correlating the position of one or more nanodumbbell systems becomes possible.

The modified options on the detection allow for measurement of the spectrum from the backscattered geometry, if the FLUOVIEW is programmed to park on a pixel of choice, via a monochromator/CCD combination(Andor Shamrock 303i/iDus CCD). Detection can also be conducted in a photon counting regime (SR400). A discriminator level is used to distinguish between the photons and dark counts on the PMT along with a gating scheme where the signal is counted only in a window corresponding to the rise time of the PMT when a laser pulse is incident. Effectively this allows for dark counts on the order of 8-10 per second. The signal is usually on the order of 1000 counts for incident pulse energies of 5 μW per pulse.

4.4.2 Local Field Intensity

For the molecular system in question, consisting of two gold nanodumbell spheres spaced approximately a nanometer apart, at the local field intensity of 1 V/nm, there exists the possibility of electron shuttling from one sphere to the other, perhaps using the molecule as a bridge. The effects of such a perturbation will not be covered here however it is expected that such an event will heavily perturb the sought after measurement. Care will be taken to avoid such intensities in the experiment so as to avoid the undocumented effects on our measurement.

The irradiance at the sample position is calculated by the peak power from the input laser fields. The peak power is calculated by taking the average power (5 μW) at the sample position, dividing it by the repetition rate (250 kHz) to resolve the power per pulse (40 pJ) and then divided by the duty cycle of the laser pulse (50 fs);

$$\frac{5 * 10^{-6} \frac{J}{s}}{250000 Hz} * \frac{1}{50 * 10^{-15} s} = 400 \frac{J}{s} = 400 W \tag{4.4}$$

This is then focused with a 1.3NA oil Objective making the spot size at the beam waist 1 μ in diameter. A trivial $\pi(\frac{d}{2})^2$ calculation gives the laser spots size an area of $8 * 10^{-13}\ m^2$. The size of the sample, encased in a silica shell is approximately 300 nm is diameter, giving an area of $8 * 10^{-14}\ m^2$. The sample effectively feels 9% of the laser power at the laser beam waist.

The conversion from irradiance in $\frac{W}{m^2}$ to $\frac{V}{nm}$ for the molecule;

$$27.4\sqrt{\frac{W}{m^2}}\frac{1}{10^9 nm} = 0.185\frac{V}{nm} \tag{4.5}$$

This means that for one laser field with an average power of 5μW at 250kHz, the local field is well below the 1 V/nm limit. This experiment requires three pulses, and if each is set at 5μW, then the local field should not exceed, by conservative estimates, 0.557 V/nm. Note that in this calculation we have neglected local field enhancements. An enhancement of $\frac{E}{E_0} = 100$ is minimally required to see single molecule SERS. When this is taken into account, we recognize that that we exceed intensities that lead to field emission. The fact that repetitive measurements can be carried out on a single nanostructure without sample damage, must be attributed to the protection provided by the silica shell.

4.4.3 Early Results

Though experiments to reproduce the published work using three colors are still underway, early results have been measured and are depicted in Figure 4.21.

The early data (left pane) shows oscillations corresponding to the beat frequency (33 cm^{-1}) between the two prepared vibrations at 1600 cm^{-1}. While the signal does not decay into

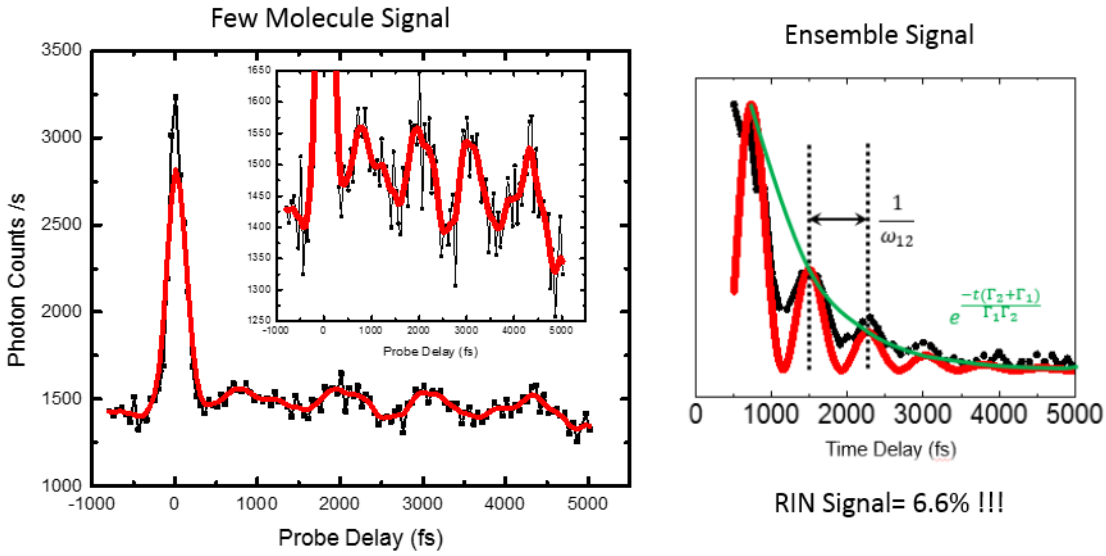

Figure 4.21: The first time resolved traces (left) show an oscillation with a period of 1 ps as expected, however the system appears to not be decaying into phase noise as predicted for the single molecule. However the system also does not exhibit the ensemble decay (right pane) indicative of a large number of molecules in the sample position. The conclusion is that the time trace must arise from more than one but less than many for these characteristics.

phase noise like the single molecule predictions discussed earlier in the chapter, the signal also doesn't follow the ensemble-like decay (right pane). This is possibly a few molecule coherence trace, where the coherent phases of a few members are averaging to give the time dependent oscillation but there are not enough molecules to see the coherence decay within the ensemble time constant. The relative intensity noise of the nonlinear signal is 6.6 %.

4.5 Conclusions and Moving Forward

I presented the first measurements that follow the evolution of a vibrational coherence on the ground state of a single molecule under ambient conditions[18]. tr-SECARS was used to prepare a vibrational superposition of two states, and a third pulse probed the phase correlation between the states as they evolved in time via a spectrally filtered, anti-Stokes

photon. Plasmonic enhancement in the form of two gold nanospheres was employed to bring the single molecule response to a measurable level via use of amplification and subsequent broadcasting of the single molecule signal from the junction. The two nanospheres serve as a viable tool to interrogate single or few molecule entities and have been shown to endure the peak power of ultrafast pulses. Real time monitoring of vibrational evolution has been shown on the ground electronic state. Such a measurement can be extended to prepare and probe a coherence on multiple electronic states of a single molecule, with the possibility of complete quantum state reconstruction.[204, 205] Coherent manipulation of quantum bits has been demonstrated using a pair of phase-locked pulse pairs.[206, 207] Quantum bit manipulation is possible on the preparation, evolution, and interrogation steps of electronically resonant FWM. [208–210] However, this has yet to be demonstrated in the single molecule limit. Proof of coherent evolution on a single molecule is a stepping stone to such applications. With a new three color microscope system, the course is set to define the measurements which aim to unlock the possibility of measuring and subsequently manipulating the wavefunction of a single molecule. The following chapter depicts the intricacies and the experimental requirements to execute such a measurement, with details regarding the information such a measurement can yield.

Chapter 5

Tomographic Quantum State Reconstruction

The complete description of dynamics is in phase space representation via the Wigner Distribution Function (WDF)[19]. The WDF allows the treatment of classical, semi-classical, and quantum dynamics equally. Determination of the WDF is equivalent to the complete determination of the state. An important aspect of the WDF is that it can be generated either from an experimentally measured density via the Inverse Radon Transform (IRT), or it can be generated directly from a wavepacket by the Wigner Transform[19]. Experimentally, one measures the density, and in order to reconstruct the WDF with fidelity there are requirements on the measurement. These requirements will be covered in detail by considering the reconstruction of the $|0> + |1>$ harmonic oscillator state through different measurements. Quite clearly, the measurement must span the complete space of the evolving state. In the case of one dimensional vibrational wavepacket motion, it is necessary to measure the marginals of the WDF, i.e., the density in coordinate or momentum, must be measured from turning point to turning point. The density is usually measured spectroscopically and here the experimental conditions that are capable of generating a complete WDF are examined.

First, in the most clear example, we will consider the Kerr gated detection of emission from an evolving state. As long as the emission terminated on a well defined potential, either known or approximated, it is possible to image the density (or the marginal). In this case we consider an evolving $|0><1|$ vibrational coherence on an initial electronic state emitting to a bound electronic final state. The reproduction fidelity of the WDF depends heavily on the width of the Kerr gate. The gated spectra as a function of the gate delay, should produce a set of snapshots over π phase of the evolution. If the width of the gate is infinitely short, the evolved density is washed out by a wide Gaussian in spectrum. If the gate is too long then the density appears stationary in spectrum. The gate has to be on the order of a fraction of the period of motion of the wavepacket and the turning points must be contained in the inverse gate width (the bandwidth). $\frac{\partial V(x)}{\partial x}$ in one dimension of the final state potential determines how widely the spectrum is spread. This spectrum has to be within the uncertainty limited bandwidth of the Kerr gate width. In regards to the potential energy surfaces, in the limit where both initial and final states are harmonic and not displaced with respect to the energy minima, then the projection of the two vibration superposition will only overlap with the analogous two vibrations on the final potential. In this limit, the spectrum collapses to a single line, and evolution cannot be tracked. Clearly, the projections must span many states for a good reproduction of the evolving state.

Using the general example of two potential energy surfaces, the strategy will be applied to demonstrate that such a measurement is possible using time resolved four wave mixing (FWM) via Spectrally Resolved Transient Grating (SRTG)[204]. In this approach, two degenerate pulses prepare a population grating that involves a two state superposition on an initial excited state. A probe pulse, incident onto the system at a later time, creates a coherence between the present initial state and a higher energy electronic state. The dynamic overlap between the initial and final states projects the prepared spatiotemporal density in the time resolved spectrum of the detected third order polarization. In this case, the probe pulse should be short in comparison to the period of motion, in order to

capture the wavepacket at discrete phases and in order to span all vibrations on the higher energy potential energy surface that fall within the Franck-Condon window. The electronic dephasing time serves the analogous role of the Kerr gate width in the previous example. If the dephasing time is instantaneous, the dynamics are washed out via a large Gaussian in spectrum. If the dissipation time is long, reemission will be present and modulate the measured spectrum. The latter can be filtered out using Fourier filtering. The following is a numerically generalized analysis of the required conditions to reproduce wavepacket motion in the highest fidelity as compared to a simulated wavepacket transfered into the WDF directly.

5.1 The $|0><1|$ coherence, Kerr gated density reconstruction

Assume a $|0> + |1>$ superposition is prepared on some potential energy surface and evolves as a function of time. The normalized wavefunction in coordinate representation is:

$$\psi[x, n, x_\delta] = \sqrt[4]{\frac{m\omega}{\pi\hbar}} \frac{e^{\frac{-m\omega(x-x_\delta)^2}{2\hbar}}}{(2^n n!)^{\frac{1}{2}}} (-1)^n e^{\frac{m\omega}{\hbar}(x-x_\delta)^2} \frac{\partial^n e^{\frac{m\omega}{\hbar}(x-x_\delta)^2}}{\partial x^n} \tag{5.1}$$

for the nth harmonic vibrational eigenfunction on a quadratic potential centered at δ. The normalized wavefunction for the 0th and 1st vibrational states appears below;

The time evolution of the density, $\rho_{10}(t) = \psi^*(x,t)\psi(x,t)$, of the superposition of states;

$$\psi(x,t) = \psi_0(x)e^{-\imath E_0 t} + \psi_1(x)e^{-\imath E_1 t} \tag{5.2}$$

is shown in Figure 5.2. The wavepacket has a period of evolution given by the difference in energy between the two states. The snapshots depicted below at a few relative phases Φ,

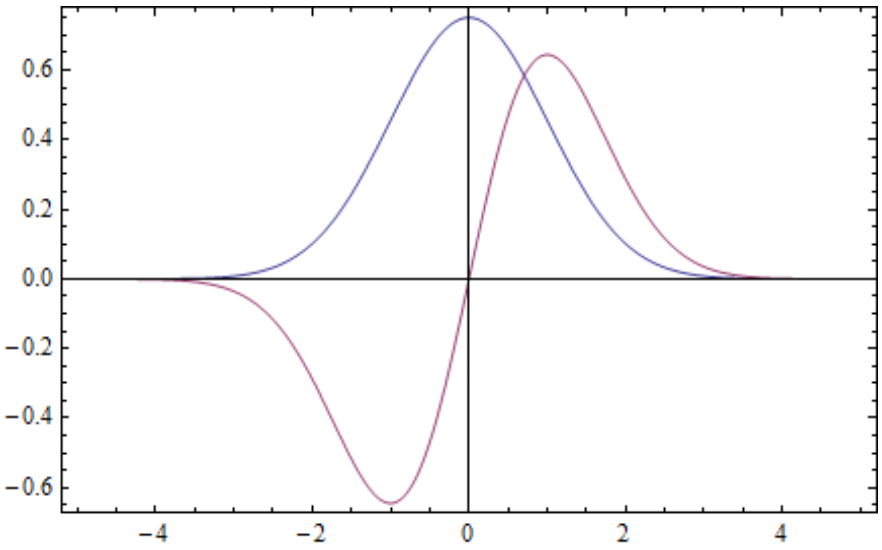

Figure 5.1: Wavefunction for the 0th(Blue) and 1st(Red) eigenstate of a Harmonic potential energy surface with x(and x_δ) units of length defined by $\sqrt{\frac{m\omega}{\hbar}}$

where $\Phi = (\frac{E_1 - E_0}{\hbar})t$;

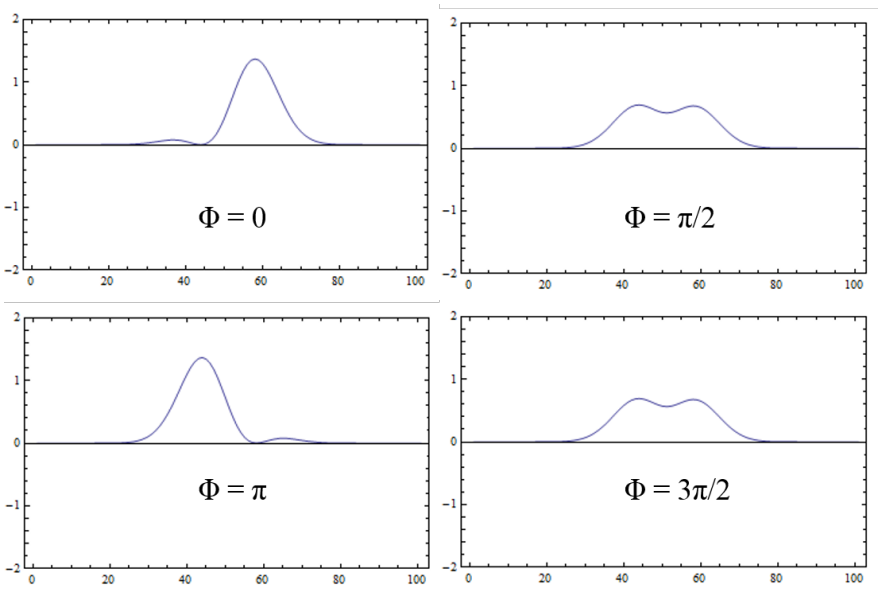

Figure 5.2: The density ρ_{10} of the $|0><1|$ superposition wavepacket evolving in time a few select relative phases

The continuous evolution of the density, $\rho_{10}(t)$ is shown in the image plot below;

The time dependent density can be projected into time dependent spectral information and

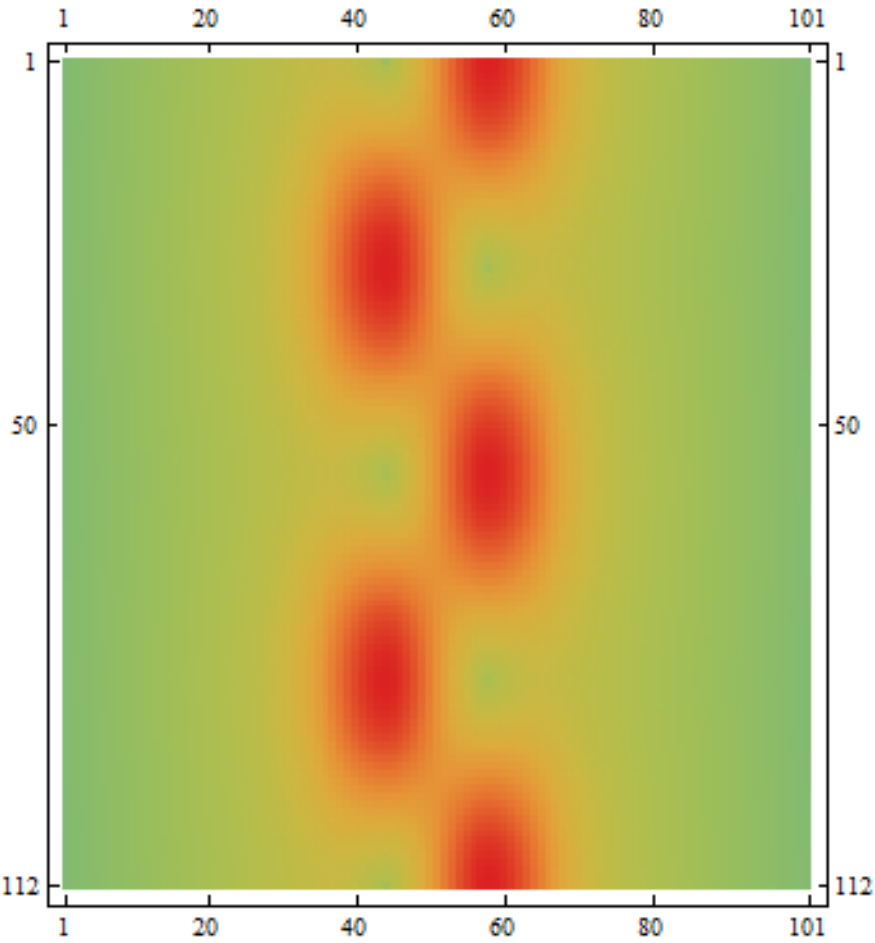

Figure 5.3: The $|0><1|$ superposition wavepacket evolving in time, in discrete points; the x-axis is vectorized in steps of 0.1 from -5 to 5, and the y axis is vectorized in time in steps of 6 fs from 0 to 666 fs (two periods of a 100 cm^{-1} difference in energy between the two eigenstates)

measured. The simplest of these schemes is to consider the emission of the prepared superposition to a lower electronic state. The spectral profile of the emission will be determined by Franck-Condon factors on the two electronic states e and g. The probability that the excited electronic state vibrational wavepacket will populate a particular vibrational level on the lower energy ground electronic state is proportional to the square of the overlap of the vibrational wavefunctions of the original(excited) and final(ground) states;

$$| < \psi_e^*(x - x_\delta)|\psi_g(x) > |^2 \tag{5.3}$$

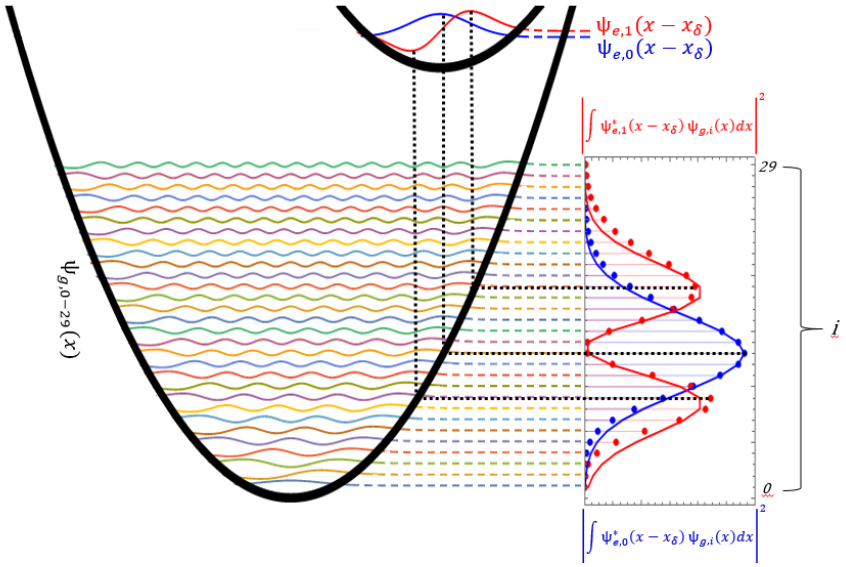

Figure 5.4: Excited and ground state potentials, the x-axis represents nuclear motion and the y-axis is energy. Vibronic transitions take place instantly(vertically) relative to nuclear motion. If there is a difference in minimum energy between the two potentials, the vibronic transition from one vibration on the initial state can populate multiple vibrations on the final state, such that the condition in Equation 5.4 is satisfied. The wavepacket(solid lines in right inset) from the excited state can be reproduced by Franck-Condon factors(dotted, right inset) on the ground state with a slight distortion due to the curvature of the ground state potential, $\frac{\partial V(x)}{\partial x} \neq$ a constant

Radiative transitions, such as ones between vibrational levels on two different potentials, take place instantaneously(vertically) when compared to the time-scale of nuclear motion(Figure 5.4). The final electronic state may have a different equilibrium position x_δ than that of the initial electronic state. If the potentials have identical curvatures, such that the harmonic frequencies($\omega_g = \omega_e$) and the minima($x_\delta = 0$) are equal, then the Franck Condon overlap only exists between identical states on the initial and final electronic states (i.e. $< \psi^*_{g,i}(x)|\psi_{e,ii}(x) >= \delta_{i,ii}$). If $x_\delta \neq 0$ then a vibrational state on the initial surface has overlap with more than one vibrational state on the final surface such that;

$$\sum_{ii}^{\infty} | < \psi^*_{e,i}(x - x_\delta)|\psi_{g,ii}(x) > |^2 = 1 \tag{5.4}$$

In order to successfully transcribe the $|0><1|$ spatial wavepacket that propagates on the excited state, the lower electronic state must span both $\psi_{e,0}(x,t)$ and $\psi_{e,1}(x,t)$. This condition is always fulfilled for a harmonic potential, which is assumed in the present. The larger the displacement in x_δ the more states are needed on the ground state to meet the above condition. This is illustrated for a case where $\omega_g = \omega_e = 100\ cm^{-1}$, $x_\delta = 5$ in Figure 5.5.

5.2 $|0><1|$ tr-Spectrum

Suppose there exist two potential energy surfaces, such as in Figure 5.4, separated in energy by 15000 cm^{-1}. The initial higher energy surface has a $|0><1|$ vibrational superposition 100 cm^{-1} apart in energy. For a $x_\delta = 5$ between the two potential energy surfaces, the lower energy surface needs 30 vibrational states, spaced in energy by increments of 100 cm^{-1}(in this example) to meet the condition in Equation 5.4. Though the energy surfaces can be Morse potentials and non-identical, as is in reality, for the sake of this exercise, it is assumed that the states are identical harmonic potentials displaced in the energy minimum $x_\delta \neq 0$.

The time dependent transition probability of the $|0><1|$ vibrational superposition on vibration ii on ground state is;

$$S_g(t) = |\sum_{ii}^{30}\sum_{i}^{2} < \psi^*_{g,ii}(x)|\psi_{e,i}(x - x_\delta) > e^{-\imath(E_{e,i}-E_{g,ii})t}|^2 \tag{5.5}$$

The sum is over the initial and final vibrational states (i is v_e=0,1 and ii is v_g=0-29).

Individually, the projection of the v=0,1 vibrations on the v=0-29 vibrations on the ground state, is depicted in Figure 5.5. Although F-C factors are time independent, if v=0,1 is prepared and propagates, a time dependent spectrum emerges in Figure 5.6.

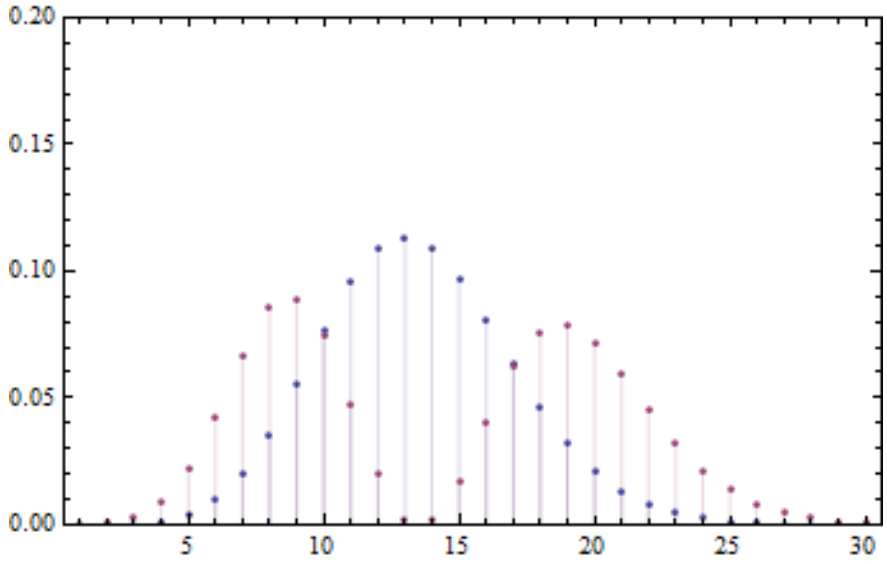

Figure 5.5: Transition probability(y-axis) of v_e = 0(blue) and 1(red) to v_g=0-29(x-axis). If the condition in Equation 5.4 is met, the spatial wavefunction is reproduced in full fidelity. If it is not met, the spatial wavefunction will only be represented partially.

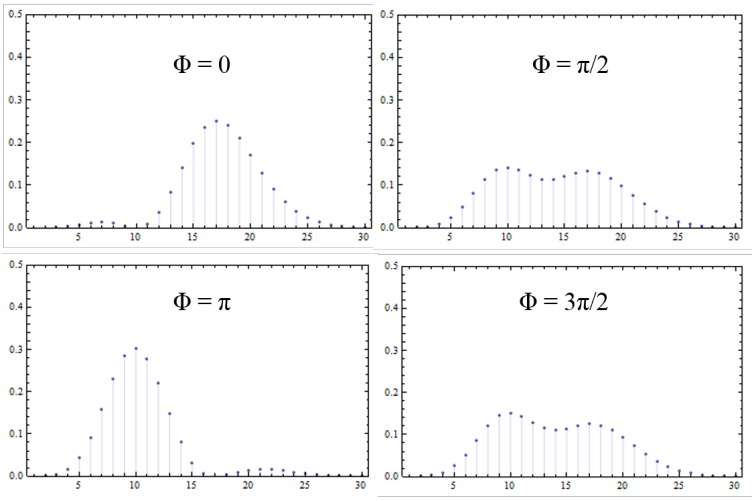

Figure 5.6: Transition probability(y-axis) of v_e = 0,1 (Blue) to v_g=0-29(x-axis). The transition overlap is time dependent with a period of $\frac{1}{3}$ ps, analogous to the 100 $cm^{-}1$ difference in energy between the v=0,1 vibrations.

Reproduction of the time dependent transition probability from v=0,1 to v=0-29 can be experimentally captured by a Kerr gate and a monochromator. In the absence of a Kerr gate, the excited state vibrational wavepacket is continuously radiating to the ground state. If the transition is intelligently gated in time to capture a window of a specific phase of

the wavepacket motion then the spatial modulation of the wavepacket in Figure 5.2 can be reproduced in spectrum, as depicted in Figure 5.7.

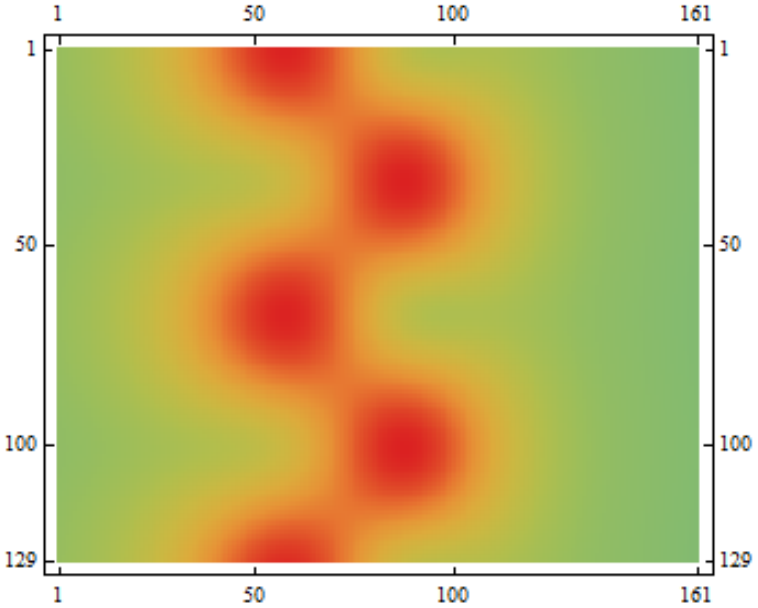

Figure 5.7: The spatial wavepacket depicted in Figure 5.2 now depicted in a vectorized spectrum using Equation 5.6. The x-axis is vectorized from 12,0000 cm^{-1} to 16,0000 cm^{-1} in steps of 25 cm^{-1} and the y axis is the Kerr Gate Delay from 0 to 640 fs in steps of 5 fs for a gate width(Δt) of 20 fs

Similar to Equation 5.5, Equation 5.6 contains the Franck Condon overlap and the energy difference between vibrational eigenstates, in addition to the Kerr Gate, which isolates a window of the wavepacket propagation in time, and a Fourier filter to transform the Kerr gated window into a spectrum, analagous to a grating in a monochromator.

$$S(\tau,\omega) = |\int_{t-2\Delta t}^{t+2\Delta t} e^{\imath\omega t} e^{-(\frac{t-\tau}{\Delta t})^2} \sum_{i}^{30} \sum_{ii}^{2} < \psi^*_{g,i}(x)|\psi_{e,ii}(x-x_\delta) > e^{-\imath(\frac{E_{e,ii}}{\hbar} - \frac{E_{g,i}}{\hbar})t}|^2 \qquad (5.6)$$

There is a distinct relationship between choice of the Kerr gate and the period of the wavepacket motion. For a wavepacket that oscillates with a period of motion of 333 fs the following is depiction of a signal measured with a 5 fs (Figure 5.8), 10 fs (Figure 5.9), 20 fs (Figure 5.10), 50 fs (Figure 5.11), 100 fs (Figure 5.12), 150 fs (Figure 5.13), and 200 fs (Figure 5.14) Δt Kerr gate widths;

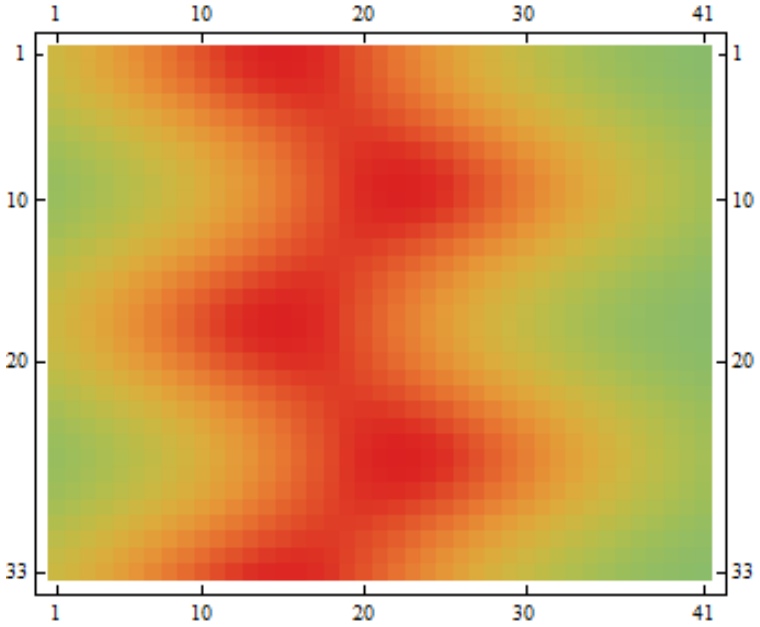

Figure 5.8: The $|0><1|$ excited state vibrational superposition emitting to a manifold of vibrations on the ground state with gated by a Kerr gate $\Delta t = 5$ fs

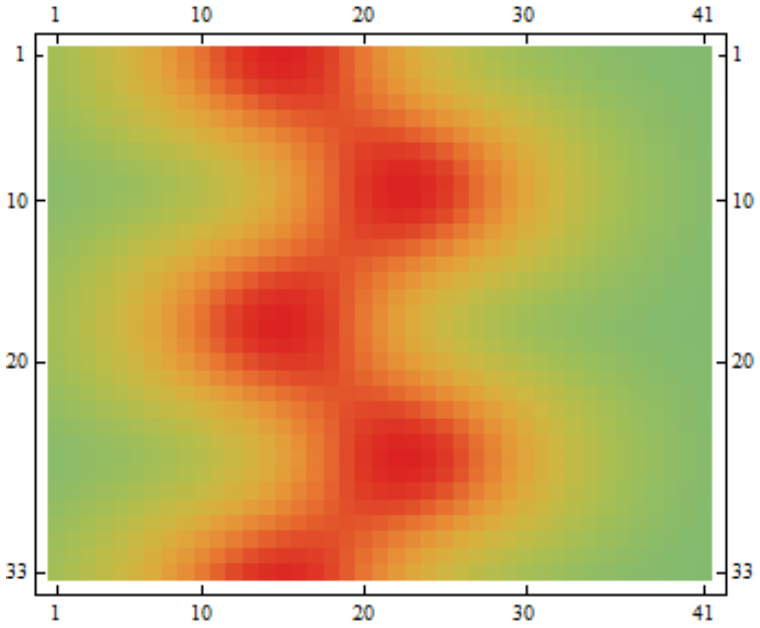

Figure 5.9: The $|0><1|$ excited state vibrational superposition emitting to a manifold of vibrations on the ground state with gated by a Kerr gate $\Delta t = 10$ fs

In the this figure series, if the Kerr gate is much shorter than the period of the superposition, the spatiotemporal profile is well represented but spectrally broadened due to the time-

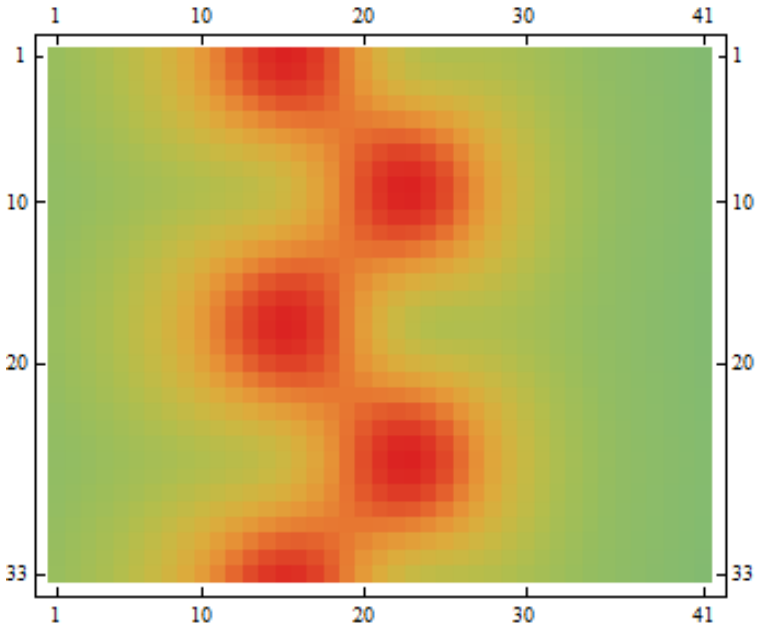

Figure 5.10: The $|0><1|$ excited state vibrational superposition emitting to a manifold of vibrations on the ground state with gated by a Kerr gate $\Delta t = 20$ fs

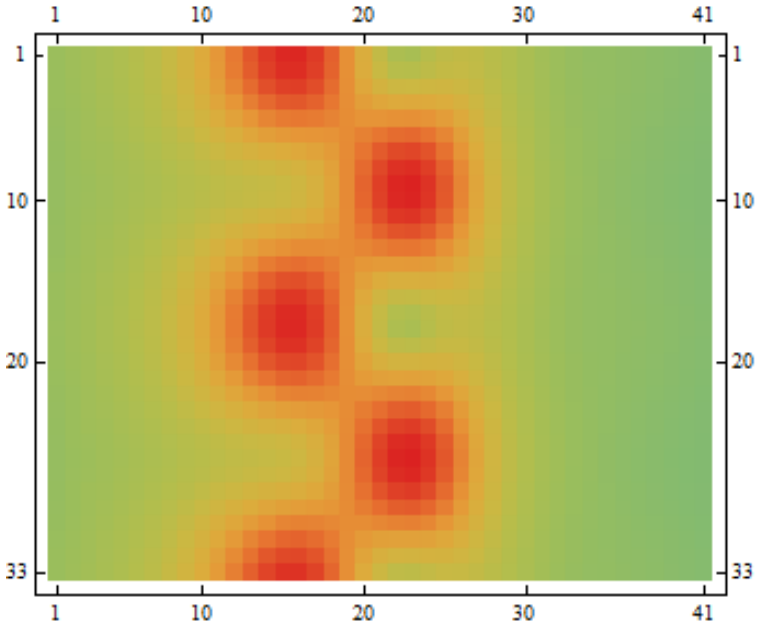

Figure 5.11: The $|0><1|$ excited state vibrational superposition emitting to a manifold of vibrations on the ground state with gated by a Kerr gate $\Delta t = 50$ fs

frequency bandwidth limitation; The smaller the Kerr gate, the larger the bandwidth of the spectrum. If the Kerr gate is made to be larger than half the period of motion, then the

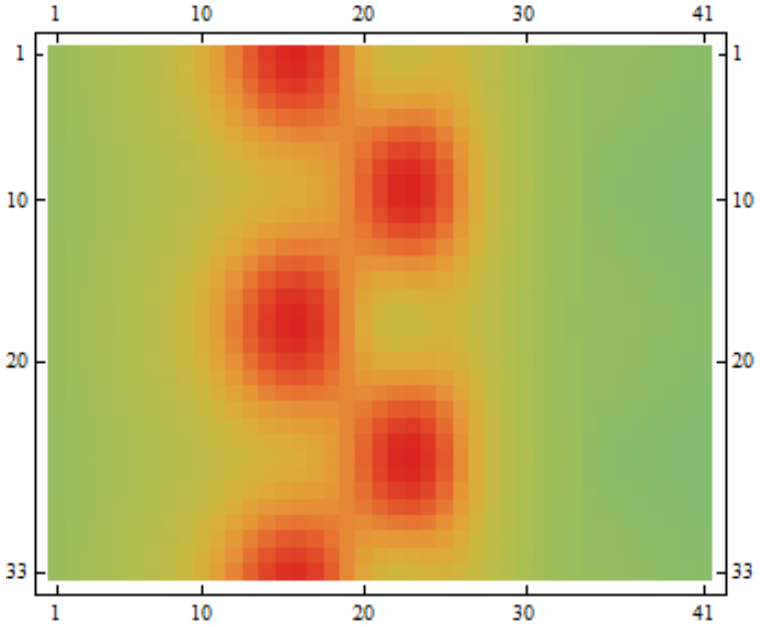

Figure 5.12: The $|0><1|$ excited state vibrational superposition emitting to a manifold of vibrations on the ground state with gated by a Kerr gate $\Delta t = 100$ fs

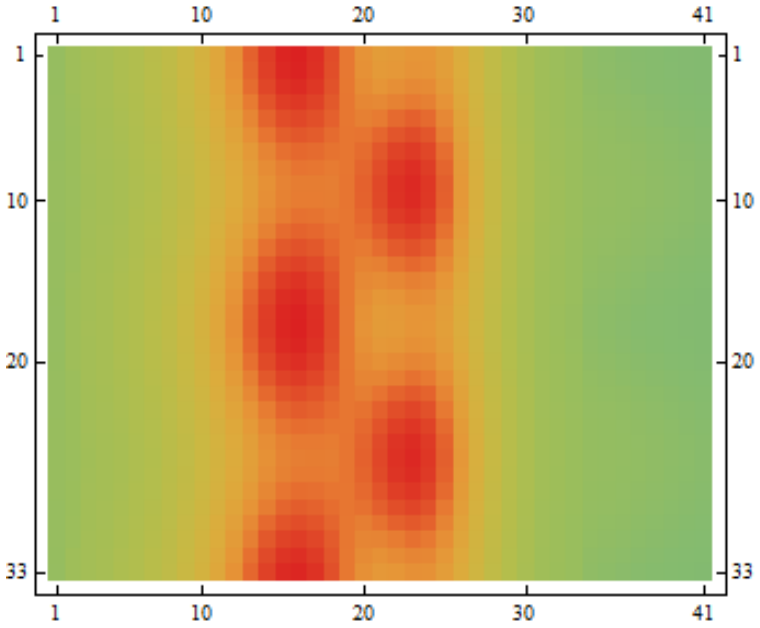

Figure 5.13: The $|0><1|$ excited state vibrational superposition emitting to a manifold of vibrations on the ground state with gated by a Kerr gate $\Delta t = 150$ fs

spatiotemporal dynamics get smoothed over. The case is best illustrated when the Kerr gate is 200 fs in Figure 5.14, which is slightly larger than half the period of motion (333 fs).

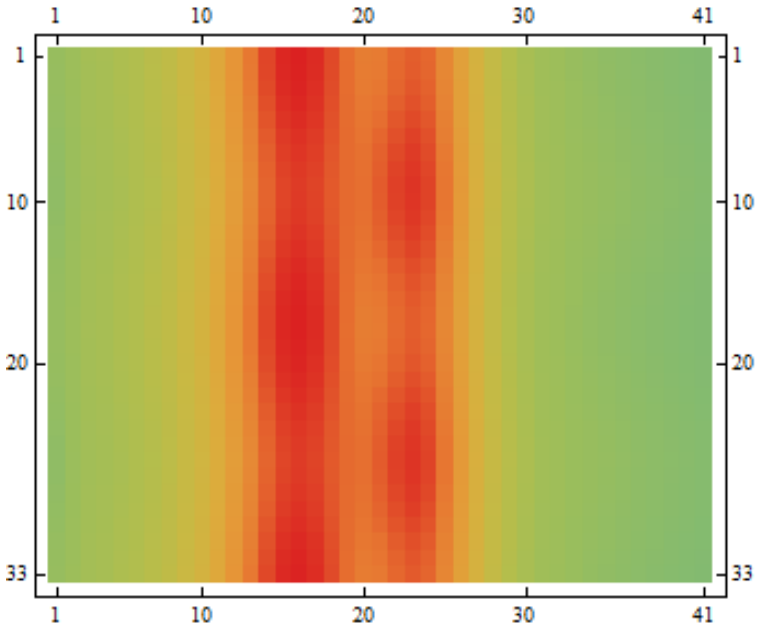

Figure 5.14: The $|0><1|$ excited state vibrational superposition emitting to a manifold of vibrations on the ground state with gated by a Kerr gate $\Delta t = 200$ fs

An exact alternative to temporally gating the wavepacket evolution is to convolve the ungated spectral response in Equation 5.6 with the spectral width of the inverse Δt of the Kerr gate.

5.3 Measuring $|0><1|$ via tr-Transient Grating

In the previous section, the Kerr Gated emission from a higher energy state containing the vibrational superposition was considered, assuming the wavepacket was already prepared and emitting to a lower energy ground state vibrational manifold. Here the preparation is considered. Spectrally resolved transient grating(SRTG) measurements prepare and probe the vibrational wavepacket motion in real time using a scheme similar to the one depicted in Figure 5.15.

A population is prepared with degenerate pulses, on an excited state and evolves as a density;

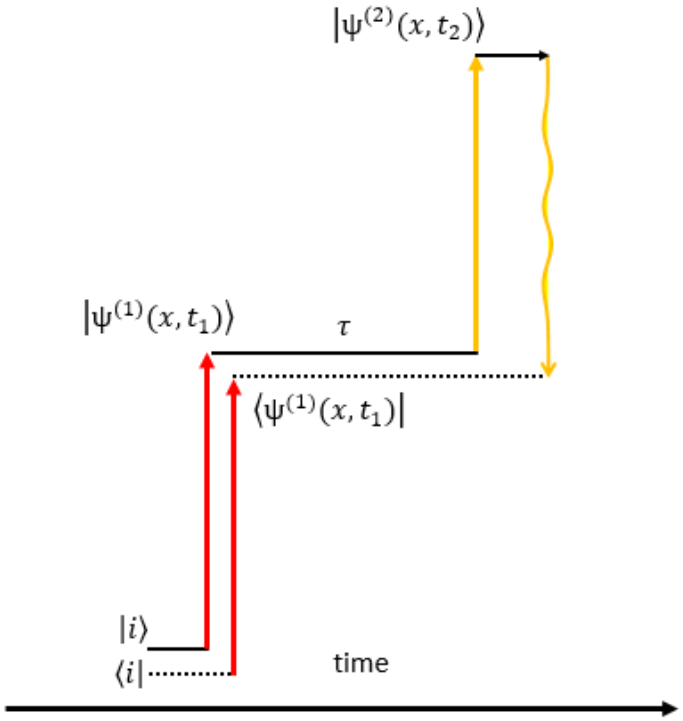

Figure 5.15: Time Circuit Diagram of Transient Grating. A population is prepared via a population grating using two degenerate femtosecond pulses(red arrows), resonant with the electronic transition between the a ground state and an excited state. The density interrogated as a function of the time delay τ between the excitation and the third laser pulse resonant with a transition to a higher energy excited state.

$$\rho_{1,1}(x,\tau) = \psi^{(1)*}(x,\tau)\psi^{(1)}(x,\tau) \tag{5.7}$$

along t_1. A probe pulse, resonant with a transition to a higher excited state, creates the electronic coherence;

$$\rho_{1,2}(x,\tau,t_2) = \psi^{(1)*}(x,\tau)\psi^{(2)}(x,t_2) \tag{5.8}$$

which evolves along t_2 until it radiates as the third order polarization;

$$P^{(3)}(x,\tau,t_2) =< \psi^{(1)*}(x,t_2)|\mu|\psi^{(2)}(x,t_2) >< \psi^{(2)*}(x,t_1)|\mu E(\tau)|\psi^{(1)}(x,t_1) > \tag{5.9}$$

The detected signal probed at a time τ is integrated over t_2 and spatial coordinate x and squared by the detector;

$$S(\tau) = |\int_{-\infty}^{\infty}\int_{-\infty}^{\infty}[P^{(3)}(x,\tau,t_2)]dt_2dx|^2 \tag{5.10}$$

While the information about the evolution along t_2 is lost when a photodiode or photomultiplier tube is used to measure the TG signal, using a monochromator to filter the Fourier components of the signal gives the spectral information about the coherence;

$$S(\tau,\omega) = |\int_{-\infty}^{\infty}\int_{-\infty}^{\infty}e^{\imath\omega t_2}[P^{(3)}(x,\tau,t_2)]dt_2dx|^2 \tag{5.11}$$

The SRTG measurement can be used to prepare and probe spatiotemporal dynamics of the $|0><1|$ vibrational superposition in absence of a Kerr gate as used in the previous example with emission. The vibrational superposition, depicted in atomic units where $\hbar = 1$, is prepared via a population grating such that;

$$\psi^{(1)}(x,t_1) = \psi_{B,0}(x)e^{-\imath E_0 t_1} + \psi_{B,1}(x)e^{-\imath E_1 t_1} \tag{5.12}$$

and

$$\psi^{(2)}(x,t_2) = \sum_{i=1}^{30}\psi_{C,i}(x)e^{-\imath E_i t_2} \tag{5.13}$$

the SRTG probing the spatiotemporal dynamics of the $|0><1|$ Vibrational Coherence is depicted in Figure 5.16.

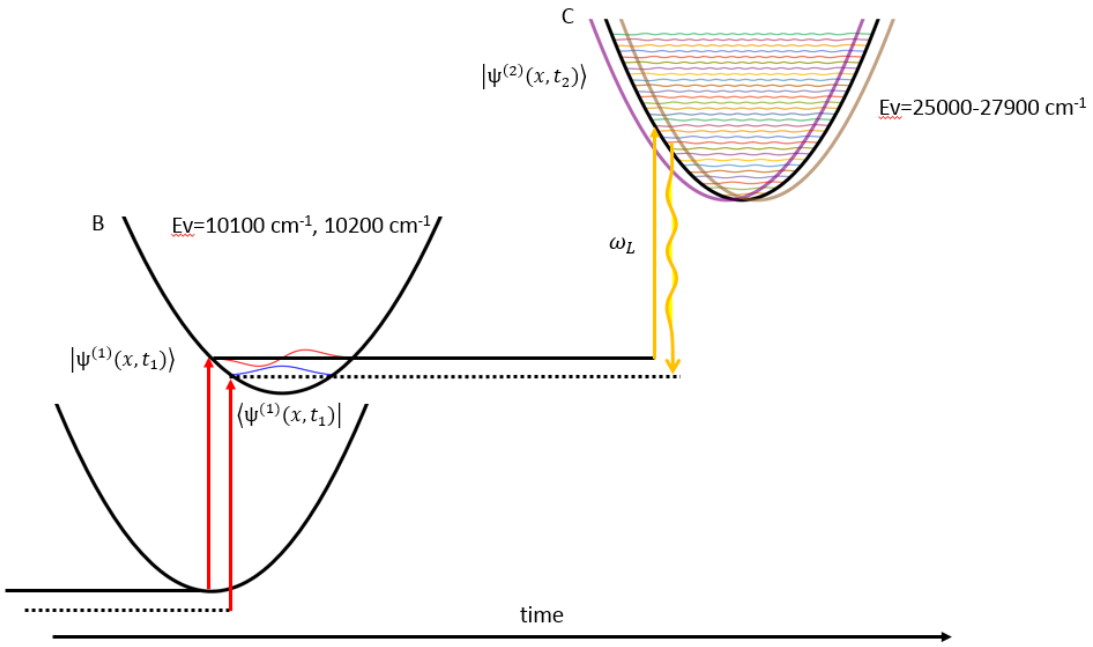

Figure 5.16: Time Circuit Diagram of SRTG. A vibrational superposition is prepared via a population grating using two degenerate femtosecond pulses(red arrows), resonant with the electronic transition between the ground state and an excited state. The density interrogated as a function of the time delay between the excitation and the third laser pulse resonant with a transition to a higher energy excited state. The spectrum of the emission contains the time dependent spatial density

The vibrational superposition evolves along time t_1 after it was prepared at $t = 0$. For the quantified simulation that follows, $E_0 = 100\ cm^{-1}$, and $E_1 = 200\ cm^{-1}$ on an electronic potential energy surface (B) with a minimum at $E_{elec} = 10000\ cm^{-1}$. A third pulse;

$$E(\tau) = e^{(\frac{t_1-\tau}{\Delta t})^2} e^{-\imath E_L(t_1-\tau)} \tag{5.14}$$

where E_L is resonant with the transition between the B state and vibrational manifold on the higher lying excited state (C) having an energy minimum at $E_{elec} = 25000\ cm^{-1}$, probes the population $|\psi_B^{(1)}(x,t_1) >< \psi_B^{(1)}(x,t_1)|$, creating a wavepacket on the C state;

$$\psi^{(2)}(x,t_2) = \sum_{i=1}^{30} \psi_{C,i}(x) e^{-\imath E_i t_2 - \Gamma t_2} \tag{5.15}$$

The wavepacket evolves along the vibrational states i on the C state with a decay time $1/\Gamma$ meant to represent the dephasing of the electronic $|B><C|$ coherence. The time dependent amplitude of the vibration i prepared on the C state, $<\psi^{(2)}_{C,i}(x,t)|\mu E(\tau)|\psi^{(1)}_{B,0}(x,t)>$ depends on the energy of the probe pulse. The probe energy dependence is depicted for a few select states in Figure 5.17.

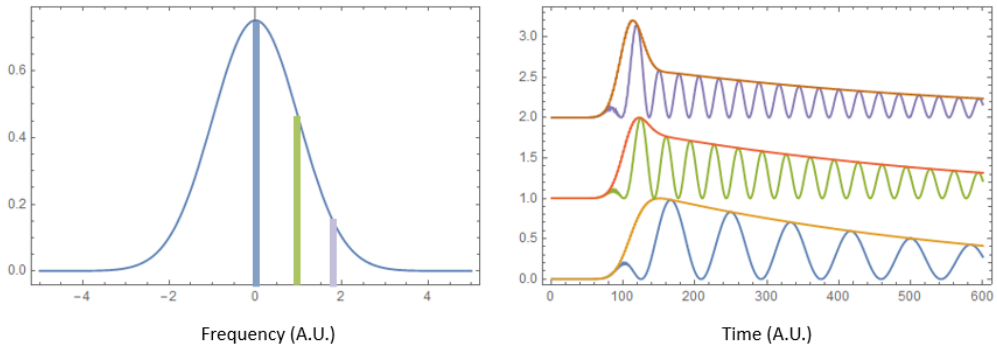

Figure 5.17: Spectral overlap of the Probe Pulse (left graph, Blue), with select vibrations on the C State (left graph, blue, green and purple delta functions). Amplitudes of the prepared vibrations in the time shortly before and after excitation via the probe pulse (right graph, blue, green and purple vibrations and the respective amplitudes). The more resonant the probe, the more amplitude in the respective vibration, which decays with an arbitrary vibrational relaxation time.

If the probe pulse is resonant with vibrational state i, then the full amplitude of the state is prepared and after the action of the probe pulse, the amplitude decays with the dephasing time. If the state is in the wings of the spectrum of the probe pulse, the amplitude of the state is smaller after the action of the pulse and follows the decay of the vibrational relaxation time.

Similarly to the emission model in the previous section, given the proper displacement x_δ between the B and C potentials, the probe pulse can project, in full fidelity, the $|0><1|$ coherence from the B state onto the C state. Figure 5.18 depicts the Franck Condon overlap of vibrational states between the B and C states with the projection according to Equation 5.3.

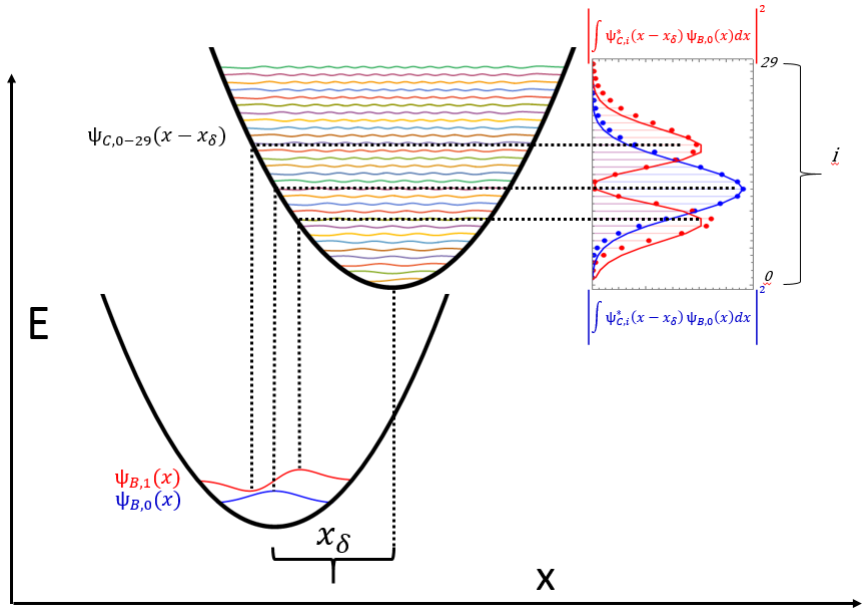

Figure 5.18: Franck Condon overlap factors according to Equation 5.3. The $|0><1|$ wavepacket on the B state is projected onto 30 states on the C potential energy surface. The overlap in the spatial coordinate is determined by the displacement x_δ between the B and C potential energy minima. The project of the $|0>$ and $|1>$ is depicted on the right inset(dots). Note the distortion of the projection when compared to the 0 and 1 wavefunctions (blue and red lines.)

The full expression for $S(\tau,\omega)$ to resolve the spatiotemporal dynamics via SRTG on the C state;

$$S(\tau,\omega) = |\int_{-\infty}^{\infty} e^{\imath\omega t_2}\psi^{(1)*}(x,t_2)\mu\psi^{(2)}(x-x_\delta,t_2) \int_{-\infty}^{\infty}[\psi^{(2)*}(x-x_\delta,t_1)\mu E(\tau)\psi^{(1)}(x,t_1)dxdt_1]dxdt_2|^2 \tag{5.16}$$

The dependence on the probe energy E_L and spatial displacement between the two vibrational energy surfaces x_δ is illustrated in Figure 5.19 for a $\Delta t = 10$ fs, and $1/\Gamma$, the dephasing time of 50 fs. The dependence on the probe pulse duration and the dephasing time will be later explored.

As the displacement between the potentials gets smaller, fewer states are necessary to fulfill

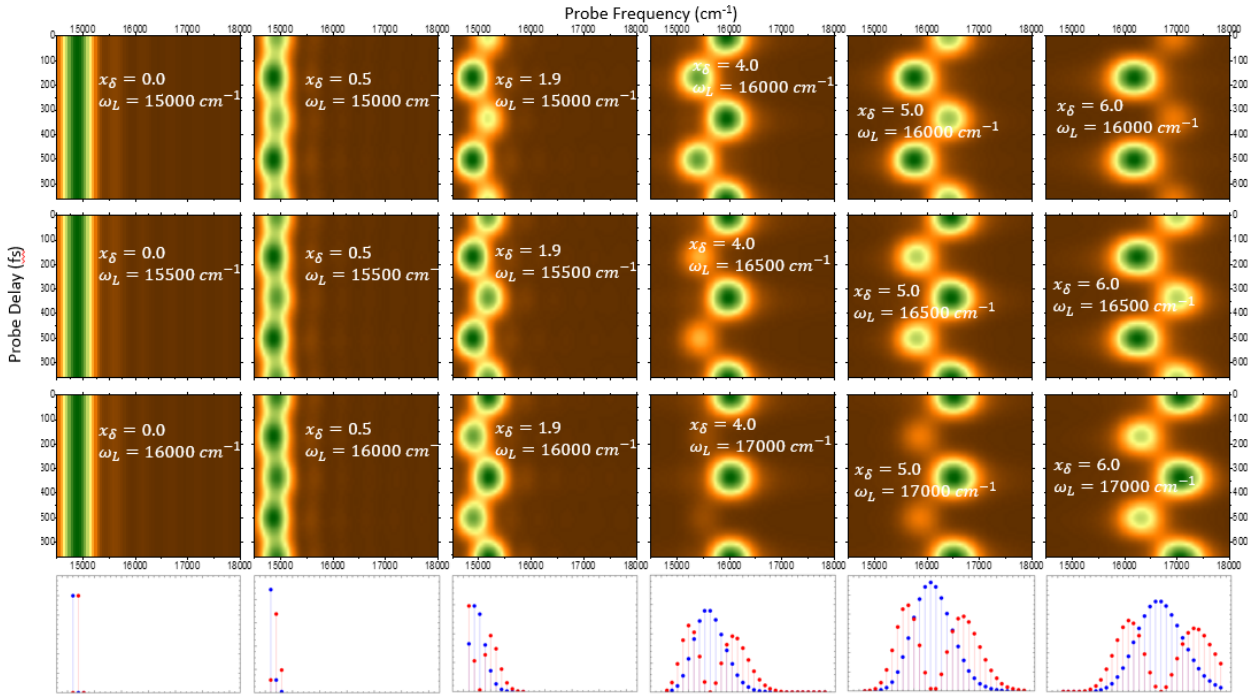

Figure 5.19: $S(\tau, \omega)$ from Equation 5.16 ilustrated for x_δ=0, 0.5, 1.9, 4.0, 5.0, and 6.0, for Probe Energies E_L=15000 cm^-1, 15500 cm^-1, 16000 cm^-1 for the cases with small displacement (0,0.5,1.9) and 16000 cm^-1, 16500 cm^-1, 17000 cm^-1 for the larger displacements 4.0, 5.0, and 6.0. The Franck Condon Overlap of the Vibrational States 0(Blue),1(Red) on the B state, and 0-29 on the X state is depicted on the bottom for the respective displacement.

the condition set forth by Equation 5.4 to sum to unity over i states as depicted by the transition probabilities at the bottom of Figure 5.19. That is, the B wavepacket projects onto fewer vibrations on the C potential. For ideal reproduction of the spatiotemporal dynamics in spectrum, the probe pulse should be resonant with the vibrations that have the highest Franck Condon factors, or in this case, the frequency associated with the peak projection of the $|0>$ wavefunction from B (v=13 on the C state for $x_\delta = 4.0$). The number of vibrational states on the C state is comparable to the dynamic resolution on which the $|0><1|$ superposition is projected on; ss the displacement becomes smaller, the dynamic range of the spatiotemporal dynamics becomes more restricted in the spectrum due to overlap with fewer vibrations on C. (see displacement of 0.5 case in Figure 5.19).

For a fixed displacement, the probe pulse is scanned in energy for selective representation of the superposition in the signal. For a displacement of 4.0, if the probe pulse is tuned to be resonant with the 13th vibration on the C state, corresponding to an energy of 16500 $cm^{-}1$, the spatiotemporal dynamics of the superposition are reproduced in good fidelity subject to the distortion of the FC projection of the superposition (see inset of Figure 5.4). If the Probe is detuned to be resonant with the 9th vibration on the C state, corresponding to an energy of 16000 $cm^{-}1$, the projection of the B wavepacket onto the lower energy vibrations on the C state is more pronounced (see displacement of 4.0 in Figure 5.19). This is akin to seeing the spatiotemporal dynamics, windowed near a turning point as opposed to seeing the full dynamics. The opposite case also applies.

So far, the simulation has considered identical harmonic potentials for the B and C states, both with a fundamental vibrational frequency of 100 $cm^{-}1$. In Figure 5.20, The time dependent spectrum is considered in a case where the fundamental vibrational frequency of the C state is reduced by 10 % to 90 $cm^{-}1$. In this case, the curvature of the C state is shallower than the B state, due to the force constant on the potential, $k = \mu\omega^2$ being reduced as a result. The $|0><1|$ superposition on the B state will now overlap with fewer vibrational eigenstates on the C state. This is evident in the Franck Condon overlaps between the vibrations on both states at the bottom of Figure 5.20. In the case where both B and C had identical curvatures, the projection of the wavepacket from the B to the C state for $x_\delta = 6.0$ was incomplete with a portion of the projection being omitted (see Bottom Right of Figure 5.19). With a softer curvature on the C state, the spectral map is more compressed. The lower vibrational spacing means that as the superposition is projected across an energy region of 2700 cm^{-1} as opposed to the previous 3000 cm^{-1}. Upon comparing the time dependent spectra in Figure 5.19, and Figure 5.20, the latter shows a redshift of the spectral dynamics with a smaller spread in energy between the wavepacket oscillations analogous to the lowered harmonic frequency. The effect of "compressed" Franck Condon overlaps and spectral dynamics is made more dramatic for illustrative purposes in Figure 5.21, where the

energy spacing of the vibrations on the C state is reduced to 60 cm^{-1}.

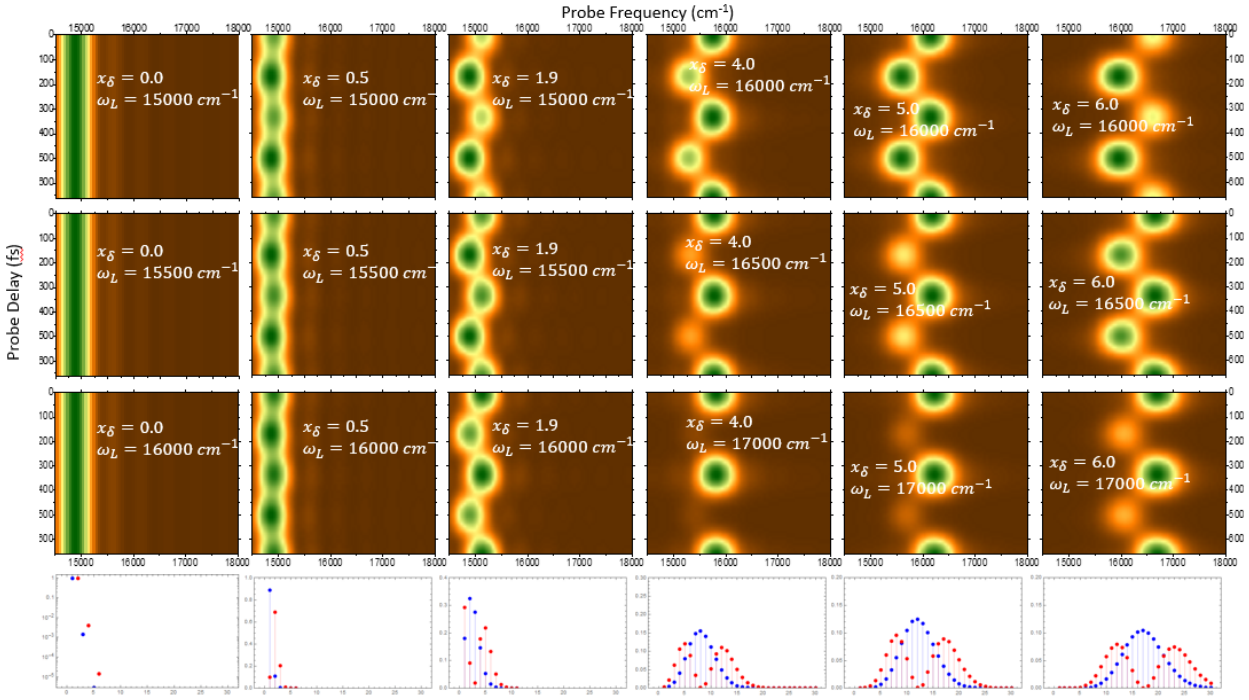

Figure 5.20: $S(\tau, \omega)$ from Equation 5.16 with a reduced electronic potential force constant, illustrated for x_δ=0, 0.5, 1.9, 4.0, 5.0, and 6.0, for Probe Energies E_L=15000 cm^-1, 15500 cm^-1, 16000 cm^-1 for the cases with small displacement (0,0.5,1.9) and 16000 cm^-1, 16500 cm^-1, 17000 cm^-1 for the larger displacements 4.0, 5.0, and 6.0. The Franck Condon Overlap of the Vibrational States 0(Blue),1(Red) on the B state, and 0-29 on the X state is depicted on the bottom for the respective displacement.

In addition to having the proper E_L for a given x_δ, the pulse width of the probe and the vibrational dissipation time on the C state, over which the wavepacket is probed, must also be considered. Changing the pulse-width of the probe pulse is akin to changing the width of the Kerr gate in the previous section. The probe pulse width determines the discreteness of the phase at which the B wavepacket is projected onto the C state. If the length is short, relative to the period of motion of the B vibrations, then the spatiotemporal dynamics are captured at very well defined phases, where the wavepacket doesn't have the opportunity to evolve under the action of the probe pulse. As the pulse width is increased and approaches an appreciable fraction of the period of wavepacket motion, the phase of the projection onto the C state becomes smeared. If the pulse width is longer than the period of motion, then

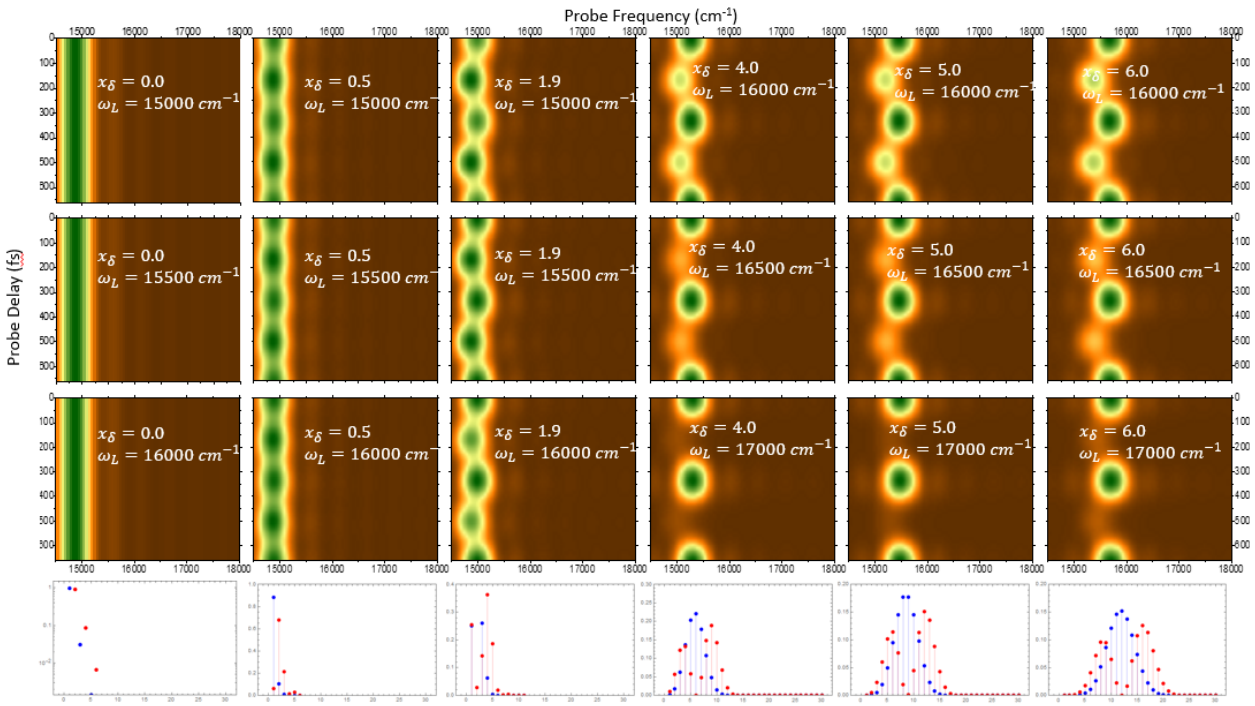

Figure 5.21: $S(\tau, \omega)$ from Equation 5.16 with a reduced electronic potential force constant, illustrated for x_δ=0, 0.5, 1.9, 4.0, 5.0, and 6.0, for Probe Energies E_L=15000 cm^-1, 15500 cm^-1, 16000 cm^-1 for the cases with small displacement (0,0.5,1.9) and 16000 cm^-1, 16500 cm^-1, 17000 cm^-1 for the larger displacements 4.0, 5.0, and 6.0. The Franck Condon Overlap of the Vibrational States 0(Blue),1(Red) on the B state, and 0-29 on the X state is depicted on the bottom for the respective displacement.

the dynamics projected onto the C state appear static in time, and as the probe pulse is preparing the vibrations during 1 cycle of motion. The effect of probe pulse-width on the capturing the discrete phase of the motion is illustrated in Figures 5.8-5.14 where the probe pulse width is varied from 5 fs to 200 fs. Naturally if the probe pulse width is changed to 333 fs, the period of wavepacket motion, the time dependent spectrum will lose time dependence.

The electronic dephasing time plays a role in determining the fidelity of the spatiotemporal dynamics reproduced in spectrum. It has been established that in order to reproduce the spatiotemporal dynamics in spectrum with the best possible fidelity, the probe pulse should be as short as possible. This will allow simultaneous preparation of a manifold of vibrations on the C state, while also capturing the wavepacket motion on the B state in at very discretely

defined phases. For a pulse width of $\Delta t = 5$ fs, the effect of the vibrational relaxation time is depicted in Figure 5.22 for spectra obtained at the $\pi/2$ phase of motion for $1/\Gamma = 10$, 25, 50, 100, and 200 fs on the C state. As the dephasing time is increased, the finer spatiotemporal features emerge in the spectral plots. For comparison, the spatiotemporal dynamics at the defined phases, as well as the Franck Condon projections from the wavepacket to the C state vibrations are included on the left pane of the Figure. The vibrational relaxation time is the inverse of the vibrational line width. The shorter the relaxation time the wider the linewidth in spectrum. The measured (or simulated) spectrum can be thought of as the sum of the emission contributions from each respective vibration on the C state emitting to the B state wavepacket. If the relaxation time is short, and thus the linewidth of the C vibrations broad, the spatiotemporal dynamics are washed out in the broad spectral emission from each vibration on the C state. If the relaxation time is long and the linewidth narrow, then the spatiotemporal dynamics are best reproduced in the time resolved spectrum. However in some cases the longer the vibrational relaxation time isn't necessarily the better. The C state vibrations have their own vibrational period which one would prefer the dissipation time to stay under. However, having a vibrational dissipation time that is longer than the period of vibrational motion will introduce interference in the spectrum. This intereference is physically explained as the reemission of the C state wavepacket. This interference can be numerically Fourier filtered.

Assuming, as in the present case, a harmonic potential, the period of motion on the C state is the same for all vibrational eigenstates. If the wavepacket from the B state is projected onto the C state at some probe delay time, and the emitted spectrum from the C state due to the created third order polarization is measured as a function of the vibrational dissipation time, as the dissipation time approaches the period of motion for the C state vibrations, reemission will occur and introduce interference into the measured spectrum. The Fourier Transform of the spectrum containing the interference will reveal a decay at early time corresponding to the observed spectrum in absence of the interference, and a recurrence at

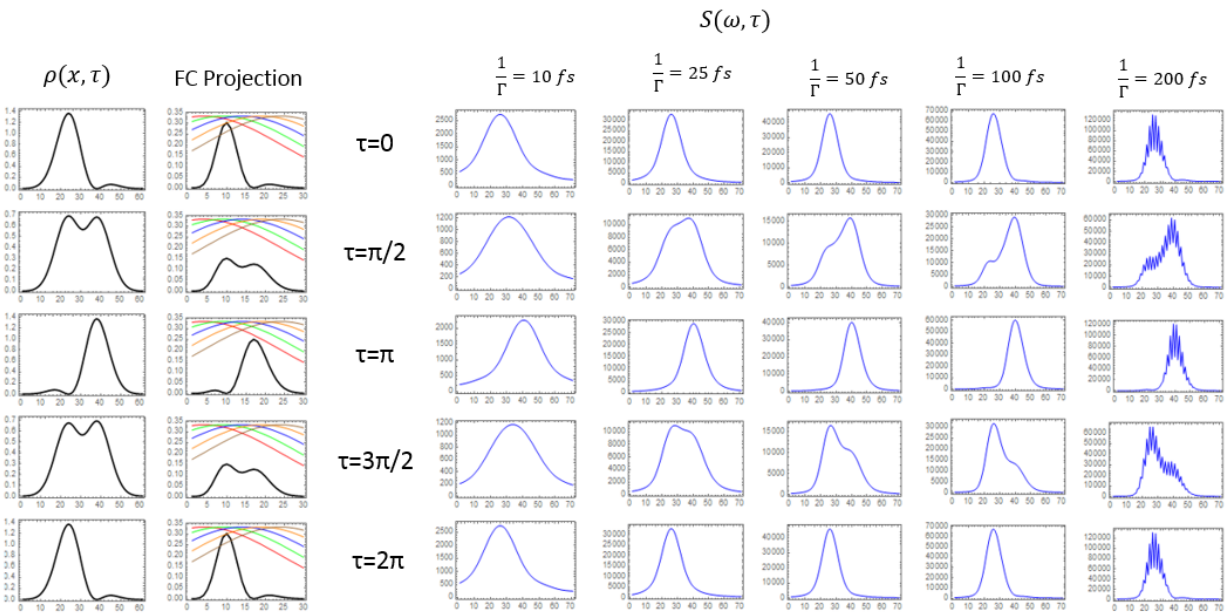

Figure 5.22: $S(\tau,\omega)$ at various vibrational dissipation times on the C state. The spectra are calculated for defined phases of the spatiotemporal dynamics, probed with a pulse resonant with the B to C state transition having a pulse width of $\Delta t = 5$ fs. The spectral overlap of the probe pulse with the vibrational states on the C state is depicted under the "Franck-Condon" Label as the Blue Trace. For comparison of the spectral reproduction of the spatiotemporal dynamics, the density, $\rho_{01}(x,\tau)$ is depicted at corresponding phases on the left.

some time corresponding to the inverse of the period of the interference in the measured spectrum. This recursion is the period of motion for the vibrations on the C state. In this example, used to depict the dependence of the measured spectrum on the pulse width and the dissipation time, the potential energy surfaces B and C are harmonic with the same vibrational energy spacing. Thus the period of motion for vibrations on both states is the inverse of 100 cm^{-1} or T = 333.3 fs. In the case of the vibrational dissipation time of 200 fs in Figure 5.22, the spectrum was generated by Fourier transforming for a time period of twice the dissipation time(or 400 fs). This is approximately 1.3x the period of motion and so the spectral interference associated with reemission from the C state is present. This spectrum is sampled in increments of 50 cm^{-1}, so to illustrate the Fourier Transform of this spectrum revealing the reemission time, and thus the vibrational periods on the excited state,

a spectrum with a finer increment is obtained in Figure 5.23 with the accompanying Fourier Transform depicting the reemission time of 333.3 fs. Of course, if in reality, a spectrum is obtained that has such interference and is hence harder to use to depict the spatiotemporal dynamics, the spectrum can be Fourier filtered to minimize anything in the spectrum with a "reemission time" greater than (in this case) 333.34 fs.

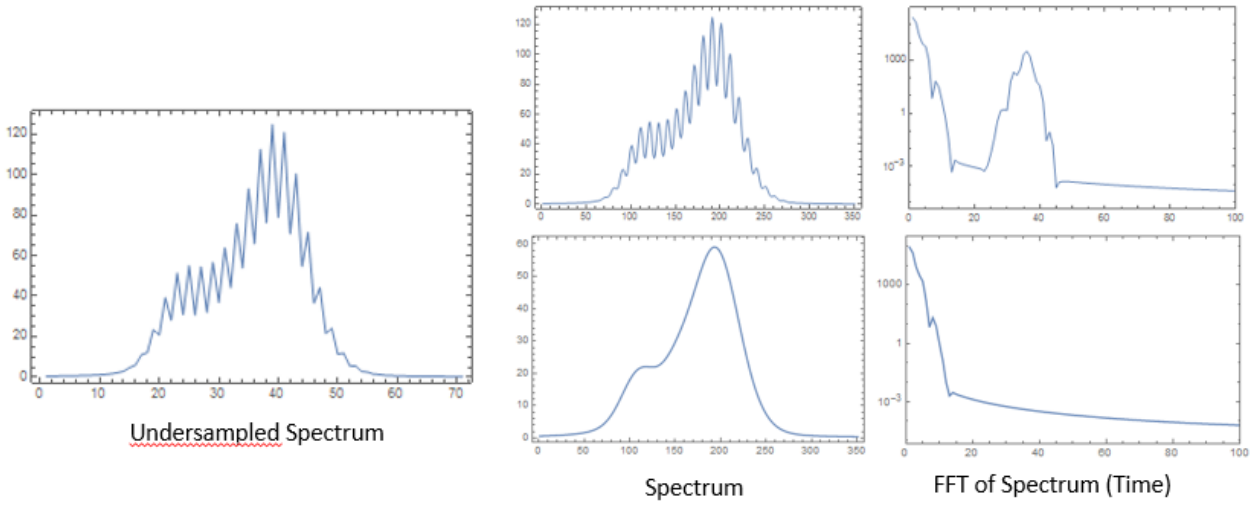

Figure 5.23: $S(\tau, \omega)$ for a signal obtained by integrating longer than the vibrational period. The result is a spectrum with modulations (left pane). These modulations are undersampled and recreated with higher fidelity (middle, top). The Fourier Transform(right, top) of the Spectrum reveals the reemission time of 333 fs, analogous to the period of motion. If the Fourier Transform is filtered to clean the reemission(right, bottom), the Inverse transform reveals a spectrum in absence of the modulations (middle, bottom)

Given the right potential energy surfaces, proper conditions for FC overlap, the appropriate pump pulses to prepare two(or more) vibrational states and the appropriate probe pulse, to probe over a large number of vibrations on a higher excited state (given the appropriate displacement), the spatiotemporal dynamics of a $|0><1|$ vibrational superposition can be reproduced as spectral modulations in time via SRTG.

5.4 Wigner Distribution Function

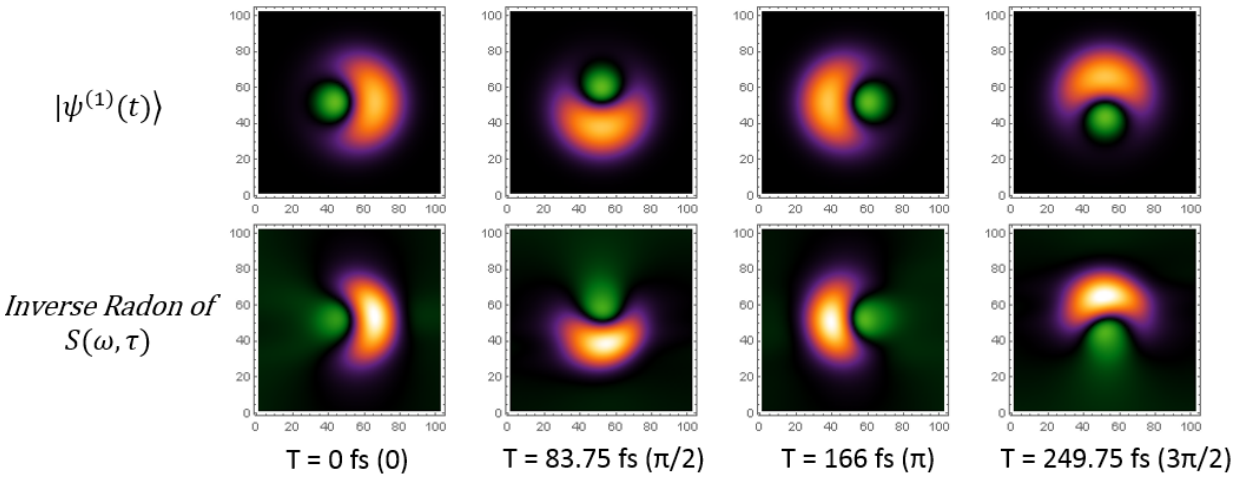

Figure 5.24: The Wigner distribution functions for the B state wavepacket obtained by Wigner transform (top series) and Inverse Radon Transform of the measured density via SRTG (bottom series) at select phases during the motion.

The Inverse Radon Transform(IRT) allows for reconstruction of the WDF from the measured spectral density. The reconstructed WDF from the measured spectrum is depicted in the bottom series of Figure 5.24. The reconstructed WDF is compared to the WDF of the wavepacket, given on the top series of the figure. The latter is directly constructed from the wavepacket via the Wigner Transform;

$$W(x,p,t) = \int \psi^*_{B,01}(x+\frac{s}{2},t)\psi_{B,01}(x-\frac{s}{2},t)ds \tag{5.17}$$

where $\psi_{B,01}(x,t)$ is the superposition on the B state;

$$\psi_{B,01}(x,t) = \psi_0(x)e^{-\imath E_0 t} + \psi_1(x)e^{-\imath E_1 t} \tag{5.18}$$

We also consider the WDF of the C state packet, launched by the probe pulse at $t = \tau$, by

taking the Wigner Transform of the packet;

$$\psi_{C,0-29}(x,t) = \sum_{i=0}^{29} \psi_{C,i}(x) e^{-\imath E_i(t-\tau)-\Gamma t} \int \psi^*_{C,i}(x,t2)\mu E(\tau)\psi_{B,01}(x,t2)dxdt_2 \tag{5.19}$$

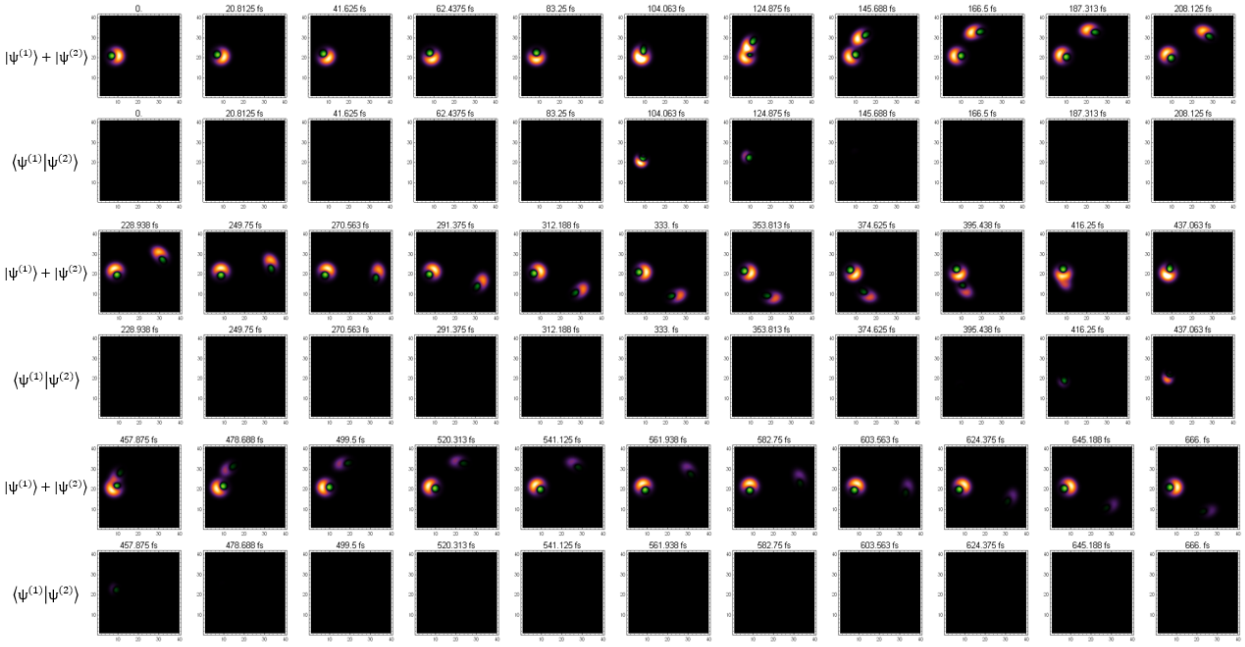

Figure 5.25: The WDF for $|\psi^{(1)}_{B,01}(x,p,t)>$ as it evolves over two periods of motion. Each frame is 20 fs of evolution. at 100 fs a probe pulse acts on the $\psi^{(1)}_{B,01}$ state and creates a $|\psi^{(2)}_{C,0-29}(x,p,t)>$ wavepacket. We also show the phase space overlap of the two packets $<\psi^{(1)}_{B,01}(x,p,t)|\psi^{(2)}_{C,0-29}(x,p,t)>$. The period of both wavepackets is 333 fs. A recurrence in overlap occurs when both packets complete one period of motion. The dephasing between the B and C states is assumed to be 500 fs.

For identical harmonic potentials with $\omega = 100\ cm^{-1}$, $x_\delta = 5$, $\Delta t = 10$ fs and ω_L resonant with the separation between the B wavepacket and 29 vibrations on the C state, the evolution of both $\psi_{C,0-29}$ and $\psi_{B,01}$ is depicted on the left pane of Figure 5.25. In absence of the probe pulse, the first few images depict the evolution of $\psi_{B,01}$. At 100 fs, the Probe pulse creates the C state packet. The ψ_C wavepacket continues its' evolution and returns to overlap with the B packet after one period of motion (in this sequence 433 fs). This action cannot be directly

measured by SRTG. SRTG in this case, integrates over the action of the C wavepacket at every probe delay. If the C wavepacket dissipates before it can complete one cycle of motion, the measured spectrum is simply the density of the B wavepacket. If the C wavepacket lives longer than the period of motion, reemission will occur in the measured SRTG spectrum.

5.5 Distortions in the WDF

While the reproduction of the WDF from the density bears immaculate resemblance to the WDF recovered from the wavefunctions, it is subject to various distortions. The curvature of the potential, $\frac{\partial V(x)}{\partial x}$ determines how wide the B packet density is spread This is depicted for various curvatures of the C state in Figures 5.19-5.21.

Consider two potentials C and B with force constants a and b respectively, displaced in space by d. The difference between these potentials in energy;

$$V_{C-B}(x) = ax^2 - b(x-d)^2 = (a-b)x^2 - bd^2 + 2bdx \tag{5.20}$$

The derivative of the difference with respect to x, i.e. the difference in curvatures;

$$\frac{\partial V_{C-B}(x)}{\partial x} = 2(a-b)x + 2bd \tag{5.21}$$

The intercept, $2bd$, is just a shift, and the slope $2(a-b)$ the difference in force constants of the two potentials, determines the spectral range with which the spectral density projects. If $a > b$, the C potential, on which the B wavepacket is projected to, has a higher force constant and is steeper, meaning the energy spacing between adjacent vibrational states is larger and the spectral range is larger. The opposite trend is also true. It is therefore intuitively obvious that for a finite probe pulsewidth, and therefore a finite bandwidth, a

softer force constant, or otherwise a situation where $b \geq a$ is preferred. In this case, there are likely to be more accessible vibrational states on the C state within the bandwidth of the probe pulse. For finite pulsewidths ranging from 5-100 fs, the projection of $\psi_B^{(1)}(t)$ onto $\psi_C^{(2)}(t)$ is depicted in Figure 5.26

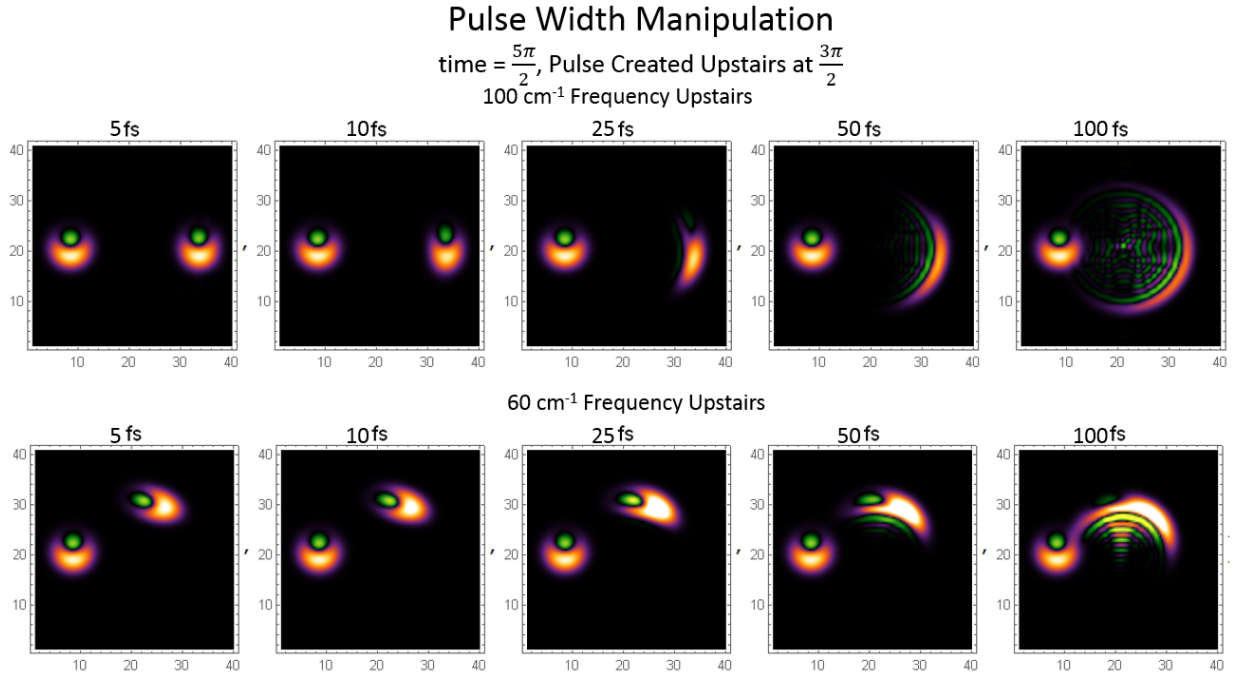

Figure 5.26: The WDF for $|\psi_{B,01}^{(1)}(x,p,t)>$ is depicted on the left of each snapshot at a phase of $5\pi/2$. $|\psi_{C,0-29}^{(2)}(x,p,t)>$ was created in the image of $|\psi_{B,01}^{(1)}(x,p,t)>$ when the latter was at a phase of $3\pi/2$. The top row is snapshots for when the vibrational period on the C state is 100 cm^{-1} and the bottom is for a vibrational period on the C state of 60 cm^{-1}. Particularly in the case of a 25 fs pulse width (middle, top and bottom) the C state with a longer period of motion (60 cm^{-1}, bottom) reproduces the B state wavepacket with more fidelity than the C state with a shorter period of motion (100 cm^{-1}, top)

In the case of a 25 fs probe pulse (middle) the C state with 60 cm^{-1} vibrational eigenstate spacing reproduces the B state wavepacket better than the C state with the 100 cm^{-1}.

There is a finite tradeoff concerning ω_C and ω_B. As illustrated above, $\omega_C < \omega_B$ allows for a better represenation of the B wavepacket on the C state, however if $\omega_C <<< \omega_B$ The B

wavepacket evolves under the creation of of the C wavepacket, provided a sufficiently long pulsewidth, and the projection onto the C state is smeared and appears isotropic. The longer period of motion affords the luxury of better spectral resolution in the measurement, provided there is a longer dissipation time to match (see Figure 5.22). The longer dissipation time, in absence of the reemission due to recursion, which is determined by the period of motion on the state, provides a higher degree of fidelity of wavepacket spatiotemporal dynamics. In the opposite case, $\omega_C >> \omega_B$, The C state wavepacket is smeared during creation by the probe pulse.

In regards to comparing the Wigner Transformed wavepacket to the density obtained wavepacket, if the WDF is obtained via an IRT, then the WDF does not represent an "instantaneneous" snapshot of the density in time. The IRT requires density evolution over π period of motion in order to reconstruct the WDF. A trivial comparison of the density derived Wigner and its wavepacket derived counterpart can be made by subtracting one from the other, assuming both have been normalized.

The WDFs, derived from the spectral density using IRT and from the wavepacket derived via Wigner Transform are shown in Figure 5.27. The WDFs of the wavepacket at t = 0, $\frac{\pi}{2}$, π, and $\frac{3\pi}{2}$ are depicted in the middle column. The WDFs for the same phases derived from the density are depicted on either side, right for a C state with a 100 cm^{-1} vibrational frequency and left for a C state with 60 cm^{-1}. After normalization and multiplication by a common multiplier, the residual difference between the WDFs derived from the wavepacket and the density are shown further on either side for the appropriate conditions. On the very right and left is a comparison of the wavepacket and the density derived profiles integrated over all momentum. In this case, the probe pulse that created the higher lying excited state wavepacket was 10 fs long and the vibrational cooling time on the C state is 50 fs. For these conditions, the WDF is better reproduced when the C state has 100 cm^{-1} vibrational spacing. However in the same set of WDFs created by a 25 fs probe pulse and 100 fs

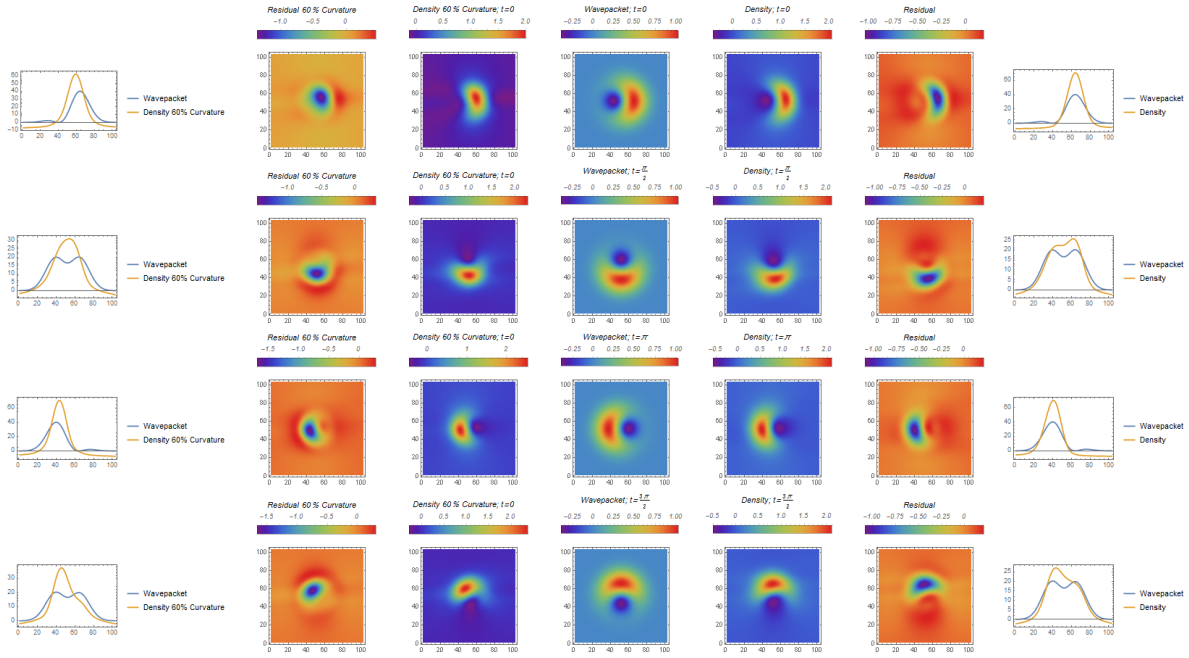

Figure 5.27: The WDFs obtained from a Wigner Transform (middle) of the wavepacket compared to the WDF obtained by IRT of the spectral density when the wavepacket is projected onto a potential with 100 cm^{-1}(middle right) and 60 cm^{-1}(middle left) vibrational frequencies, using a 10 fs pulse and 50 fs vibrational dissipation time at t = 0, $\frac{\pi}{2}$, π, and $\frac{3\pi}{2}$. The residual WDFs of both cases(far left and far right) is the difference between the IRT derived WDF and the Wigner Transform WDF. Farther right and left is a comparison of the wavepacket and the density WDFs integrated over the momentum.

vibrational cooling time depicted in Figure 5.28, the opposite is true. The lower energy vibrational frequency potential has a better reproduction of the WDF with a vibrational cooling time of 100 fs than with 50 fs as evidenced by the emergence of spectral features in the momentum integrated plots. The pulse width for the 60 cm^{-1} potential makes little difference, as all the vibrations on the C state are still prepared, even with a lower pulse bandwidth. The higher vibrational energy potential WDF suffers due to a longer pulsewidth, and hence a lower bandwidth, which prepared fewer vibrations on the C state. The longer pulse width and dissipation time, in the absence of smearing, is better suited for a potential with a lower energy vibrational frequency, while a shorter pulsewidth is better suited for a

potential with a higher vibrational frequency.

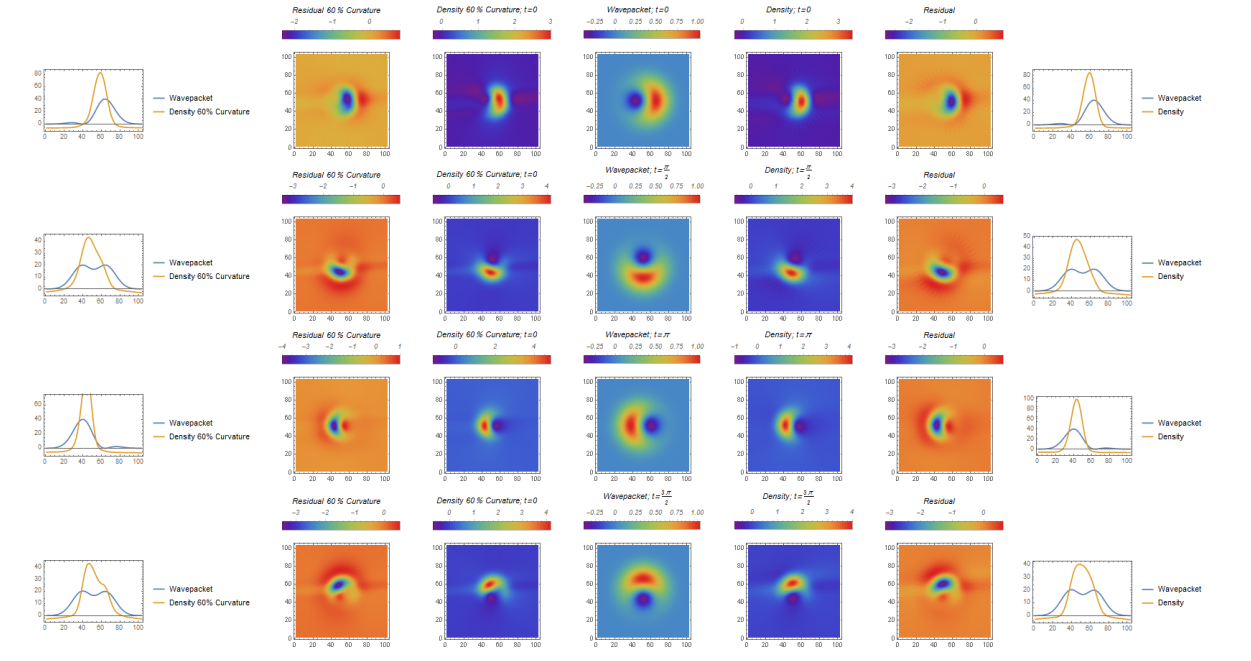

Figure 5.28: The WDFs obtained from a Wigner Transform (middle) of the wavepacket compared to the WDF obtained by IRT of the spectral density when the wavepacket is projected onto a potential with 100 cm^{-1}(middle right) and 60 cm^{-1}(middle left) vibrational frequencies, using a 25 fs pulse and 100 fs vibrational dissipation time at t = 0, $\frac{\pi}{2}$, π, and $\frac{3\pi}{2}$. The residual WDFs of both cases(far left and far right) is the difference between the IRT derived WDF and the Wigner Transform WDF. Farther right and left is a comparison of the wavepacket and the density WDFs integrated over the momentum.

5.6 Fluctuations of the Wigner Hole

One of the metrics for measuring the fidelity of WDF reproduction when comparing a density source or a wavepacket source is the magnitude, or the "depth" of the Wigner Hole. This hole is a moniker for the negative region of the WDF, the fundamental proof that the WDF contains the quantum description of the state being described. When considering the magnitude of the hole of an evolving WDF, if the WDF was retrieved from a wavepacket

via Wigner Transform, the magnitude is time independent. Whereas, if the WDF is generated from a measurement, such as the time dependent spectrum being simulated here, the hole is seen to fluctuate with a period proportional to the period of motion of the state being described. The difference is highlighted in Figure 5.29. The fluctuation is clearly a measurement artifact.

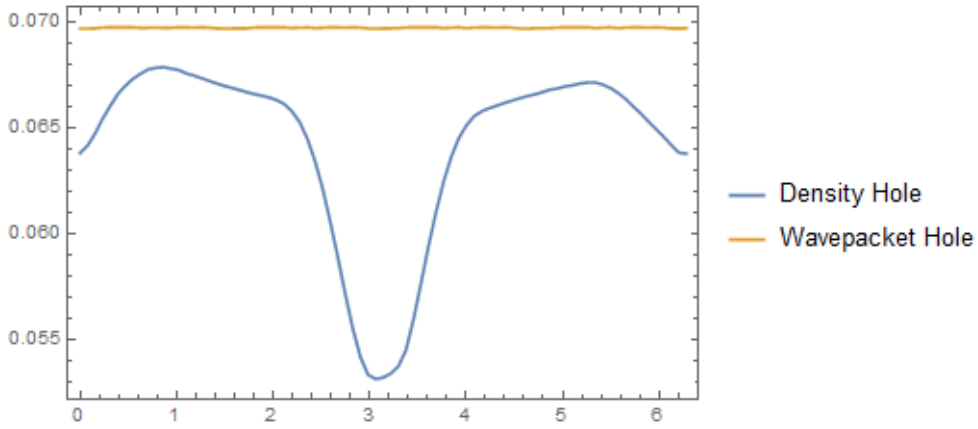

Figure 5.29: The size of the negative region was calculated for WDFs obtained from tr-spectrum via IRT (Blue), and from the wavepacket via Wigner Transform (Orange) as a function of one period of motion of the original evolving superposition (0 to 2π, x-axis). The hole size fluctuates in the density derived WDF due to the angular convolution between the original and created state overlap. The features observed over one cycle of motion repeat for every 2π of evolution

To obtain the magnitude of the hole, the integral of all the values of a WDF is subtracted from the integral of the absolute value of the WDF to give a magnitude that is twice the size of the hole;

$$Hole(t) = \frac{\int\int |W(p,q,t)| dpdq - \int\int W(p,q,t) dpdq}{2} \tag{5.22}$$

The fluctuations of the hole magnitude, derived from the density WDF, as a function of time arise from the mismatch of the original and created wavepackets. The created wavepacket is always produced by the probe pulse at a turning point on the higher energy potential. However, the original state, can be cloned via the probe pulse at any time. Hence the

fluctuations result from the angular convolution of the original state at any phase and created state, always at a turning point, while it is being created by the probe pulse. The important consideration is that the measurement can only reduce the hole. This provides a robust optimization principle for measurements with shaped pulses; namely, adjustment of pulse width, detuning, and chirp to maximize the hole, and in the process, to obtain the highest fidelity in the state reconstruction.

5.7 Generalizing the experimental requirements

Numerical simulations have shown the effect of ideal and far from ideal parameters of the probe pulse width, detuning, the curvatures and displacements of the two electronic potentials, and the vibrational dissipation time on the higher lying excited state. It is more helpful to reduce the findings in terms of scaled parameters, to generalize the principles for state reconstruction. Indeed, the considerations are limited to the reconstruction of the WDF of a harmonic oscillator, which is a good approximation if low lying vibrational superpositions are interrogated.

We consider the vibrational period of the lower excited state, on which the $|0><1|$ coherence is created to have a vibrational frequency of ω' and the higher lying excited state to have a vibrational frequency of ω''. An exact copy of the state is created on the upper electronic state using a delta probe pulse. However, if the emission is limited to the decay of the overlap between the created state and the original, this time must be long enough to define the structure of the packet in its spectral map. The length of the overlap is determined by the angular frequency of the created state WDF and the phase angle spanned by the original state WDF on the created state potential. The latter is determined by the delta shift, x_δ, between potential minima.

In the case where the vibrational dephasing time on the created state is long, or longer than the period of motion of the vibrational frequency ω'', reemission signatures in the form of spectral interference will emerge in the time dependent spectrum. In the case where wavepacket is projected onto a dissociative(unbound) potential energy surface, the measure spectral fluctuations will only be observed under the temporal evolution of the probe pulse. As described earlier in the case where the dephasing time is less than one period of motion on the created state.

The effect of a finite probe pulse is the smearing seen in Figure 5.26, which arises from the angular convolution between the original state and the created state. Since the emission is limited to the vertical overlap of the state and its copy, this has the effect of angular autocorrelation of the WDF, as long as the evolving excited state moves out of overlap and the emission is restricted by dephasing to be instantaneous, i.e., as long as dephasing time is shorter than the excited state period;

$$\frac{1}{\Gamma} < \frac{2\pi}{\omega''} \tag{5.23}$$

We see for potentials shifted by $x_\delta = 5$, that a pulsewidth of;

$$\Delta t = 0.1\frac{1}{\Gamma} = 0.1 * \frac{2\pi}{\omega''} \tag{5.24}$$

is necessary to restrict the distortion. As we show below, this is determined by the relative displacement of the potentials. Much longer pulsewidths can be used for the same potentials if their displacement is smaller. A more critical requirement on the probe pulsewidth is placed by its time-bandwidth product; the probe bandwidth must span the entire Franck-Condon window defined by the relative curvatures of the two electronic states. The classical reflection approximation is adequate to define this requirement for the relative curvature

between two states;

$$\Delta x \frac{\partial \Delta V(x)}{\partial x} = \Delta E \tag{5.25}$$

the energy bandwidth of the probe ($\frac{\Delta E}{\hbar}$ is the spectral bandwidth), where Δx is the spatial span of the lower energy wavepacket (defined by the original state curvature, or equivalently the original state frequency) and $\Delta V(x)$ is the difference between the lower and higher energy excited state potentials;

$$\Delta V(x) = \frac{1}{2}k'x^2 - \frac{1}{2}k''(x-\delta)^2 \tag{5.26}$$

k' and k'' are the force constants of the lower and higher energy potential energy surfaces with the higher energy minimum shifted by δ. Further simplification yields;

$$\Delta V(x) = \frac{1}{2}(k'-k'')x^2 + k''x\delta - \frac{1}{2}k''\delta^2 \tag{5.27}$$

The derivative of the difference yields the transformation function between spatial and spectral coordinates;

$$\frac{\partial \Delta V(x)}{\partial x} = (k'-k'')x + k''\delta \tag{5.28}$$

If the curvatures of the two potentials are not equal $k' \neq k''$ then there is a quadratic difference in curvatures, which will cause distortion of the $|0><1|$ coherence at one of the turning points, and compress it at the other. This can be overcome by using a shaped probe pulse that passes through a spatial light modulator (SLM). If a spectrum is collected over π phase of evolution in SRTG, and passed through an Inverse Radon Transform, a WDF can be generated using an unperturbed probe pulse. The SLM can be iteratively optimized to increase the size of the negative region of the WDF. When the negative region of the WDF

is optimized, the amplitude profile of the pulse shaped by the SLM reveals the curvature of the difference in potentials $\Delta V(x)$.

If the curvatures are the same, i.e., if $\omega' = \omega''$ then $k' = k''$ and the first term in Equation 5.26 is 0, and the difference potential is linear, with a slope of $k''\delta$. The significance of this is that the space to frequency mapping is true, with a scaling determined by $k'' = \mu\omega''^2$, and δ. Therefore, as the displacement between the two potentials is increased, the FC window is expanded along the frequency axis.

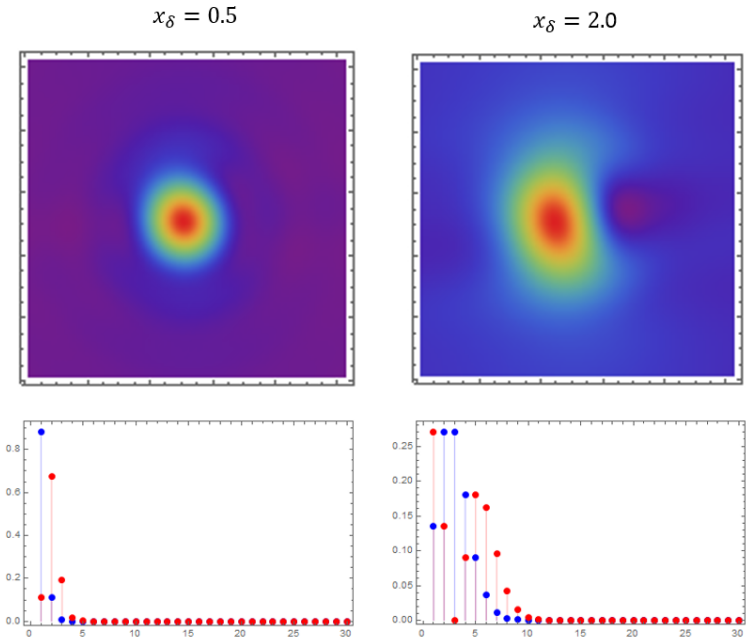

Figure 5.30: The WDFs obtained from IRT of the spectral density when $x_\delta = 0.5$ (left) and 2.0 (right). The potentials have identical curvature. The probe pulse used to generate the density is 10 fs long, and the excited state has a dephasing time of 100 fs. The probe pulse is detuned such that the time dependent density is even in height on both turning points to guarantee best WDF reconstruction. Below the WDF is the FC projection from the original vibrations (blue (v=0) and red (v=1) and the created vibrations (x-axis v=0-29). The WDF for the larger displacement contains a Wigner Hole, whereas the smaller displacement does not

Because the spacing in the models studied above focused largely on $x_\delta = 5.0$ the bandwidth

of at 10 fs laser pulse was required to observe the full spread of the $|0><1|$ coherence. Effectively, the above argument means that for a lower x_δ, less bandwidth is required to see the full spread of the wavepacket. This beckons the question of what is the bare minimum displacement that can be used in order to observe a negative region in the WDF? If we consider the WDF constructed from the earlier sequence of tr-spectra for identical potentials from Figure 5.19 obtained by varying the displacement between the two potentials, we see in Figure 5.30 that for a displacement of $x_\delta = 0.5$ between the two minima, no hole can be observed (left side). Whereas for a displacement of $x_\delta = 2.0$ the WDF contains a negative region(right side). A closer inspection of the FC projections, reproduced below the WDF for each displacement show that the WDF with a larger displacement retains the valley between the two peaks for the projection of $\psi_{B,v=1}$ (Red points), whereas the projection of the smaller displacement has no such distinction. This projection, along with the $\psi_{B,v=0}$ are the time dependent probability distributions that we see manifest in the time resolved spectra. The significance of the two alternatively fluctuating peaks in time are the nascence of quantum behavior as it shows that the wavepacket is neither in one side of the distribution nor the other, but in both simultaneously. Therefore, if the distinction between being in on both sides of the distribution is not present in the FC projections, as is the case in the with the smaller displacement, then the WDF will not have in it a negative region.

The minimum amount of states necessary to depict the projection of two peaks and a valley of $\psi_{B,v=1}$ is three, two for the peaks and one for the valley. The FC projection, along with the density derived WDF appears in Figure 5.31 on the left. We see that for a two state superposition on the lower energy excited state, projected onto three states on a higher energy excited state, at a displacement of $x_\delta = \sqrt{2ln2}$, the half-width at half-max of the $\psi_{B,v=0}$ wavefunction, the projection of $\psi_{B,v=1}$ onto $\psi_{C,v=1}$ is lower than its projection onto $\psi_{C,v=0}$ and $\psi_{C,v=2}$. Accordingly, the generated WDF displays a negative region. As per the argument made before that the probe pulse must have the bandwidth to span the states created on the higher lying excited state, because the number of states in this case is 3, the

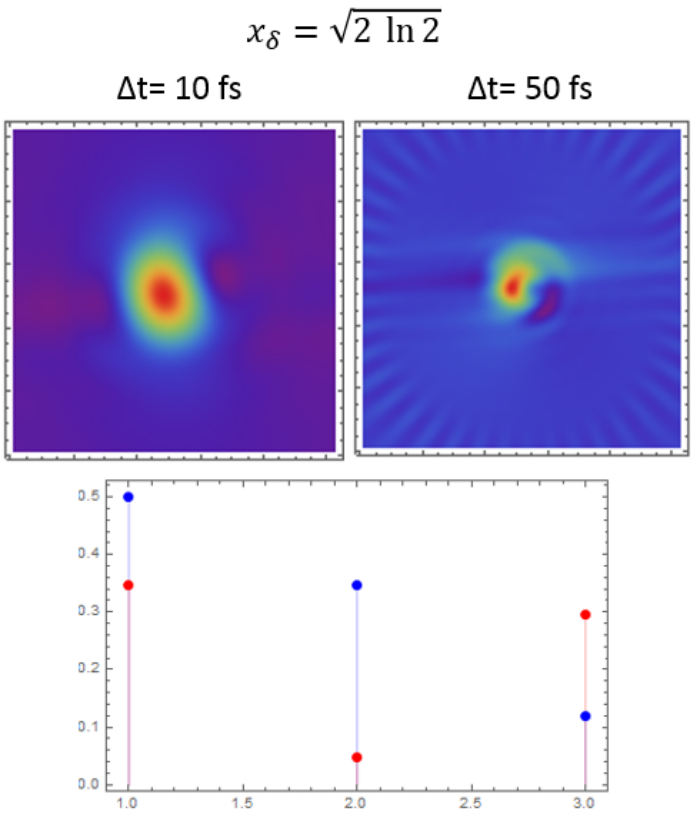

Figure 5.31: The WDFs obtained from IRT of the spectral density when $x_\delta = \sqrt{2Ln2}$. The potentials have identical curvature. The probe pulse used to generate the density is 10 fs(left) and 50 fs(right) long, and the excited state has a dephasing time of 100 fs. The probe pulse is detuned such that the time dependent density is even in height on both turning points to guarantee best WDF reconstruction. Below the WDF is the FC projection from the original vibrations (blue (v=0) and red (v=1) and the created vibrations (x-axis v=0-2). The WDF for both probe pulse durations contains a Wigner Hole. The tails or the yin-yang behavior is generated as a result of evolution of the original wavepacket under the probe pulse.

span of the probe pulse need only to be 200 cm^{-1}, much less than the bandwidth of a 10 fs pulse used earlier.

The same system, two vibrations projected onto three, with a displacement of a half-width half-max of the $\psi_{B,v=0}$ wavefunction, but measured with a 50 fs appears in Figure 5.31 on the right. The 50 fs probe pulse is not centered on the transition between $\psi_{C,v=0,1}$ and

$\psi_{C,v=1}$ but is slightly shifted, to give either side of the valley equal weight. This is because the FC projection depicted in the figure shows that the overlap of $\psi_{B,v=1}$ is better with $\psi_{C,v=0}$ than it is with $\psi_{C,v=2}$. If the probe pulse is slightly shifted relative to the center of the projection, it can be set such that the tr-spectrum will give either turning point equal weight, for better reproduction of the WDF. The WDF generated by the longer probe pulse exhibits the smearing discussed earlier; as the probe pulse is acting on the system, the original state is evolving appreciably and effectively copies $\frac{1}{6}$th of its motion onto the created state. This demonstrates that the optimal experimental conditions can be defined in scaled coordinates of the relative potential shift and curvature to define the ideal probe pulse width and dephasing time.

Bibliography

[1] R. Silbey E. Barkay, Y. Jung. *Ann. Rev. Phys. Chem.*, 55:457–507, 2004.

[2] T. D. Ladd. *Nature*, 464:45–53, 2010.

[3] F. Nori I. Buluta. *Science*, 326:108–111, 2009.

[4] L. Kador W. E. Morner. *Phys. Rev. Lett.*, 62:2535–2538, 1989.

[5] J. Bernard M. Orrit. *Phys. Rev. Lett.*, 65:2716–2719, 1990.

[6] R. J. Chichester E. Betzig. *Science*, 262:1422–1425, 1993.

[7] R. N. Zare S. Nie, D. T. Chiu. *Science*, 266:1018–1021, 1994.

[8] R. Rigler M. Eigen. *Proc. Natl. Acad. Sci.*, 91:5740–5747, 1994.

[9] N. F. van Hulst R. Hildner, D. Brinks. *Nature Physics*, 7:172–177, 2011.

[10] F. D. Stefani N. F. van Hulst D. Brinks, R. Hindler. *Farad. Disc.*, 153:51–60, 2011.

[11] D. Brinks et al. *Nature*, 465:905–908, 2010.

[12] F. D. Stefani N. F. van Hulst R. Hindler, D. Brinks. *Phys. Chem. Chem. Phys.*, 13: 1888–1894, 2011.

[13] N.G. Greeneltch R.P.V. Duyne D.L. Polla R.L. Aggarwal, L.W. Farrar. *App Spec*, 67: 2, 2013.

[14] V. A. Apkarian M. Banik, P. Z. El-Khoury. *J. Phys. Chem. C.*, 116:10415–10423, 2012.

[15] A. McQuillan M. Fleischman, P. Hendra. *Chem. Phys. Lett.*, 26:163, 1974.

[16] Prior et al. *J. Chem. Phys.*, 115:8440, 2001.

[17] Prior et al. *J. Chem. Phys.*, 115:236, 2001.

[18] D. Fishman S. Yampolsky. *Nature Photonics*, 8:650, 2014.

[19] W. P. Schleich. *Quantum Optics in Phase Space*. Wiley-VCH, 2001.

[20] T. P. Carter W. E. Morner. *Phys. Rev. Lett.*, 59:2705, 1987.

[21] M. D. Fayer R. W. Olson. *J. Phys. Chem.*, 84:2001, 1980.

[22] D. Mobius M. Orrit, J. Bernard. *Chem. Phys. Lett.*, 156:233, 1989.

[23] M. Orrit F. Kulzer. *Ann. Rev. Phys. Chem.*, 55:585–611, 2004.

[24] V. Palm T. Plakhotnik. *Phys. Rev. Lett.*, 87:183602, 2001.

[25] T. Plakhotnik. *J. Lumin*, 98:57–62, 2002.

[26] A. Hibara T. Sadawa T. Kitamori M. Tokeshi, M. Uchida. *Anal. Chem.*, 73:2112–16, 2001.

[27] J. J. Macklin J. K. Trautman. *Chem. Phys.*, 205:221–229, 1996.

[28] T. D. Harris L. E. Brus J. J. Macklin, J. K. Trautman. *Science*, 272:255–258, 1996.

[29] J. H. Jett J. C. Martin D. C. Nguyen, R. A. Keller. *Anal. Chem.*, 59:2158, 1987.

[30] A. N. Glazer R. A. Mathies K. Peck, L Stryer. *Proc. Natl. Acad. Sci.*, 86:4087, 1989.

[31] L. M. Ramsey W. B. Whitten. *IBID*, 64:2914, 1992.

[32] W. Baumgartner H. J. Gruber H. Schindler T. Schmidt, G. J. Schutz. *Proc. Natl. Acad. Sci.*, 93:2926–2929, 1996.

[33] T. Kues R. Peters U. Kubitschek, O. Kuckmann. *Biophys. J.*, 78:2170–79, 2000.

[34] T. Endress H. Buning M Hallek C. Brauchle G. Seisenberger, M. U. Reid. *Science*, 294:1929–1932, 2001.

[35] W. W. Webb D. Magde, E. Elson. *Phys. Rev. Lett.*, 29:705–708, 2002.

[36] T. Plathotnik A. Mitterdorfer A Renn U. P. Wild F. Guttler, J. Sepiol. *J. Lumin.*, 56: 29–38, 1993.

[37] J. K. Trautman E. Betzig. *Science*, 257:189, 1992.

[38] D. Axelrod E. H. Hellen. *J. Opt. Soc. Am. B*, 4:337, 1987.

[39] W. E. Moerner. *J. Phys. Chem. B*, 106:910–927, 2002.

[40] M. Pirotta A. Renn U. P. Wild T. Plathotnik, D. Walser. *Science*, 271:1703–1705, 1996.

[41] G. R. Holtom M. F. Granville. *J. Chem. Phys.*, 72:467, 1980.

[42] H. Petek et al. *J. Chem. Phys.*, 98:3777, 1993.

[43] L. Kador. *Phys. Status Solid B*, 189:11, 1995.

[44] H. Talon M. Orrit J. Bernard, L. Fleury. *J. Chem. Phys.*, 98:850–859, 1993.

[45] M. Orrit H. Talon T Basche, W. E. Moerner. *Phys. Rev. Lett.*, 69:1516–1519, 1992.

[46] R. J. Silbey Y. J. Jung, E. Barkai. *J. Chem Phys.*, 117:10980–10995, 2002.

[47]

[48] M. Orrit R. Verberk. *J. Chem. Phys.*, 119:2214–2222, 2003.

[49] J. Yu D. A. Vanden Bout P. F. Barbara W. T. Yip, D. Hu. *J. Phys. Chem. A*, 102: 7564–7575, 1998.

[50] L. Kuipers N. F. Van Hulst J. A. Veerman, M. F. Garcia-Parajo. *Phys. Rev. Lett.*, 83: 2155–2158, 1999.

[51] A. Gallagher D. J. Nesbitt M. Kumo, D. P. Fromm H. F. Hamann. *J. Chem. Phys.*, 112:3117–3120, 2000.

[52] C. A. Leatherdale S. A. Empedocles W. K. Woo K. T. Shimizu, R. G. Neuhauser. *Phys. Rev. B*, 63:205316, 2001.

[53] X. S. Xie H. P. Lu. *Nature*, 385:143–146, 1997.

[54] S. Mukamel. *Principles of Nonlinear Spectroscopy.* New York/London: Oxford Univ. Press, 1995.

[55] J. L. Skinner S. A. Egorov, M. D. Stephens. *J. Chem. Phys.*, 107:10485–10491, 1997.

[56] M. Rief X. W. Zhuang. *Curr. Opin. Struct. Biol.*, 13:88–97, 2003.

[57] G. Haran E. Rhoades, E. Gussakovsky. *Proc. Natl. Acad. Sci. USA*, 100:3197–3202, 2003.

[58] D. A. Vanden Bout L. A. Deschenes. *J. Phys. Chem. B*, 105:11978–11985, 2001.

[59] S. Weiss. *Science*, 283:1676–1683, 1999.

[60] X. S. Xie G. K. Schenter, H. P. Lu. *J. Phys. Chem. A*, 103:10477–10488, 1999.

[61] P. W. Anderson. *J. Phys. Soc. Jpn.*, 9:316–39, 1954.

[62] R. Kubo. *Adv. Chem. Phys.*, 15:101–127, 1962.

[63] A. M. Stoneham. *Rev. Mod. Phys.*, 41:82–108, 1969.

[64] S. Weiss. *Science*, 283:1676–1683, 2001.

[65] S. Xie. *Single Molecules*, 2:229–236, 2001.

[66] E. Collini et al. *Nature*, 463:644–647, 2010.

[67] G. Panitchayankoon. *Proc. Natl. Acad. Sci.*, 107:12766–12770, 2010.

[68] G. D. Scholes. *J. Phys. Chem. Lett.*, 1:2–8, 2010.

[69] G. R. Fleming H. Lee, Y. C. Cheng. *Science*, 316:1462–1465, 2007.

[70] G. S. Engel et al. *Nature*, 446:782–786, 2007.

[71] A. H. Zewail. *J. Phys. Chem. A.*, 104:5660–5694, 2000.

[72] H. Rabitz R. J. Levis, G. M. Menkir. *Science*, 292:709–713, 2001.

[73] C. J. Bardeen. *Chem. Phys. Lett.*, 292:709–713, 1997.

[74] N. Dudovich. *Nature*, 418:512–514, 2002.

[75] B. Amstrup. *J. Phys. Chem.*, 95:164–166, 1991.

[76] J. L. Herek. *Nature*, 417:533–535, 2002.

[77] N. F. Scherer. *J. Chem. Phys.*, 95:1487–1511, 1991.

[78] J. J. Macklin. *Science*, 272:255–258, 1996.

[79] A. H. Zewail. *Acc Chem. Res.*, 13:360–368, 1980.

[80] C. von Borczyskowski R. Brown J. Wrachtrup M. Orrit, J. Bernard. *J. Chem. Phys*, 100:7182–7191, 1994.

[81] I. Gerhard et al. *Phys. Rev. A.*, 79:011402, 2009.

[82] G. Wrigge et al. *Nature*, 4:60–66, 2008.

[83] H. Kamada. *Phys. Rev. Lett.*, 87:246401, 2001.

[84] H. Htoon et al. *Phys. Rev. Lett.*, 88:087401, 2002.

[85] J. Enderlein D. Parta, I. Gregor. *J. Phys. Chem. A*, 108:6836–6841, 2004.

[86] N. F. Van Hulst L. Novotny. *Nature*, 5:83–90, 2011.

[87] R. P. van Duyne D. L. Jeanmarie. *J. Electroanal. Chem.*, 84:1–20, 1977.

[88] G. C. Schatz. *Acc. Chem. Res.*, 17:370–376, 1984.

[89] P. J. Hendra R. L. Paul, A. J. McQuillan. 19775, journal =.

[90] M. Fleischmann A. J. McQuillan, P. J. Hendra. *J. Electroanal. Chem.*, 65:933, 1975.

[91] P. J. Hendra M. Fleischmann. *Chem. Phys. Lett.*, 26:163, 1974.

[92] J. A. Creighton M. G. Albrecht. *J. Am. Chem. Soc.*, 99:5215, 1977.

[93] R. P. Van Duyne A. B. Apkarian. *J. Am. Chem. Soc.*, 99:5215, 19.

[94] D. A. Zwener T. H. Wood, M. V. Klein. *Surf. Sci.*, 107:625, 1981.

[95] H. Seki. *J. Vac. Sci. Tech.*, 18:633, 1981.

[96] J. Creighton. *Surf. Sci.*, 124:209, 1983.

[97] Moody et al. *App. Spec.*, 41:966, 1987.

[98] J. Kottman O. Martin. *Opt. Exp.*, 8:655, 2001.

[99] F. D. Stefani T. H. Taminlau. *Opt. Express*, 16:10858–10866, 2008.

[100] E. A. Kort E. Cubucku. *Appl. Phys. Lett.*, 89:093120, 2006.

[101] K. Catchpole S. Pillai. *J. Appl. Phys.*, 101:093105, 2007.

[102] S. J. Stranick L. Novotny. *Ann. Rev. Phys. Chem.*, 57:303–331, 2006.

[103] P. Ghenuche et al. *Phys. Rev. Lett.*, 101:116805, 2008.

[104] O. J. F. Martin P Muehlschlegel, H. J. Eisler. *Science*, 308:1607–1609, 2005.

[105] B. Deutsch P. Bharadwaj. *Adv. Opt. Photon.*, 1:438–483, 2009.

[106] D. D. Whitmore. *J. Phys. Chem. C*, 115:15900–15907, 2011.

[107] J. J. Baumberg S. Mahajan C. Steuwe, C. F. Kaminski. *Nano. Lett.*, 11:5339–5343, 2011.

[108] S. R. Emory S. Nie. *Science*, 275:1102–1106, 1997.

[109] K. Kneipp et al. *Phys. Rev. Lett.*, 78:1667–1670, 1997.

[110] E. C. Le Rue P. G. Etchegoin. *Phys. Chem. Chem. Phys.*, 10:6097–6089, 2008.

[111] M. Stockburger P. Hildebrandt. *J. Phys. Chem.*, 88:5935, 1984.

[112] R. Zhang et al. *Nature*, 498:82–86, 2013.

[113] J. G. Bergman P. F. Liao. *Chem. Phys. Lett.*, 82:355–359, 1981.

[114] R. P. van Duyne K. A. Willets. *Ann. Rev. Phys. Chem.*, 58:267–297, 2007.

[115] M. A. Young A. D. McFarland. *J. Phys. Chem. B.*, 109:11279–11285, 2005.

[116] L. E. Brus A. M. Michaels, M. Nirmal. *J. Am. Chem. Soc.*, 121:9932–9939, 1999.

[117] L. Brus A. M. Michaels. *J. Phys. Chem. B.*, 104:11965–11971, 2000.

[118] A. Murphy M. D. Doherty. *J. Phys. Chem. C.*, 114:19913–19919, 2010.

[119] Y. Kikkawa T. Itoh. *J. Photochem. Photobiol. A*, 183:322–328, 2006.

[120] P. Nordlander J. Zuloaga. *Nano. Lett.*, 11:1280–1283, 2011.

[121] D. J. Masiello J. P. Litz, J. P. Camden. *J. Phys. Chem. Lett.*, 2:1695–1700, 2011.

[122] S. L. Kleinman et al. *J. Am. Chem. Soc.*, 35:301–308, 2013.

[123] H. Metiu P. Aravind, A. Nitzan. *Surf. Sci.*, 110:189, 1981.

[124] G. C. Schatz E. Hau. *J. Chem. Phys.*, 120:357, 2004.

[125] D. L. Mills P. A. Letnes, I. Simonsen. *Phys. Rev. B*, 83:75426, 2011.

[126] M. Kall H. Xu. *Phys. Rev. Lett.*, 89:246802, 2002.

[127] N. Valley S. L. Kleinman, E. Ringe. *J. Am. Chem. Soc.*, 133:4115, 2011.

[128] S. J. Lee G. B. Braun. *J. Phys. Chem C*, 113:13622, 2009.

[129] K. Bosnik J. Jiang. *J. Phys. Chem. B*, 107:9964–9972, 2003.

[130] Y. Maruyama M. Futamata. *J. Mol. Struc.*, 735:75–84, 2005.

[131] M. Banik et al. *ACS Nano*, 6:10343–10354, 2012.

[132] Kiefer et al. *J. Raman. Spec.*, 32:771, 2001.

[133] G. Knopp A. Materny. W. Kiefer, M. Schmitt. *Chem. Phys. Lett.*, 270:9, 1997.

[134] C. Burda S. Link. *J. Phys. Chem. B*, 104:6152–6163, 2000.

[135] F. Vallee N. Del Fatti, C. Flytzanis. *Appl. Phys. B*, 68:433, 1999.

[136] G. Hartland J. Hodak, I. Martini. *J. Phys. Chem. B*, 102:6958, 1998.

[137] J. Z. Zhang A. Faulhaber, B. A. Smith. *Mol. Cryst. Liq. Cryst.*, 283:25, 1996.

[138] U. Giebel G. Schmid B. A. Smith, J. Z. Zhang. *Chem. Phys. Lett.*, 270:139, 1997.

[139] M. Kerker. *The Scattering of Light anf Other Electromagnetic Radiation.* Academic Press, 1969.

[140] S. Koda H. Kurita, A. Takami. *Appl. Phys. Lett.*, 72:789, 1998.

[141] M. B. Mohamed S. Link, C. Burda. *J. Phys. Chem. A*, 103:1165, 1999.

[142] G. van Plessen M. Perner, P. Bost. *Phys. Rev. Lett.*, 78:2192, 1997.

[143] V. Namboodiri et al. *Vib. Spectrosc.*, 56:10, 2011.

[144] M. Hashimoto T Ichimura, N. Hayazawa. *Phys. Rev. Lett.*, 94:220801, 2004.

[145] Shen et al. *Phys. Rev. Lett.*, 43:943, 1979.

[146] M. Kerker H. Chew, D.S. Wang. *J. Opt. Soc. Am. B*, 1:1, 1984.

[147] M. Kerker H. Chew, D. S. Wang. *J. Opt. Soc. Am. B*, 1:56, 1984.

[148] Voronine et al. *Sci Rep*, 2:891, 2013.

[149] Kiefer et. al. *J. Raman Spec.*, 32:771, 2001.

[150] W. Kiefer M Schmitt; G. Knopp, A. Materny. *Chem. Phys. Lett.*, 270:9, 1997.

[151] Karavitis et. al. *J. Chem. Phys.*, 114:4131, 2001.

[152] Segale et. al. *J. Chem. Phys.*, 135:024203, 2011.

[153] Senekerimyan et al. *J. Chem. Phys.*, 127:8, 2007.

[154] J. R. McDonald A. B. Harvey W. M. Tolles, J. W. Nibbler. *Appl. Spectrosc.*, 31:253, 1977.

[155] M. B. Rashke R. L. Olmon. *Nanotechnology*, 23:444001, 2012.

[156] Y. Silberderg N. Dudovich, D. Oron. *Nature*, 418:512, 2002.

[157] D. J. Tannor. *Introduction to Quantum Mechanics: A Time Dependent Perspective*. University Science Books, 2007.

[158] R.W. Terhune. *Bull. Amer. Phys. Soc.*, 8:359, 1963.

[159] R.P.V. Duyne. *J. Electroanalytical Chem.*, 8:359, 1963.

[160] A. Otto. *Surface Science*, 75:L392, 1978.

[161] Kleinman et. al. *J. Am. Chem. Soc.*, 135:301, 2012.

[162] Wustholz et. al. *J. Am. Chem. Soc.*, 132:301, 2010.

[163] T.H. Wood M.V. Klein, D.A. Zwemer. *Surface Science*, 107:625, 1981.

[164] H. Seki. *J Vac Sci Tech*, 18:633, 1981.

[165] J. Creighton. *Surface Science*, 124:209, (1983).

[166] Moody et al. *App Spec*, 41:966, 1987.

[167] O. Martin J. Kottman. *Optics Express*, 8:655, 2001.

[168] Whitmore et. al. *J. Phys. Chem. C.*, 115:15900, 2011.

[169] C. Steuwe et al. *Nano Letters*, 11:5339, 2011.

[170] Apkarian et al. *J. Phys. Chem.*, 18:10415, 2012.

[171] V. Namboodiri et al. *Vib. Spec.*, 56:9, 2011.

[172] Apkarian et al. *ACS Nano*, 6:10343, 2012.

[173] Koo et al. *Opt. Lett.*, 30:1024, 2005.

[174] J.J. Baumberg S. Mahajan C. Steuwe, C.F. Kaminski. *Nano Lett*, 11:5339, 2011.

[175] A. Stingl et. al. *Opt. Lett.*, 20:602, 1995.

[176] E. Gulevich et. al. *Proc. SPIE*, 102:2095, 1994.

[177] Mourou G. Stock, M. L. *Opt. Comm.*, 106:249, 1994.

[178] Weinberg D. L. Burnham, D. C. *Phys. Rev. Lett.*, 25:84, 1970.

[179] Hasama. T. Jiang, J. *Opt. Comm.*, 220:193, 2003.

[180] Salin. F. Squier, J. *Opt. Lett.*, 16:324, 1991.

[181] Riedle et al. *Appl. Phys. B*, 71:457, 2000.

[182] Steiner-Shepard M. K. Reed, M. K. *Opt. Lett.*, 19:1855, 1994.

[183] Chin S. L. Brodeur, A. *J. Opt. Soc. Am.*, 16:637, 1999.

[184] Schmacher D. Jarman, C. *Oh. St. Univ.*, 10:430, 2005.

[185] Shapiro S. L. Alfano, R. R. *Phys. Rev. Lett.*, 24:592, 1970.

[186] Silvestri S. D. Cerullo, G. *Rev. Sci. Instr.*, 74:1, 2003.

[187] Gale G. M. Driscoll, T. J. *Opt. Comm.*, 110:638, 1994.

[188] Cavallari M. Gale, G. M. *Opt. Lett.*, 20:1562, 1995.

[189] Cavallari M. Gale, G. M. *J. Opt. Soc. Am. B*, 15:702, 1998.

[190] Riedle E. Piel, J. *Opt. Lett.*, 31:1289, 2006.

[191] Piel. J. Wilhelm, T. *Opt. Lett.*, 22:1494, 1997.

[192] Martinez O. E. Fork, R. L. *Opt. Lett.*, 9:150, 1984.

[193] R. Trebino. *Frequency Resolved Optical Gating*. Springer, 2000.

[194] Randolph W. Diels, J. *Ultrashort Pulse Phenomena Fundamentals, Techniques, and Applications on a Femtosecond Time Scale*. Elvesier, 2006.

[195] Pastirk I. Lozovoy, V. V. *Opt. Lett.*, 29:775, 2004.

[196] Walmsley I. A. Iaconis, C. *Opt. Lett.*, 23:792, 1998.

[197] Gong T. Nighan, W. L. *Opt. Comm.*, 69:339, 1989.

[198] L. Novotny M. Danckwerts. *Phys. Rev. Lett.*, 98:026104, 2007.

[199] S. Lefrant I. Baltog, M. Baibarac. *Phys. Rev. B.*, 72:245402, 2005.

[200] Stolow et. al. *Science*, 314:278, 2006.

[201] H. W. Yang. *J. Chem. Phys.*, 104:4313, 1996.

[202] S. Mukamel. *Principles of Nonlinear Optical Spectroscopy.* Oxford University Press, 1995.

[203] Dieringer et. al. *J. Am. Chem. Soc.*, 129:16249, 2007.

[204] V. A. Apkarian I. U. Golschleger, M. N. van Staveren. *J. Chem. Phys.*, 139:034201, 2013.

[205] J. A. Cina T. S. Humble. *Ultrafast Proceedings*, 14:514, 2005.

[206] N. F. van Hulst R. Hildner, D. Brinks. *Nature Physics*, 7:172, 2011.

[207] Kneipp et. al. *Phys. Rev. Lett.*, 76:2444, 1996.

[208] D. A. Lidar V. A. Apkarian R. Zadoyan, D. Kohen. *Chem. Phys.*, 266:323, 2001.

[209] Glenn et. al. *Mol. Phys.*, 104:1249, 2006.

[210] Bihary et. al. *Chem. Phys. Lett*, 360:459, 2002.

[211] M. van Staveren. I. Goldschleger. *J. Chem. Phys.*, 139:034201, 2013.

Appendix A

Appendix

A.1 Tomographic State Reconstruction and Excited State Wavepacket Propagation

The following is a manual for the generation of excited state wavepackets to simulate the time resolved spectra depicted in Chapter 5, along with the necessary code to generate WDF from Wigner Transforms and Inverse Radon Transforms.

1. Wavefunction and Energy Solution for Harmonic Oscillator

Force Constant k

```
kk = Solve[ω == Sqrt[k/μ], k] // Flatten
```

$$\{k \to \mu\, \omega^2\}$$

Harmonic Oscillator Potential; $\frac{1}{2}$ kx^2

```
V = 1/2 k x^2 /. kk
```

$$\frac{1}{2} x^2\, \mu\, \omega^2$$

Hamiltonian

```
H[ψ_] := -ħ^2/(2 μ) D[ψ, {x, 2}] + V ψ
```

Solving the Schrodinger

```
WF = DSolve[H[ψ[x]] == EE[v] ψ[x], ψ[x], x]
```

$$\left\{\left\{\psi[x] \to C[2]\ \text{ParabolicCylinderD}\left[\frac{-\omega\,\hbar - 2\,EE[v]}{2\,\omega\,\hbar}, \frac{i\,\sqrt{2}\,x\,\sqrt{\mu}\,\sqrt{\omega}}{\sqrt{\hbar}}\right] + C[1]\ \text{ParabolicCylinderD}\left[\frac{-\omega\,\hbar + 2\,EE[v]}{2\,\omega\,\hbar}, \frac{\sqrt{2}\,x\,\sqrt{\mu}\,\sqrt{\omega}}{\sqrt{\hbar}}\right]\right\}\right\}$$

Real Solusions only; C[2] -> 0 because C[2] has I term

```
WFsoln = FunctionExpand[ψ[x] /. WF] /. C[2] → 0
```

$$\left\{2^{-\frac{-\omega\,\hbar + 2\,EE[v]}{4\,\omega\,\hbar}}\, e^{-\frac{x^2\,\mu\,\omega}{2\,\hbar}}\, C[1]\ \text{HermiteH}\left[\frac{-\omega\,\hbar + 2\,EE[v]}{2\,\omega\,\hbar}, \frac{x\,\sqrt{\mu}\,\sqrt{\omega}}{\sqrt{\hbar}}\right]\right\}$$

Allowed energies have Hermite Polynomials in integer orders

```
En[v_] = Solve[(2 EE[v] - ħ ω)/(2 ħ ω) == 0 + v, EE[v]]
EnV = Table[EE[v] /. En[v], {v, 0, 2}] // Flatten
```

$$\left\{\left\{EE[v] \to \frac{1}{2}\,(1 + 2\,v)\,\omega\,\hbar\right\}\right\}$$

$$\left\{\frac{\omega\,\hbar}{2}, \frac{3\,\omega\,\hbar}{2}, \frac{5\,\omega\,\hbar}{2}\right\}$$

Now the Wavefunctions, and Normalize

```
Ψ[v_, x_] = WFsoln /. En[v] // Flatten // Simplify
```

$$\left\{2^{-v/2}\, e^{-\frac{x^2\,\mu\,\omega}{2\,\hbar}}\, C[1]\ \text{HermiteH}\left[v, \frac{x\,\sqrt{\mu}\,\sqrt{\omega}}{\sqrt{\hbar}}\right]\right\}$$

```
c0[v_, x_] := Solve[Integrate[Last[Ψ[v, x]^2], {x, -∞, ∞}, Assumptions → μ ω/ħ > 0] == 1, C[1]]
Ψ1[v_, x_] := Ψ[v, x] /. Last[c0[v, x]]
```

Some of the Wavefunctions

Ψ1 generates the wavefunction for eigenstate v, as a function of x, based on μ, $\hbar$, and ω

```
Ψ2[x_] = Table[Ψ1[v, x], {v, 0, 2}] // Flatten // FullSimplify;
gv = Grid[Partition[Table[v, {v, 0, 2}], 1], Spacings -> {0, 2}];
gwf = Grid[Partition[Ψ2[x], 1]];
gho = Grid[Partition[EnV, 1], Spacings → {0, 2}];
Grid[Partition[{gv, gwf, gho}, 3], Frame → All]
```

0	$\frac{e^{-\frac{x^2\,\mu\,\omega}{2\,\hbar}}}{\pi^{1/4}\left(\frac{\hbar}{\mu\,\omega}\right)^{1/4}}$	$\frac{\omega\,\hbar}{2}$
1	$\frac{\sqrt{2}\ e^{-\frac{x^2\,\mu\,\omega}{2\,\hbar}}\ x\,\mu^{3/2}\,\omega^{3/2}\left(\frac{\hbar}{\mu\,\omega}\right)^{3/4}}{\pi^{1/4}\,\hbar^{3/2}}$	$\frac{3\,\omega\,\hbar}{2}$
2	$\frac{e^{-\frac{x^2\,\mu\,\omega}{2\,\hbar}}\left(2\,x^2\,\mu\,\omega - \hbar\right)}{\sqrt{2}\ \pi^{1/4}\,\hbar\left(\frac{\hbar}{\mu\,\omega}\right)^{1/4}}$	$\frac{5\,\omega\,\hbar}{2}$

```
Ψ3 = Ψ2[x] /. μ → 1 /. ω → 1 /. ħ → 1
Ψ4 = Ψ2[x] /. μ → 1 /. ω → .6 /. ħ → 1
Ψ5 = Append[Ψ3, Ψ4] // Flatten;
Plot[Ψ5, {x, -5, 5}, PlotRange → All]
```

$$\left\{\frac{e^{-\frac{x^2}{2}}}{\pi^{1/4}}, \frac{\sqrt{2}\ e^{-\frac{x^2}{2}}\,x}{\pi^{1/4}}, \frac{e^{-\frac{x^2}{2}}\left(-1 + 2\,x^2\right)}{\sqrt{2}\ \pi^{1/4}}\right\}$$

$$\left\{0.661074\, e^{-0.3\,x^2},\ 0.724171\, e^{-0.3\,x^2}\,x,\ 0.46745\, e^{-0.3\,x^2}\left(-1 + 1.2\,x^2\right)\right\}$$

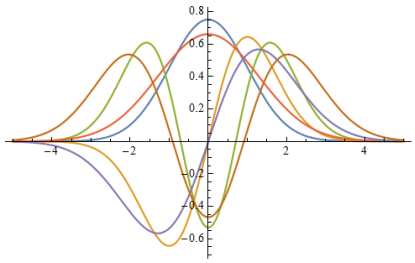

2. The Franck Condon Array

- **ψtab generates vibrational eigenstate wavefunctions in x in terms of parameters x, ω, $\hbar$ and μ**

```
ψtab = Monitor[Table[Ψ1[n, xx][[1]], {n, 0, 29}], n];
```

- **The Franck Condon Array describes the overlap of vibrational states across two potential energy surfaces, in this case ψB represents the vibrations on the first electronic state B as described in chapter 5, ψC is the second electronic state C. Input for ψC has been modified to adjust the ω relative to ψB;**

```
ψB[x_, n_, δ_] := ψtab[[n + 1]] /. xx → x - δ /. ħ → 1 /. μ → 1 /. ω → 1
ψC[x_, n_, δ_, ωδ_] := ψtab[[n + 1]] /. xx → x - δ /. ħ → 1 /. μ → 1 /. ω → ωδ
```

- **ω1 and ω2 are the vibrational frequencies of ψB and ψC respectively,**
  with their minima separated in energy by (in this case) 14900 cm^{-1}, ω2' s vibrational spacing DEPENDS ON ω that was chosen for ψC

```
Clear[ω2]
Elec1 = 10 000 × 2.998 × 10^10 10^-15 ;
Elec2 = 25 000 × 2.998 × 10^10 10^-15 ;
ω1 = Elec1 + 2.998 × 10^10 10^-15 {100, 200};
ω2[ωδ_] := Elec2 + 2.998 × 10^10 10^-15 Table[100 (0.4 + 0.1 ωδ) n, {n, 0, 29, 1}];
```

- **The Franck Condon Array; FCTabδ is the generated FC arrays for overlap in x for ψB and ψC vibrational wavefunctions sorted by ω of ψC and the displacement of the energy minima of ψB and ψC in x;**
  -Depicted in the plot is the FC overlap of the v=0 (Blue) and v=1 (Red) vibrations on B projected across 30 states on C for ωC=ωB and xδ= 5.0
  -The Overlap between any two states for variable curvature of C and variable xδ is accessed by FCTabδ by [[ω, xδ, v on B, v on C]];
  -$\omega\delta$ (0.5=1,0.6=2,0.7=3,0.8=4, 0.9=5,1.0=6) where 1.0 is identical curvature of ψB and ψC and 0.5 is ωC = 0.5ωB
  -xδ (0.0=1,0.5=2,1.0=3,1.5=4,2.0=5,2.5=6,3.0=7,3.5=8, 4.0=9, 4.5=10, 5.0=11, 5.5=12, 6.0=13) The separation between B and C energy minima in x from 0 to 6.0 in steps of x = 0.5

```
SetSharedVariable[{c1, c2, c3, c4}];
States = 29;
FCTabδ = Monitor[ParallelTable[c1 = ωδ;
    c2 = xδ;
    c3 = i;
    c4 = ii;
    ∫_-∞^∞ Conjugate[ψB[z, i, 0]] * ψC[z, ii, xδ, ωδ] dz, {ωδ, 0.5, 1, 0.1}, {xδ, 0, 6, 0.5}, {i, 0, 1}, {ii, 0, States, 1}],
  {(c1 - 0.5)/0.005 // N, c2/.06 // N, (c3 + 1)/0.02 // N, c4/(.01 States) // N}];

FCTab0 = Table[FCTabδ[[6, 11, 1, iii]] e^(-i 2 π (ω1[[1]] - ω2[6][[iii]]) t2), {iii, 1, 30, 1}];
FCTab1 = Table[FCTabδ[[6, 11, 2, iii]] e^(-i 2 π (ω1[[2]] - ω2[6][[iii]]) t2), {iii, 1, 30, 1}];
FCTab = Table[Abs[FCTab0 + FCTab1]^2, {t2, 0, 333, 83.25}];
STTab = Table[Abs[ψB[x, 0, 0] e^(-i 2 π (ω1[[1]]) t2 + ψB[x, 1, 0] e^(-i 2 π (ω1[[2]]) t2]^2, {t2, 166.5, 499.5, 83.25}, {x, -3, 3, .1}];

ListPlot[{Abs[FCTab0]^2 /. t2 → 0, Abs[FCTab1]^2 /. t2 → 0}, Filling → Axis, Frame → True, Axes → False, PlotRange → All,
 PlotStyle → {{Blue, PointSize[Large]}, {Red, PointSize[Large]}}]
```

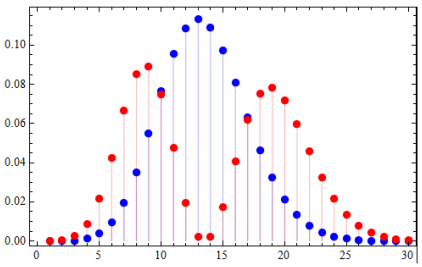

3. Spectrally Resolved Transient Grating

- **The function to generate a spectrum of < ψB | ψC > at any delay τ for a probe pulse energy of ωL, where additional parameters $\omega\delta$ and xδ extract the pertinent FC factors between the B and C vibrations from the calculated FC table above. Δt is the pulsewidth of the probe laser, and TT is the decay time of the vibrations on the C state. For illustrative purposes, the vibrations on the B state do not decay.**

  For the above parameters, the function calculates a table using ;

  $$< \psi_{B,v=m}(t_2) \mid \mu_{m,n}(X) \mid \psi_{C,v=n}(t_2) > \; < \psi_{C,v=n}(t_1) \mid \mu_{(n,m)}(X)\, E(\tau, \omega L) \mid \psi_{B,v=m}(t_1) >$$

  at a particular "grating" frequency (to spectrall resolved the signal) ω , for ω spanning 14100 cm^{-1} to 18100 cm^{-1}, in 40 cm^{-1} spacing. Additionally, one can modify the equation and generate a tr-spectrum by making a table of τ's to generate a 2D table.

```
Spectrum[τ_, ωL_, ωδ_, xδ_, Δt_, TT_] :=
 Table[
  Sum[
   Abs[Sum[e^(i 2 π 2.998×10^-5 ω t2) (FCtabδ[[ωδ, xδ, 1, ii]] e^(i 2 π (ω1[[1]]) t2) + FCtabδ[[ωδ, xδ, 2, ii]] e^(i 2 π (ω1[[2]]) t2)) e^(-i 2 π ω2[ωδ][[ii]] (t2-τ)-(t2-τ)/TT)
     Sum[e^-((t-τ)/Δt)^2 e^(-i 2 π 2.998×10^-5 ωL t) (FCtabδ[[ωδ, xδ, 1, ii]] e^(-i 2 π (ω1[[1]]-ω2[ωδ][[ii]]) t) +
       FCtabδ[[ωδ, xδ, 2, ii]] e^(-i 2 π (ω1[[2]]-ω2[ωδ][[ii]]) t)), {t, τ - Δt, τ + Δt, 5}], {t2, τ - 3 Δt, If[Δt > TT, τ + 2 Δt, τ + 2 TT], 5}]]^2,
   {ii, 1, 30, 1}], {ω, 14100, 18100, 40}];
```

- **Shown below is an example of a few spectra claculated at**

$\tau = 0, \frac{\pi}{2}, \pi, \frac{3\pi}{2}, 2\pi$

phases of the vibrations on the *B* state for $a\,x\delta = 5.0$, $\omega\delta = 1.0$, $\Delta t = 10$ fs, TT = 100 fs

-The spectrum is evaluated by fourier filtering at a frequency ω of a time slice that is 2 TT long (so for 100fs, the time slice is 200fs)
-On the far left is the $\rho_{10}(x)$ at the same τ' s as above with x={-5,5};
-To the right of these are the FC projections(Black) of B onto the C state vibrations in ω, where $\omega_{C,v=0} = 15000\ cm^{-1}$ at $x = 1$ on the plot, with the spectrum of the probe pulses used to generate the respective spectra to the right centered at 15300 cm^{-1}(Red), 15800 cm^{-1}(Green), 16300 cm^{-1}(Blue), 16800 cm^{-1}(Orange) and 17300 cm^{-1}(Brown)

```
Spectrum10fsP100fsT = Monitor[ParallelTable[c1 = τ;
   c2 = ω;
   Spectrum[τ, ω, 6, 11, 10, 100], {τ, 0, 333, 83.25}, {ω, 15300, 17300, 500}], {c1/3.33 // N, (c2 - 15300)/20 // N}];

Table[ListPlot[Transpose[Prepend[Prepend[Transpose[Spectrum10fsP100fsT], FCTab10], STTab]][[i, ii]], Joined → True,
   PlotRange → All, Frame → True, Axes → True, PlotStyle → PlotTab[[i, ii]]], {i, 1, 5, 1}, {ii, 1, 7, 1}] // TableForm
```

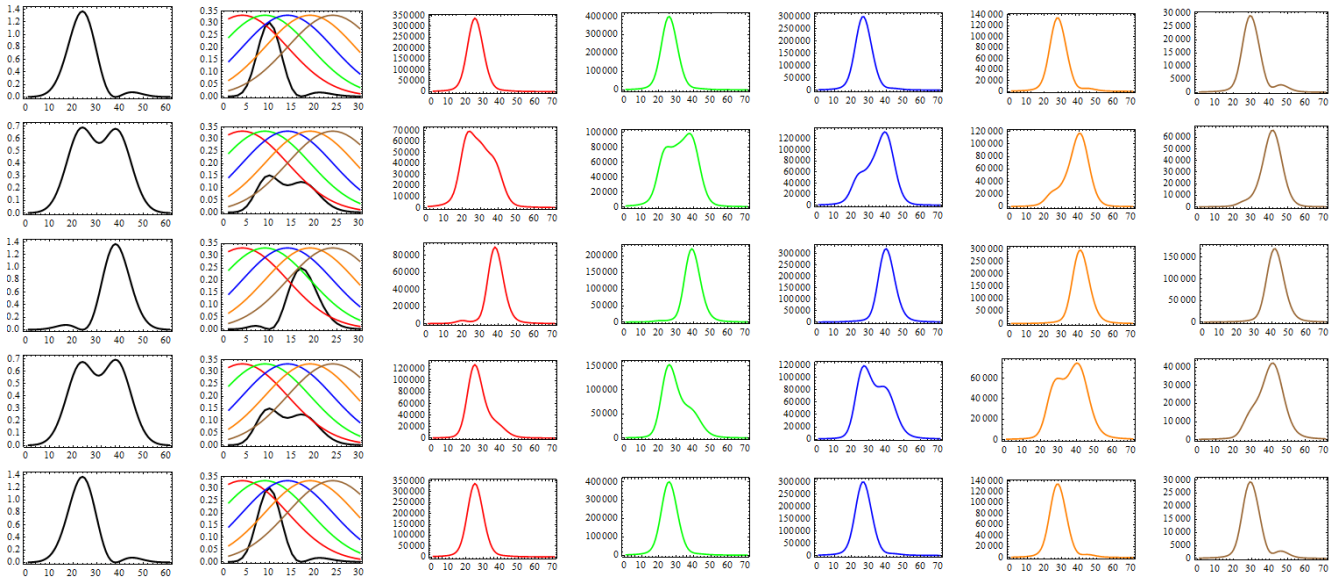

- **Below is the appendix code used to generate the projections and probe spectra plots. The far left spatiotemporal plots were generated in the Franck Condon Section using STTab**
  -This should be evaluated before the above plots are generated as it also contains the colormapping

```
Ten = Table[e^(-((ω-ω1)/(3333/(2 Sqrt[2 Log[2]/Log[e]])))^2), {ω1, 15300, 17300, 500}, {ω, 15000, 17900, 100}];
FCTab10 = Table[Prepend[Ten / 3, FCTab[[i]]], {i, 1, 5, 1}];
PlotTab = Table[{{Thick, Black}, {{Thick, Black}, {Red}, {Green}, {Blue}, {Orange}, {Brown}}, {Red}, {Green}, {Blue}, {Orange}, {Brown}}, {i, 1, 5, 1}];
```

---

4. The WDF of ψB and ψC and <ψB|ψC> obtained by Wigner Transform

- **The abbreviated FCTable is generated for a displacement between B and C ($x\delta = 5.0$) where B and C have identical ω**

```
FCtabδAbbr = Monitor[ParallelTable[c3 = i;
   c4 = ii;
   ∫_-∞^∞ Conjugate[ψB[z, i, 0]] * ψC[z, ii, 5, 1] dz, {i, 0, 1}, {ii, 0, States, 1}], {(c3 + 1)/0.02 // N, c4/(.01 States) // N}];
```

- **The Wigner Transform takes a wavefunction that is defined in spacial coordinate x and transforms it to be defined in position x, and momentum p;**

$\psi(x,p) = \int \psi^*\left(x + \frac{s}{2}\right)\psi\left(x - \frac{s}{2}\right) ds$

Time dependence of the wavefunction can be attached and is unmodified by the transform. Therefore an instantaneneous transform from wavefunction in position space can be transformed to a wavefunction in position AND monetum space.

The transform was used on ψB and ψC to depict the wavepackets in phase space while ψB is evolving, and at some time τ a probe pulse creates ψC
-for ψB the process is trivial, the wavefunction is sent through the Wigner Transform with time dependence attached and spits out a phase space representation of the wavefunction that is also time dependent. It is plotted in x and p {-5,5} and offset in x by $x\delta$ (in this case 5.0) so that ψB and ψC can be shown in the same plot accurately)

```
Wignerψ1f = Monitor[ParallelTable[c1 = t;
   c2 = q;
   c3 = p;
   NIntegrate[Sum[ψB[q + s/2, i, 0] e^(i 2 π ω1[[i+1]] 10.40625 (t-1)), {i, 0, 1, 1}] Sum[ψB[q - s/2, i, 0] e^(-i 2 π ω1[[i+1]] 10.40625 (t-1)), {i, 0, 1, 1}] e^(i p s), {s, -10, 10}], {t, 1, 65, 1},
   {q, -3, 12.6, .4}, {p, -8, 8, .4}], {c1/.65 // N, (c2 + 3)/.156 // N, (c3 + 8)/.16 // N}];
```

- **The Wigner Transform of ψC is a bit more complicated as the time dependent coefficients that develop as a function of the probe pulse time are calculated, with FC factors taken into account; a2f and a2Conjf are tables of the time dependent coefficients of the vibrations on the C state that are calcualted for a probe pulse incident on ψB at time τ. in this case, the probe pulse is 10 fs in duration centered at 16200 cm^{-1}**

```
a2f[τ_] := Monitor[ParallelTable[c1 = t2; c2 = i; Sum[e^(-((t-τ)/10)^2) e^(-ι 2 π 2.998×10^-5 16200 t) (FCtabδAbbr[[1, i]] e^(-ι 2 π (ω1[[1]]-ω2[6][[i]]) t) +
        FCtabδAbbr[[2, i]] e^(-ι 2 π (ω1[[2]]-ω2[6][[i]]) t)), {t, 0, t2}], {t2, 0, 666, 666/64 // N}, {i, 1, 30, 1}], {(c1 - 100)/6.66 // N, c2/.3 // N}];
a2Conjf[τ_] := Monitor[ParallelTable[c1 = t2; c2 = i; Conjugate[Sum[e^(-((t-τ)/10)^2) e^(-ι 2 π 2.998×10^-5 16200 t) (FCtabδAbbr[[1, i]] e^(-ι 2 π (ω1[[1]]-ω2[6][[i]]) t) +
        FCtabδAbbr[[2, i]] e^(-ι 2 π (ω1[[2]]-ω2[6][[i]]) t)), {t, 0, t2}]], {t2, 0, 666, 666/64 // N}, {i, 1, 30, 1}], {(c1 - 100)/6.66 // N, c2/.3 // N}];
a2τ100f = a2f[166];
a2Conjτ100f = a2Conjf[166];
Dimensions[a2τ100f]
{65, 30}
```

- **The coefficients are plugged into the spatial and temporal dependence of ψC as it undergoes a Wigner Transform and dephases in 500fs (for illustrative purposes)**

```
Wignerψ2f = Monitor[ParallelTable[c1 = tt;
    c2 = q;
    c3 = p;
    NIntegrate[Sum[ψC[q + s/2, i - 1, 0, 1] e^(ι 2 π ω2[6][[i]] (10.40625 (tt-1))-((10.40625 (tt-1))-166.5)/500) a2Conjτ100f[[tt, i]], {i, 1, 30, 1}]
      Sum[ψC[q - s/2, i - 1, 0, 1] e^(-ι 2 π ω2[6][[i]] (10.40625 (tt-1))-((10.40625 (tt-1))-166.5)/500) a2τ100f[[tt, i]], {i, 1, 30, 1}] e^(ι p s), {s, -10, 10}], {tt, 1, 65, 1}, {q, -8, 7.6, .4}, {p, -8, 8, .4}],
  {c1/.65 // N, (c2 + 8)/.156 // N, (c3 + 8)/.16 // N}];
```

- **The result is the phase space representation of the B and C wavepackets as they propagate in time and a probe pulse creates ψC at τ = 166 fs, of the π phase of the B wavepacket, the top plot shows both wavepackets propgating independently, and the bottom plot depicts the coherence of the two in phase space.**

```
myColorFunction[x_] /; x < 0 := ColorData["AvocadoColors"][2 Abs[x]]
myColorFunction[x_] /; x ≥ 0 := ColorData["SunsetColors"][Abs[x]]
ψ1ψ2 =
  Monitor[
   Table[{ListDensityPlot[Re[Transpose[180 Wignerψ1f[[i]] + Wignerψ2f[[i]]]]/700, ColorFunction → myColorFunction, PlotRange → All, InterpolationOrder → 2,
      ColorFunctionScaling → False, PlotLabel → Style[10.40625 (i - 1) "fs", 16, Black]],
     ListDensityPlot[Re[Transpose[180 Wignerψ1f[[i]] * Wignerψ2f[[i]]]]/250000, ColorFunction → myColorFunction, PlotRange → All, InterpolationOrder → 2,
      ColorFunctionScaling → False, PlotLabel → Style[10.40625 (i - 1) "fs", 16, Black]]}, {i, 1, 65, 1}], i/.65 // N];
m = Manipulate[ψ1ψ2[[i]] // TableForm, {i, 1, 65, 1}]
```

Out[612]=

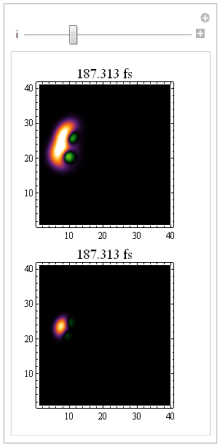

5. The WDF of < ψB | ψC > Obtained by Inverse Radon Transform

- **Because the WDF can be obtained from a wavefunction by Wigner Transform, it must be obtained from the Spectral Density for comparison of reproduction, in effect, how does the Density derived WDF differ from the Wigner Transform Derived WDF**
  - **-The IRT requires a sampling of the density over π phase of evolution. Hence the tr-Spectra for each WDF are generated over π of the evolution.**
  - **-The π tr-Spectra undergo Inverse Radon Transform;**
    - **-The spectra are generated using the Spectrum Function Above for an xδ=5.0, identical curvatures $\omega\delta$=1.0, probed at 16 200 cm^{-1} by *a* 10 fs probe pulse and *a C* dephasing time of 50 fs**
    - **-The TimeSpectrum variable is the 2D table of spectrum (x axis), vs time of the probe pulse (y axis). MatrixPlot plots the 2D table.**
    - **-The table is manipulated in format (not in substance) to undergo IRT, and formatted again to be depicted in ListDensityPlot.**
    - **-Both Density Plots are of the same table, but using 2 different color schemes to enhance negative and positive features in the plot.**
    - **-This is dome iteratively to generate the WDF at 4 phases.**

```
TimeSpectrum1 = Monitor[ParallelTable[c1 = τ; Spectrum[τ, 16200, 6, 11, 10, 50], {τ, 249.75, 416.25, 166.5/20 // N}], (c1 - 249.75)/1.665 // N];
MatrixPlot[TimeSpectrum1, ColorFunction → "Rainbow"]
```

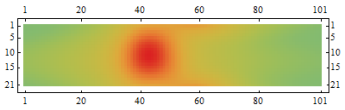

```
density1 = ImageData[InverseRadon[Image[Chop[Transpose[TimeSpectrum1 / 70]] // N]]];
s1 = {ListDensityPlot[ImageData[InverseRadon[Image[Chop[Transpose[TimeSpectrum1]] // N]]], PlotRange → All, ColorFunction → "Rainbow"],
  ListDensityPlot[ImageData[InverseRadon[Image[Chop[Transpose[TimeSpectrum1 / 70]] // N]]], PlotRange → All, ColorFunction → myColorFunction, ColorFunctionScaling → False]}
```

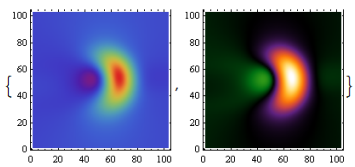

```
TimeSpectrum2 = Monitor[ParallelTable[c1 = τ; Spectrum[τ, 16200, 6, 11, 10, 50], {τ, 499.5, 666, 166.5/20 // N}], (c1 - 499.5)/1.665 // N];
MatrixPlot[TimeSpectrum2, ColorFunction → "Rainbow"]
```

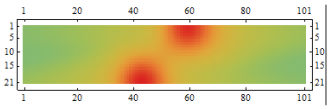

```
density2 = ImageData[InverseRadon[Image[Chop[Transpose[TimeSpectrum2 / 75]] // N]]];
s2 = {ListDensityPlot[ImageData[InverseRadon[Image[Chop[Transpose[TimeSpectrum2]] // N]]], PlotRange → All, ColorFunction → "Rainbow"],
  ListDensityPlot[ImageData[InverseRadon[Image[Chop[Transpose[TimeSpectrum2 / 75]] // N]]], PlotRange → All, ColorFunction → myColorFunction, ColorFunctionScaling → False]}
```

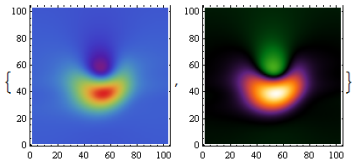

```
TimeSpectrum3 = Monitor[ParallelTable[c1 = τ; Spectrum[τ, 16200, 6, 11, 10, 50], {τ, 416.25, 582.75, 166.5/20 // N}], (c1 - 416.25)/1.665 // N];
MatrixPlot[TimeSpectrum3, ColorFunction → "Rainbow"]
```

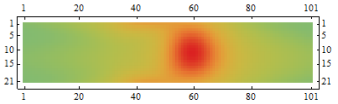

```
density3 = ImageData[InverseRadon[Image[Chop[Transpose[TimeSpectrum3 / 70]] // N]]];
s3 = {ListDensityPlot[ImageData[InverseRadon[Image[Chop[Transpose[TimeSpectrum3]] // N]]], PlotRange → All, ColorFunction → "Rainbow"],
  ListDensityPlot[ImageData[InverseRadon[Image[Chop[Transpose[TimeSpectrum3 / 70]] // N]]], PlotRange → All, ColorFunction → myColorFunction, ColorFunctionScaling → False]}
```

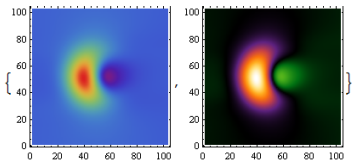

```
TimeSpectrum4 = Monitor[ParallelTable[c1 = τ; Spectrum[τ, 16200, 6, 11, 10, 50], {τ, 333, 499.5, 166.5/20 // N}], (c1 - 333)/1.665 // N];
MatrixPlot[TimeSpectrum4, ColorFunction → "Rainbow"]
```

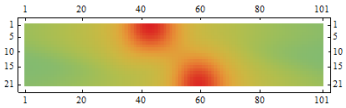

```
density4 = ImageData[InverseRadon[Image[Chop[Transpose[TimeSpectrum4 / 70]] // N]]];
s4 = {ListDensityPlot[ImageData[InverseRadon[Image[Chop[Transpose[TimeSpectrum4]] // N]]], PlotRange → All, ColorFunction → "Rainbow"],
  ListDensityPlot[ImageData[InverseRadon[Image[Chop[Transpose[TimeSpectrum4 / 70]] // N]]], PlotRange → All, ColorFunction → myColorFunction, ColorFunctionScaling → False]}
```

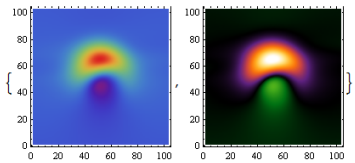

- **The WDF of the B wavepacket is generated at the same phases, same as in the previous section for comparison via Wigner Transform**

```
Wignerψ1f2 = Monitor[ParallelTable[c1 = t;
    c2 = q;
    c3 = p;
    NIntegrate[Sum[ψB[q + s/2, i, 0] e^(i 2 π ωi[[i+1]] 83.25 t, {i, 0, 1, 1}] Sum[ψB[q - s/2, i, 0] e^(-i 2 π ωi[[i+1]] 83.25 (t), {i, 0, 1, 1}] e^(i p s, {s, -10, 10}], {t, 0, 3, 1},
    {q, -3.0, 3.0, 6/102 // N}, {p, -3.0, 3.0, 6/102 // N}], {c1/.03 // N, (c2 + 3.0)/.06 // N, (c3 + 3.0)/.06 // N}];

wavepacket1 = Re[Transpose[Wignerψ1f2[[1]]]];
b1 = {ListDensityPlot[Re[Transpose[Wignerψ1f2[[1]]]], PlotRange → All, ColorFunction → "Rainbow"],
  ListDensityPlot[Re[Transpose[Wignerψ1f2[[1]]]/5], PlotRange → All, ColorFunction → myColorFunction, ColorFunctionScaling → False]}
```

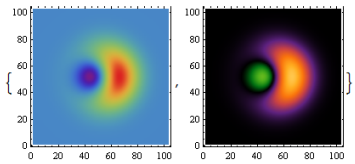

```
wavepacket2 = Re[Transpose[Wignerψ1f2[[2]]]];
b2 = {ListDensityPlot[Re[Transpose[Wignerψ1f2[[2]]]], PlotRange → All, ColorFunction → "Rainbow"],
  ListDensityPlot[Re[Transpose[Wignerψ1f2[[2]]]/5], PlotRange → All, ColorFunction → myColorFunction, ColorFunctionScaling → False]}
```

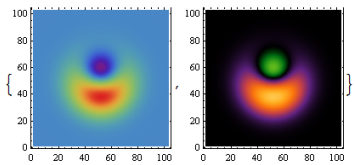

```
wavepacket3 = Re[Transpose[Wigner𝜓1f2[[3]]]];
b3 = {ListDensityPlot[Re[Transpose[Wigner𝜓1f2[[3]]]], PlotRange → All, ColorFunction → "Rainbow"],
  ListDensityPlot[Re[Transpose[Wigner𝜓1f2[[3]]]/5], PlotRange → All, ColorFunction → myColorFunction, ColorFunctionScaling → False]}
```

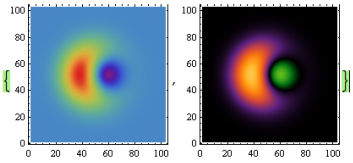

```
wavepacket4 = Re[Transpose[Wigner𝜓1f2[[4]]]];
b4 = {ListDensityPlot[Re[Transpose[Wigner𝜓1f2[[4]]]], PlotRange → All, ColorFunction → "Rainbow"],
  ListDensityPlot[Re[Transpose[Wigner𝜓1f2[[4]]]/5], PlotRange → All, ColorFunction → myColorFunction, ColorFunctionScaling → False]}
```

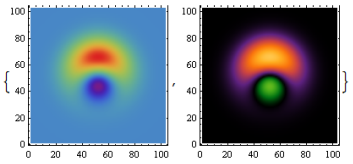

- **The comparison of the Density derived WDF from SRTG(Bottom Pane) and Wigner Transformed B wavepacket(top Pane)**

```
{{b1[[2]], b2[[2]], b3[[2]], b4[[2]]}, {s1[[2]], s2[[2]], s3[[2]], s4[[2]]}} // TableForm
```

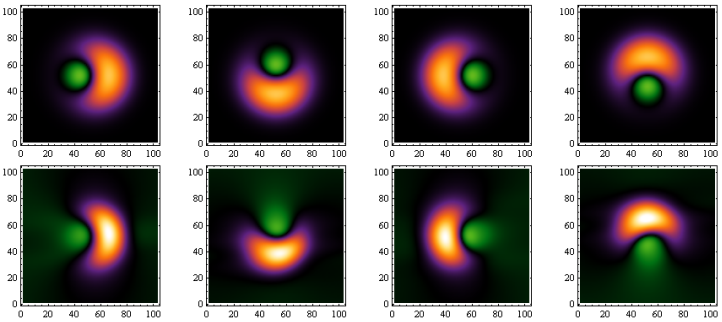

- **The respective WDFs are Normalized to generate a Residual Plot to highlite the difference in reproduction, along with plots of the momentum integrated WDFs as they would appear in space**

```
w1 = 10^3 wavepacket1 / Total[Total[wavepacket1]];
w2 = 10^3 wavepacket2 / Total[Total[wavepacket2]];
w3 = 10^3 wavepacket3 / Total[Total[wavepacket3]];
w4 = 10^3 wavepacket4 / Total[Total[wavepacket4]];
d1 = 10^3 density1 / Total[Total[density1]];
d2 = 10^3 density2 / Total[Total[density2]];
d3 = 10^3 density3 / Total[Total[density3]];
d4 = 10^3 density4 / Total[Total[density4]];
res1 = w1 - d1;
res2 = w2 - d2;
res3 = w3 - d3;
res4 = w4 - d4;

w1int = Table[Total[Transpose[w1][[i]]], {i, 1, Length[Transpose[w1]]}];
w2int = Table[Total[Transpose[w2][[i]]], {i, 1, Length[Transpose[w2]]}];
w3int = Table[Total[Transpose[w3][[i]]], {i, 1, Length[Transpose[w3]]}];
w4int = Table[Total[Transpose[w4][[i]]], {i, 1, Length[Transpose[w4]]}];
d1int = Table[Total[Transpose[d1][[i]]], {i, 1, Length[Transpose[d1]]}];
d2int = Table[Total[Transpose[d2][[i]]], {i, 1, Length[Transpose[d2]]}];
d3int = Table[Total[Transpose[d3][[i]]], {i, 1, Length[Transpose[d3]]}];
d4int = Table[Total[Transpose[d4][[i]]], {i, 1, Length[Transpose[d4]]}];

{{ListDensityPlot[w1, PlotRange → All, ColorFunction → "Rainbow",
    PlotLegends → Placed[BarLegend[Automatic, LegendMargins → {{0, 0}, {10, 5}}, LegendLabel → "Wavepacket; t=0", LabelStyle → {Italic, FontFamily → "Helvetica"}], Above]],
  ListDensityPlot[d1, PlotRange → All, ColorFunction → "Rainbow",
    PlotLegends → Placed[BarLegend[Automatic, LegendMargins → {{0, 0}, {10, 5}}, LegendLabel → "Density; t=0", LabelStyle → {Italic, FontFamily → "Helvetica"}], Above]],
  ListDensityPlot[res1, PlotRange → All, ColorFunction → "Rainbow",
    PlotLegends → Placed[BarLegend[Automatic, LegendMargins → {{0, 0}, {10, 5}}, LegendLabel → "Residual", LabelStyle → {Italic, FontFamily → "Helvetica"}], Above]],
  ListPlot[{w1int, d1int}, Joined → True, PlotLegends → {"Wavepacket", "Density"}, Frame → True, Axes → True, PlotStyle → {Thick, Thick}]},
 {ListDensityPlot[w2, PlotRange → All, ColorFunction → "Rainbow",
    PlotLegends → Placed[BarLegend[Automatic, LegendMargins → {{0, 0}, {10, 5}}, LegendLabel → "Wavepacket; t=π/2", LabelStyle → {Italic, FontFamily → "Helvetica"}], Above]],
  ListDensityPlot[d2, PlotRange → All, ColorFunction → "Rainbow",
    PlotLegends → Placed[BarLegend[Automatic, LegendMargins → {{0, 0}, {10, 5}}, LegendLabel → "Density; t=π/2", LabelStyle → {Italic, FontFamily → "Helvetica"}], Above]],
  ListDensityPlot[res2, PlotRange → All, ColorFunction → "Rainbow",
    PlotLegends → Placed[BarLegend[Automatic, LegendMargins → {{0, 0}, {10, 5}}, LegendLabel → "Residual", LabelStyle → {Italic, FontFamily → "Helvetica"}], Above]],
  ListPlot[{w2int, d2int}, Joined → True, PlotLegends → {"Wavepacket", "Density"}, Frame → True, Axes → True, PlotStyle → {Thick, Thick}]},
 {ListDensityPlot[w3, PlotRange → All, ColorFunction → "Rainbow",
    PlotLegends → Placed[BarLegend[Automatic, LegendMargins → {{0, 0}, {10, 5}}, LegendLabel → "Wavepacket; t=π", LabelStyle → {Italic, FontFamily → "Helvetica"}], Above]],
  ListDensityPlot[d3, PlotRange → All, ColorFunction → "Rainbow",
    PlotLegends → Placed[BarLegend[Automatic, LegendMargins → {{0, 0}, {10, 5}}, LegendLabel → "Density; t=π", LabelStyle → {Italic, FontFamily → "Helvetica"}], Above]],
  ListDensityPlot[res3, PlotRange → All, ColorFunction → "Rainbow",
    PlotLegends → Placed[BarLegend[Automatic, LegendMargins → {{0, 0}, {10, 5}}, LegendLabel → "Residual", LabelStyle → {Italic, FontFamily → "Helvetica"}], Above]],
  ListPlot[{w3int, d3int}, Joined → True, PlotLegends → {"Wavepacket", "Density"}, Frame → True, Axes → True, PlotStyle → {Thick, Thick}]},
 {ListDensityPlot[w4, PlotRange → All, ColorFunction → "Rainbow",
    PlotLegends → Placed[BarLegend[Automatic, LegendMargins → {{0, 0}, {10, 5}}, LegendLabel → "Wavepacket; t=3π/2", LabelStyle → {Italic, FontFamily → "Helvetica"}], Above]],
  ListDensityPlot[d4, PlotRange → All, ColorFunction → "Rainbow",
    PlotLegends → Placed[BarLegend[Automatic, LegendMargins → {{0, 0}, {10, 5}}, LegendLabel → "Density; t=3π/2", LabelStyle → {Italic, FontFamily → "Helvetica"}], Above]],
  ListDensityPlot[res4, PlotRange → All, ColorFunction → "Rainbow",
    PlotLegends → Placed[BarLegend[Automatic, LegendMargins → {{0, 0}, {10, 5}}, LegendLabel → "Residual", LabelStyle → {Italic, FontFamily → "Helvetica"}], Above]],
  ListPlot[{w4int, d4int}, Joined → True, PlotLegends → {"Wavepacket", "Density"}, Frame → True, Axes → True, PlotStyle → {Thick, Thick}]}} // TableForm
```

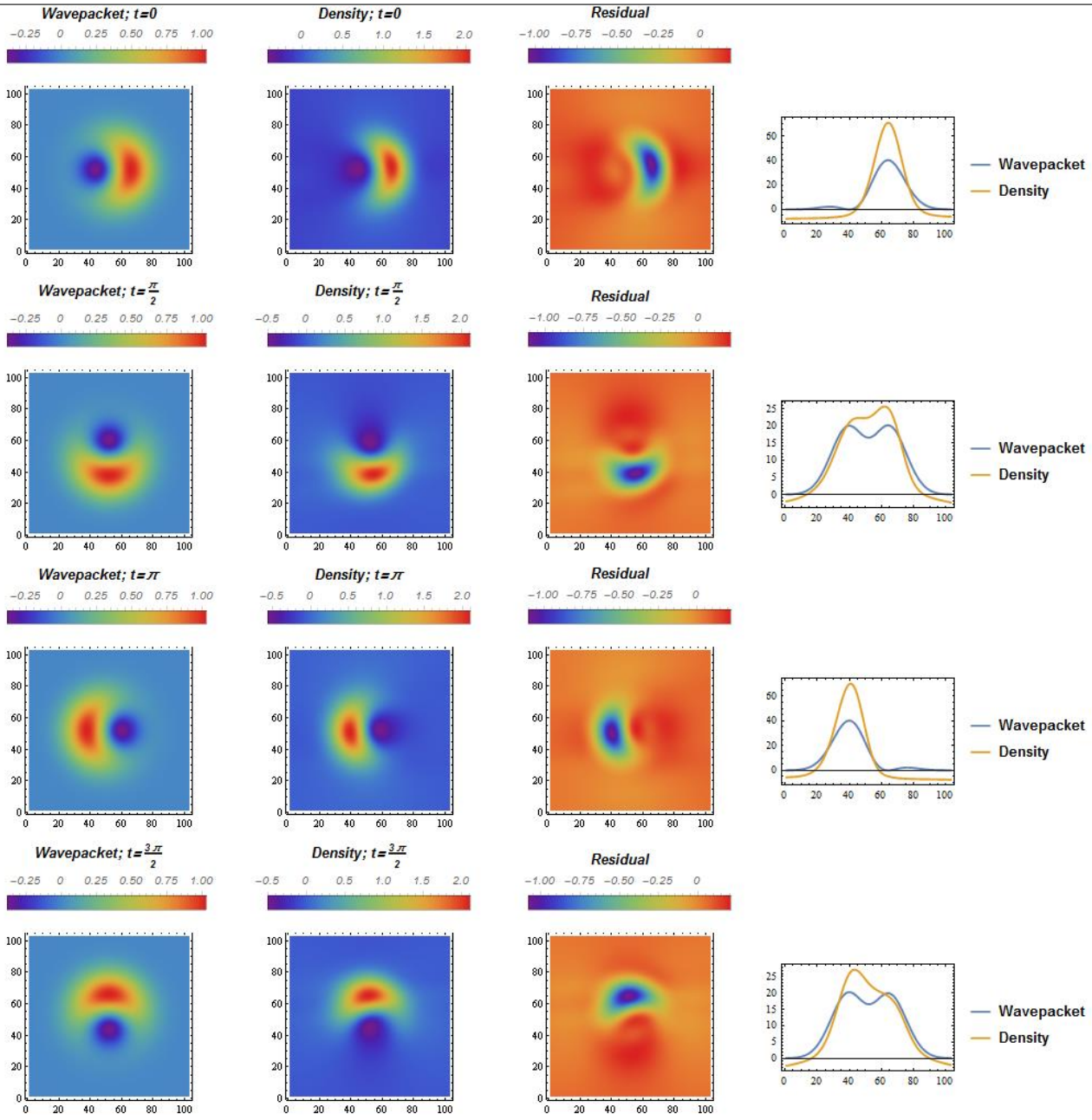
Wavepacket; t=0
Density; t=0
Residual
Wavepacket; t=π/2
Density; t=π/2
Residual
Wavepacket; t=π
Density; t=π
Residual
Wavepacket; t=3π/2
Density; t=3π/2
Residual
Wavepacket
Density